Hamilton College
Hamilton Digital Commons

Scholarly Projects | Works by Type

2012

Optically Trapped Fluorescent Nanodiamonds

Viva Horowitz
vhorowit@hamilton.edu

Follow this and additional works at: https://digitalcommons.hamilton.edu/other

Part of the Condensed Matter Physics Commons

Citation Information

Horowitz, Viva, "Optically Trapped Fluorescent Nanodiamonds" (2012). Hamilton Digital Commons. https://digitalcommons.hamilton.edu/other/3

This work is made available by Hamilton College for educational and research purposes under a Creative Commons BY-NC-ND 4.0 license. For more information, visit http://digitalcommons.hamilton.edu/about.html or contact digitalcommons@hamilton.edu.

UNIVERSITY OF CALIFORNIA
Santa Barbara

Optically trapped fluorescent nanodiamonds

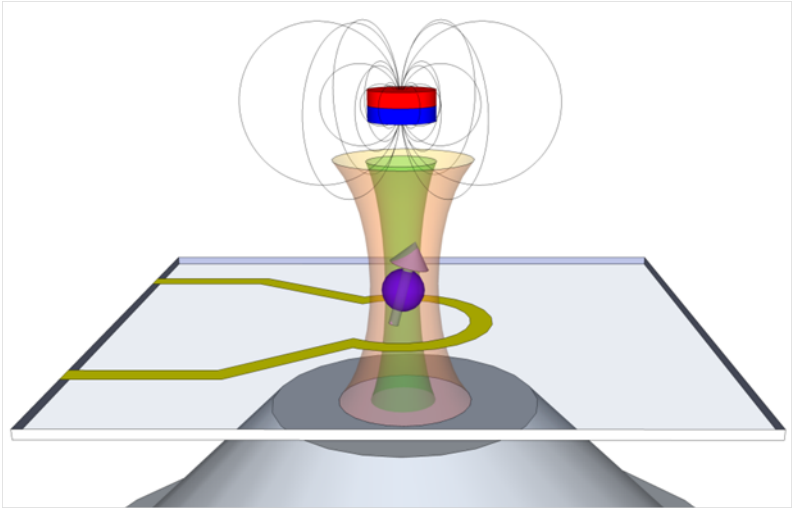

A dissertation submitted in partial satisfaction
of the requirements for the degree of

Doctor of Philosophy
in
Physics
by

Viva Rose Horowitz

Committee in charge:

Professor David D. Awschalom, Chairperson

Professor Elisabeth G. Gwinn

Professor Leon Balents

September 2012

The dissertation of Viva Rose Horowitz is approved:

David D. Awschalom, Committee Chairperson

August 2012

Optically trapped fluorescent nanodiamonds

Copyright © 2012

by

Viva Rose Horowitz

Abstract

Optically trapped fluorescent nanodiamonds

by

Viva Rose Horowitz

The nitrogen-vacancy (NV) color center in diamond is gaining significant interest for applications in nanoscale sensing. The optical addressability of the magnetically sensitive spin states and the ability to coherently control these states at room temperature makes this system an exciting candidate for spin-based magnetometry. I constructed an optical tweezers apparatus combined with a confocal fluorescence apparatus. Using the optical apparatus, we demonstrate three-dimensional position control of nanodiamonds in solution with simultaneous readout of ground-state electron-spin resonance (ESR) transitions in an ensemble of diamond nitrogen-vacancy (NV) color centers. Despite the motion and random orientation of NV centers suspended in the optical trap, we observe distinct peaks in the measured ESR spectra qualitatively similar to the same measurement in bulk. Accounting for the random dynamics, we model the ESR spectra observed in an externally applied magnetic field to enable dc magnetometry in solution. We estimate the dc magnetic field sensitivity based on variations in ESR line shapes to be ~45 $\mu T/\sqrt{Hz}$. This technique may provide a pathway for spin-based magnetic, electric, and thermal sensing in fluidic environments and biophysical systems inaccessible to existing scanning probe techniques.

Vitæ

Education

2005 B.A., Physics, Swarthmore College.

2011 M.A., Physics, University of California, Santa Barbara.

2012 Ph.D., Physics, University of California, Santa Barbara.

Publications

"Electron spin resonance of nitrogen-vacancy centers in optically trapped nanodiamonds," V. R. Horowitz, B. J. Alemán, D. J. Christle, A. N. Cleland, and D. D. Awschalom, *Proc. Natl. Acad. Sci. USA* **109**, 13493 (2012).

"Optofluidics: Field or technique?" V. R. Horowitz, D. D. Awschalom, S. Pennathur, *Lab on a Chip* **8**, 1856 (2008).

"Generating spin currents in semiconductors with the spin Hall effect," V. Sih, W. H. Lau, R. C. Myers, V. R. Horowitz, A. C. Gossard, D. D. Awschalom, *Physical Review Letters* **97**, 96605 (2006).

"Mechanical control of spin-orbit splitting in GaAs and $In_{0.04}Ga_{0.96}As$ epilayers," V. Sih, H. Knotz, J. Stephens, V. R. Horowitz, A. C. Gossard, D. D. Awschalom, *Physical Review B* **73**, 241316 (2006).

"Aggregation behavior and chromonic liquid crystal properties of an anionic monoazo dye," V. R. Horowitz, L. A. Janowitz, A. L. Modic, P. A. Heiney, P. J. Collings, *Physical Review E* **72**, 041710 (2005).

Fields of study

Major field: Physics

Optically trapped fluorescent nanodiamonds

Professor David D. Awschalom

Contents

Chapter 1 Introduction **1**
1.1 Optical tweezers 2
1.2 Nitrogen-vacancy centers in diamond 2
1.3 Optically trapped diamonds 6
1.4 Organization 8

Chapter 2 Optical tweezers **10**
2.1 Theory of optical trapping 10
2.1.1 Mie regime: The ray-optics approach 11
2.1.2 Rayleigh regime: The induced dipole approach 11
2.1.3 Gaussian potential well in the Rayleigh regime 13
2.2 Instrument 18
2.2.1 Optics 19
2.2.2 Conjugate focal planes 31
2.2.3 Benefits and disadvantages of a commercial microscope 40
2.2.4 Challenges and solutions 44
2.3 Characterization 46

Chapter 3 Nanodiamond fluorescence **57**
3.1 Instrument 58
3.2 Nanoparticle deposition 63
3.2.1 Drop-casting 63
3.2.2 Electrospray 63
3.3 Antibunching measurements 66

3.4 Blinking nanodiamond NV centers 69
3.5 Polarization 75
3.5.1 Calculating the angular dependence of the absorption of an NV center 75
3.5.2 Methods and Results 77
3.6 Optical trapping and fluorescence 79

Chapter 4 Electron spin resonance of NV centers in nanodiamonds 82
4.1 Antenna 82
4.2 Noise and software lock-in 84
4.3 Trapping nanodiamonds 89
4.4 ESR of immobilized nanodiamonds 89

Chapter 5 Magnetometry with optically trapped nanodiamonds 92
5.1 Apparatus and techniques 92
5.2 Estimating trap population of nanodiamonds 95
5.3 Optical collection efficiency 96
5.4 Modeling the ESR spectrum 98
5.4.1 Angular dependence of the excitation 99
5.4.2 The emission collected from a single NV center 102
5.4.3 Zeeman splitting 103
5.4.4 ESR spectrum of a single NV center 104
5.4.5 ESR spectrum of an isotropic ensemble of NV centers . . 106
5.4.6 Fitting the ESR curves 109
5.5 Results and Discussion 110

Chapter 6 Conclusion 115

Appendix A Etched nanodiamonds 116

References 119

List of figures

1.1 The diamond NV center: atomic structure and energy levels . . 3

2.1 The ray-optics interpretation of optical trapping 12
2.2 Gaussian beam intensity plot 16
2.3 Gaussian beam trapping potential 16
2.4 Non-paraxial Gaussian beam intensity plot 17
2.5 The 532 nm beam profile: theory vs. experiment 18
2.6 The optical tweezers apparatus 19
2.7 Dual trap by means of AOD time-sharing 24
2.8 Position calibration of a dual-axis AOD 26
2.9 Power calibration of a dual-axis AOD 27
2.10 Gaussian beam expansion and the knife edge technique 28
2.11 The steering lens and the objective rear aperture at conjugate focal planes 35
2.12 Placing the AOD conjugate to the steering lens 36
2.13 The IR collection path for position detection 39
2.14 Spatial control of optically trapped nanodiamonds 47
2.15 Bead position calibration 50
2.16 Identifying trapping problems: bead trajectory 53
2.17 Power spectrum of trapped bead for trap stiffness 54

3.1 The photoluminescence spectra of three fluorescent nanodiamonds. 57

3.2 The 532 nm excitation beam pathway and the fluorescence collection pathway. 61
3.3 Confocal fluorescence microscopy: a squid chromatophore . . . 62
3.4 AFM of electrosprayed nanodiamonds 65
3.5 Nanodiamond aggregation 66
3.6 Single NV fluorescence: line scans 67
3.7 Single-NV Antibunching 67
3.8 Comparison of spectra from bright intervals and dark intervals . 70
3.9 A single NV center with blinking detected in two color ranges. . 72
3.10 Histograms of NV center blinking duration. 73
3.11 Blinking with three levels 74
3.12 The absorption of an NV center 78
3.13 The fluorescence intensity and blinking of a single NV center at multiple excitation polarization angles 80

4.1 Microwave antenna 83
4.2 Noise of an ensemble of optically trapped nanodiamonds: standard deviation of I_{PL} 85
4.3 Electron microscopy images of nanodiamond samples 86
4.4 Power spectral density of the luminescence 87
4.5 Amplitude-modulated ESR in trapped nanodiamonds 88
4.6 Fluorescent particles entering the trap with discrete steps 90
4.7 ESR spectra and Zeeman splitting of immobilized nanodiamonds 91

5.1 Diagram of apparatus for measuring ESR spectra and Zeeman splitting in optically trapped nanodiamonds 93
5.2 Schematic of nanodiamond optical trapping, photoexcitation, and luminescence detection 94
5.3 Photoluminescence spectrum of optically trapped nanodiamonds 97
5.4 Angular dependence of absorption and emission of an NV center 101
5.5 NV center energy levels and Zeeman splitting 103
5.6 Calculated spin sublevel transition frequencies 105

5.7 The angular dependence of the measured I_{PL} of an NV center and the contribution to I_{PL} of each angle in an isotropic ensemble of NV centers 106
5.8 The modeled ESR spectrum for a single NV center 107
5.9 Modeled ESR spectra of an ensemble of randomly oriented NV centers 108
5.10 ESR spectra of optically trapped nanodiamonds in an external magnetic field with fits 111
5.11 ESR spectra of optically trapped nanodiamonds in an external magnetic field up to 60 G: measured and modeled 112
5.12 Magnetic field measured by the trapped NV ensemble 112
5.13 Magnetic sensitivity of the trapped NV ensemble 114

A.1 Procedure for etching nanodiamonds 117
A.2 SEM images of etched nanodiamonds with etch masks 118
A.3 SEM images of an etched nanodiamond with and without the etch mask 118

List of tables

2.1 Elements of the optical tweezer pathway 21
2.2 Elements of the IR collection path for position detection 22
2.3 Items relating to the optical tweezers apparatus 22

3.1 Elements of the optical excitation path 59
3.2 Elements of the fluorescence collection path 60

Acknowledgments

ב"ה

I am incredibly grateful to the many people who surround me with support. Above all, I owe many thanks to **David D. Awschalom** for his scientific support, encouragement, and superb mentorship. May I always emulate his high standards for excellence. David, thank you making this possible and for all you have taught me. May Chicago open new opportunities for you and your lab.

Thank you also to my committee, **Elisabeth G. Gwinn** and **Leon Balents**.

I have been honored to work collaboratively with many scientists, and I especially acknowledge **Benjamín J. Alemán, Jayna B. Jones, Erzsebet C. Vincent, Sumita Pennathur, Paolo Andrich, David Christle, David Toyli, Abram Falk, Lee Bassett, Ian McFarlane, Daniel Kirby, Lijuan (Lily) Li,** and **Vanessa Sih**. This dissertation expands on a recent publication [1], and some of the language and many figures are taken directly from that paper. I gratefully acknowledge my co-authors, **Benjamín J. Alemán, David J. Christle, Andrew N. Cleland,** and **David D. Awschalom**.

Benjamín J. Alemán, who has worked closely with me for the past year, is an amazing colleague in every way. Benji, thank you for your insight and enthusiasm, and for all that you do. My best to you and your beautiful family. I hope to continue collaborating with you in my future career. Go team OT!

Jayna B. Jones collaborated with me for years as we built up the lab. Jayna, thank you for all you have taught me.

Erzsebet Vincent is a top-notch undergraduate researcher with whom I have been honored to collaborate. Mentoring her as she performed optical studies of cephalopod chromatophores has been a highlight of my time here.

I acknowledge her specifically for preparing the sample shown in Fig. 3.3. Erzsi, thank you for always being there for me, especially as I re-aligned the optical tweezers pathway for the *n*th time. Thank you for nominating me for (and helping me receive) the CSEP Excellence in Mentoring award.

Sumita Pennathur has taught a great deal, including optical microscopy and microfluidics. She mentored me with great thoughtfulness while we wrote the article, "Optofluidics: field or technique?".

I have had the pleasure of working in graduate school with many fantastic scientists in the Awschalom group: **Benjamín J. Alemán, Paolo Andrich, Lee Bassett, Joerg Bochmann, Abram Falk, Alberto Politi, Steven Brown, Bob Buckley, Greg Calusine, David Christle, Charles de las Casas, Joseph Heremans, Paul Klimov, William Koehl, Brian Maertz, Ken Ohno, David Toyli, Chris Yale, Andrew Yeats, and Erzsebet Vincent** as well as past group members, including **Jayna Jones, Vanessa Sih, Greg Fuchs, Ian McFarlane, Mark Nowakowski, Shawn Mack, David Steuerman, Ineke Wijnheijmer, Sai Ghosh, Wayne Lau, Jason Stephens, Ronald Hanson, Ryan Epstein, Felix Mendoza, Maiken Hoegh Mikkelsen, Nate Stern, Jesse Berezovsky, Hadrian Knotz, John Heron, and Willem Peutz**. All of these people have contributed to my scientific education at UCSB. In addition to all the time we've spent together in the lab, we have had some good times traveling together in the Awschalom group, to Japan, Hawaii, Denver, and Boston. Also, **Will, Mark, Shawn** and I were classmates, and they made those long nights in the office more fun.

Paolo Andrich, in the few months you've been here, you have already contributed a great deal. The optical tweezers are yours; take good care of them. I wrote this dissertation for you. Sorry it's not in Italian.

I have enjoyed collaborating with **David J. Christle**, especially because of his enthusiasm for performing simulations and his smooth wordsmithing. David, thank you for your many contributions to this work, and especially for your analysis that made Figs. 5.12 and 5.13 possible.

David Toyli and **Abram Falk** helped design the research discussed in Appendix A. David and Abram, thank you for your valuable scientific comments

on all aspects of this research.

Thanks to **Lee Bassett** for valuable discussions, especially concerning the model of the ESR spectrum of an ensemble of randomly oriented NV centers, and for assistance with preparing Fig. 5.11.

I have split an optical table with a number of people, including **Joe Heremans, Chris Yale, David Toyli, Brian Maertz, and Ineke Wijnheijmer**. Thanks for sharing.

I am grateful to **John Joo** and **Elaine D. Haberer** in **Evelyn Hu**'s group for showing me how to breed bacteriophage, and to **Daniel DeMartini** for providing cephalopod samples.

Many people have offered me help over the years. I am grateful to **Rachel Sapiro, Ben Lopez and Megan Valentine** for advice. In a few cases, I received valuable comments in brief conversation; I am very glad to have spoken with **Iwijn de Vlaminck, Kamlesh D. Patel, and Shanying Cui**. (Now that we are collaborating with Shanying, I'm looking forward to more useful comments.)

I acknowledge the support of the DARPA, AFOSR, and the GAANN Fellowship Program.

I am grateful to **Beth Gwinn** for helping me receive a GAANN fellowship. As a GAANN fellow I also worked as a teaching assistant and have had the privilege of working with excellent educators, including **Sumita Pennathur** and **Harry Nelson**.

Thanks to the wonderful scientists and staff of the California NanoSystems Institute (CNSI), including **Mark Cornish, Stephan Kraemer, Claudia Gottstein, Arica Lubin, Ofelia Aguirre, Holly Woo, Bob Hanson, Paul Weakliem, Lynne Leininger, Daniel Daniels, Valerie Voita, Eva Deloa, Lindsey Kasehagen, Erin Lennon, Neysa Gleason, Anna-Marie Nuila-Chae, Alycia Lewis, Marissa Guillen, Stella Hahn**, and **Teddy Thomas.**

Thanks to the excellent staff in the Physics Department, including **Jeff Dutter, Mark Sheckherd, Mike Wrocklage, Doug Rehn, Andy Segale, and Guy Patterson** in the machine shop and **Jennifer Farrar, Kerri O'Connor, and Shilo Tucker** in the Department office.

Thanks to the cleanroom staff, including **Jack Whaley, Brian Thibeault,**

and Don Freeborn. The UCSB nanofabrication facility is part of the NSF-funded National Nanotechnology Infrastructure Network.

Thanks to the campus Facilities group, especially **Daniel Marquez**, **Jim**, and **Marc**.

Many thanks to my UCSB classroom professors, **Leon Balents, Evelyn Hu, Omar Saleh, Joseph Incandela, Doug Eardley, Boris Shraiman, and Andreas Ludwig**, and to my classmates.

Thanks to the wonderful people of the Women in Science and Engineering (WiSE), including **Giulia Piovan, Maria Napoli, and Natasha Vermaak**, and the Women in Physics, especially **Jennifer Cano, Jenna Hagemeier, Susanna Thon, and Lisa Manning**.

I acknowledge the vendors who provided me with equipment and who gave advice, warranty repairs, and who lent me their products as demos.

I have lived with a great many people, about 70% physicists, who have shaped my experience in Santa Barbara in many ways, so here's to my housemates, **Kevin, Zach, Ben, Will, Dan, Brian, and Richard** at Rhoads, **Andrew, Ramsey, Brian, Dan, Isaac, Ann, Anubhav, Suthee, Ryan, Ian, Joe, Shane, Susanna & Dustin, Erin, Christine, Jen, Anandi & Drew, Jill, Alison, and Nada** at Ravenscroft, and **Leslie, Sarah, and Fiona** at Newman. (Don't get the Dans or the Brians mixed up.) A good housemate is a wonderful thing.

For my family, **my mom, my grandma, my dad and stepmom, my grandma Ethel, my aunts and uncles, my cousins, Elias, Talia, Colin, Trevor, Graeme, and Eva** and my more distant relatives: your love and support are everything. Mom, thanks for helping me celebrate with a trip to Universal Studios.

I am grateful to the amazing people I've had the pleasure of meeting in Santa Barbara beyond the physics community.

The Jewish community of Santa Barbara has been an important part of my experience here. Santa Barbara Hillel has been my number one Jewish home-away-from-home in Santa Barbara. Chabad has never let me down and provides the best challah in the universe, Papa Lo's dough. Events with the Jewish Federation and the Young Adult Division (YAD) are always a good

time, thanks especially to **Mike Witt**. The Isla Vista Minyan is a treasure. Congregation B'nai B'rith and Young Israel have both been very welcoming shuls. Thanks to the religious leaders, **Rabbi Allison Conyer**, **Rabbi Evan Goodman**, **Rabbi Mendel Loschak** (who once taught a class on Talmud in the Physics library) and **Rebbetzin Rochel Loschak, Rabbi Loschak (Papa Lo) and Rebbetzin Devorah Loschak, Shelley and Yehuda Fowler, Rabbi Arthur Gross-Schaefer, Judy Karin, Rabbi Alyson Solomon, the Shushans, and Sarah Cohen Domont**. So many of my dear friends have been people I have shared a Shabbat meal with, including **Mike Gary, Sara Adler & Uri Mandelbaum, Stuart Brinkley, Nathan & Lindsay Roller, Dan Malinow, Doron Bergman, Rich & Anne-Claire Cain, Kimi Kuroda & Gideon Cohn, Valerie & Josh Bouganim, Meir Basson, Gaddiel Ouaknin, Liz Shayne & Josh Lannik, Aaron Sloane, Phil Miller, Arielle Leitner, Mike Schwartz, Jon Berlin, Micha Fireman, Diana Van Dijk, Julie Huniu, Ian McFarlane, Sara Covey, Claire Landa, Michal Silverstein, Yonah Lemonik, David Sforza, and Skona Brittain.**

Scott Marcus is the director of the UCSB Middle East Ensemble. Thanks to him, we traveled to Egypt and performed at the Cairo Opera House in 2010. I have performed countless concerts and gigs with the Ensemble, in Santa Barbara, Los Angeles, Michigan, and Egypt, and made some wonderful friends, including **Parker Abercrombie**, **Julie Huniu**, **Giselle Garcia**, **Lillie Gordon**, **Sachiyo Yoshimoto**, and, of course, the oud section, the accordion section, the qanun section, the violin (kamanga) section, the nay section, the drum section (with riqq, doumbek, tar, darbuka, and more), the cello section, the saz section, the saxophone section, the electric guitar section, the dancers, the soloists, and of course, my fellow singers. Thanks to everyone who has taught me to sing in Arabic (from Moroccan to Iraqi), Farsi, Turkish, Hebrew, Ladino, Greek, Armenian, and Assyrian.

Thanks to my tango instructors, **Brian Griffin** and **Fay Villanueva**. To all my tango partners, thank you for the dances.

I discovered running a few years ago and it has become an essential part of my life. Thanks especially to **Mike Gary** and **Richard Eager**, two amazing

friends who told me to try running even if I didn't think I could. (I couldn't, and ended up with six months of physical therapy, but now I can and do run. Many thanks to the **UCSB Student Health physical therapists**!) Thanks to my running partners, **Mike, Richard, Dan Malinow, Molly Forr, Parker Abercrombie, Rachel Weber, Chris McKenney, Naomi Miller-Wave, Erzsebet Vincent, and my dad.**

Thanks to NAMI and the MWC, especially **Deborah Smilovitz** for your education and support.

Thanks to **Stuart Winthrop** and his Lasik team for curing my myopia and astigmatism.

Thanks to the Elements Theater Collective for excellent shows and events. I'll always remember you as the group who performed Boom in an empty swimming pool in a suburban backyard, with the actors running around the steep slope between the deep end and the shallow end.

Thanks to **Alicia Jo Rabins** for her inspiring music. (It is always best to listen to music while aligning optics.) Thanks to KCLU and especially to **Tom Ashbrook** for telling me about all the happenings in the world outside.

For my out-of-town friends who have visited me in Santa Barbara, thank you for your friendship, and I'm sorry if I was distracted by scientific work while you were here. For my out-of-town friends who never visited me in Santa Barbara. . . last chance!

It is not possible to thank everyone who has brought me to this moment, but I am immensely grateful to you all, and I would especially like to thank **you, the reader**, who gives purpose to this document.

♦♦♦

Chapter 1

Introduction

We demonstrate a biocompatible approach to scanning nanodiamond magnetometry in solution using a single-beam optical tweezers apparatus. The optical trap uses the radiation pressure of a focused infrared laser beam to attract and hold an ensemble of diamond nanoparticles at the focus, while a second confocal green laser optically excites the embedded NV centers. The spin-dependence of the NV center's luminescence, together with a nearby microwave antenna, allow us to perform optically detected ESR measurements with simultaneous three-dimensional control in solution. We develop a model of the observed ESR spectra based on the ground-state Hamiltonian that accounts for the random motion of NV centers in the trap and incorporates the orientation-dependent absorption and luminescence collection efficiency. Using this model, we are able to infer the magnetic field experienced by the ensemble of NV centers and show an estimated magnetic sensitivity of $\sim 45\ \mu\mathrm{T}/\sqrt{\mathrm{Hz}}$.

1.1 Optical tweezers

Optical tweezers utilize tightly focused light to non-invasively trap and move small dielectric particles in three dimensions [2]. This powerful and biocompatible technique has allowed investigation of molecular motors [3], cell-sorting of a population of *Eschericha coli* based on single-cell viability [4], and even the observation of single-base-pair stepping (3.7 Å) of RNA polymerase along DNA [5]. With ultrastable, dual-beam optical tweezers achieving repeatable displacements at the nanometer scale and below [5,6], the prospect of combining optical tweezers with quantum-based sensors is particularly attractive for biosensing.

1.2 Nitrogen-vacancy centers in diamond

Nanodiamonds are biocompatible: they can enter cells without killing the cells. This biocompatibility, together with the photostability of fluorescent NV centers within nanodiamonds, is gaining attention for biological applications [7–11]. The quantum control of NV centers within living cells [12] points to potential applications of sensing, tracking, and tagging in submicron biophysical systems.

The optical spin polarization and spin-dependent photoluminescence intensity, I_{PL}, of NV centers enable optically detected ESR measurements. When combined with electromagnetically and thermally sensitive spin states, optically detected ESR permits the measurement of the local electric, magnetic, or thermal environment. The negatively charged NV center defect in diamond consists of a substitutional nitrogen atom adjacent to a vacancy in the diamond lattice (Fig. 1.1*A*). The NV center's unperturbed electronic

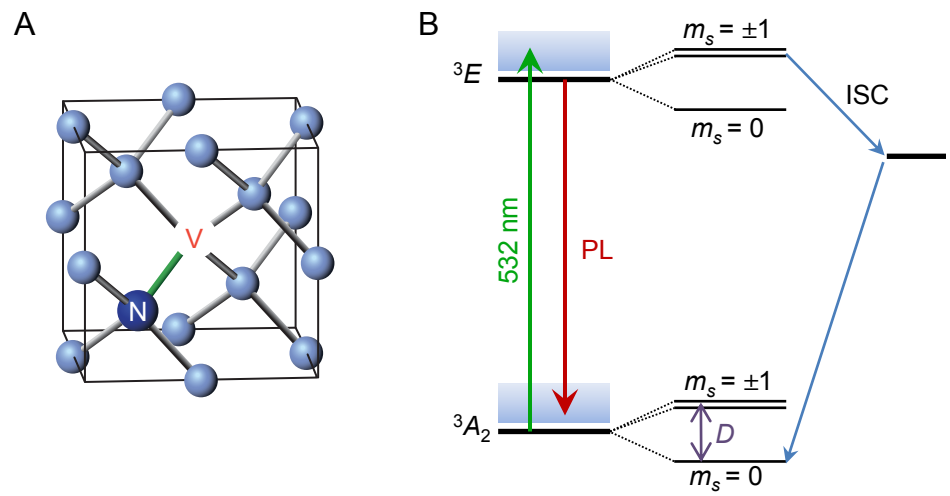

Figure 1.1: The diamond NV center. (*A*) Atomic structure of the NV center, with a substitutional nitrogen neighboring a vacancy. (*B*) Energy level diagram of the negatively charged NV center in diamond, showing relevant levels. The $^3A_2$ ground state is expanded to show the spin sublevels split by the zero-field splitting, D. The ^3E excited state is similarly split into a spin triplet. The spin system is optically excited by 532 nm laser into the excited state (^3E), where it has a spin-dependent probability of either returning to the ground state with a red-shifted photoluminescence (PL) or decaying non-radiatively through an intersystem crossing (ISC). (*A*) is reprinted by permission from Macmillan Publishers Ltd: *Nature Physics* [13], copyright 2005.

energy level structure, shown in Fig. 1.1*B*, consists of a ground-state spin triplet with lowest-energy spin sublevel $m_s = 0$ along with two $m_s = \pm 1$ spin sublevels [14, 15], which are nominally degenerate at zero magnetic field and energetically higher than $m_s = 0$ by the crystal field splitting, $D = 2.87$ GHz. The energy of the NV center spin system is magnetically sensitive, much like that of its classical analogue, the magnetic dipole. Specifically, a magnetic field $\mathbf{B}$ will shift the energy of the NV center's spin states according to the ground-state Hamiltonian,

$$\hat{H}_{\mathrm{NV}} = D\hat{S}_z^2 + g\mu_{\mathrm{B}}\mathbf{B}\cdot\hat{\mathbf{S}}, \tag{1.1}$$

where $g = 2$ is the electronic g-factor, μ_{B} is the Bohr magneton, and $\hat{\mathbf{S}}$ is the

electronic spin-1 operator. The measurement of spin energy eigenvalues in the presence of a magnetic field is the experimental basis for magnetic sensing using NV centers. The optical read-out of the spin state is possible because the $m_s = \pm 1$ states have a higher probability of a non-radiative transition via an intersystem crossing (ISC) through a series of singlets [16–18], so I_{PL} is lower in these states than in the brighter $m_s = 0$ state. Control of the spin state is achieved with a combination of optical and microwave pumping: optical excitation initializes the system into the $m_s = 0$ state through the same ISC, while a microwave field resonant with the energy splitting between the $m_s = 0$ and the $m_s = +1$ or -1 states will coherently rotate the spin into a superposition of the spin sublevels, which we detect as a darker I_{PL}. In continuous wave ESR measurements, the photoluminescence intensity (I_{PL}) is read out under the continuous application of both the 532 nm laser and microwave fields, leading to resonances in the observed intensity as the applied microwave field is swept in frequency across the spin sublevel transitions.

Magnetometry with NV centers

The room temperature quantum coherence and optical addressability of negatively charged nitrogen-vacancy (NV) color center spins in diamond [19] make NV centers particularly effective for a variety of sensing applications. In particular, the nitrogen-vacancy center in diamond is gaining interest for its sensitivity to magnetic fields. Degen [20] and Taylor et al. [21] proposed its use as a high-sensitivity scanning magnetic field sensor with nanoscale resolution. The spin-dependent fluorescent readout of ground-state electron-spin resonance (ESR) transitions in NV centers forms the basis for magnetometry. Balasubramanian et al. [22] and Maze et al. [23] demonstrated this magnetic sensitivity: Maze et al. demonstrated

ac magnetometry using both bulk diamond and 30 nm monocrystalline nanodiamonds deposited on a coverslip, and Balasubramanian et al. glued a nanodiamond to a scanning probe tip to scan a magnetic field, demonstrating high spatial resolution scanning probe magnetometry. Schoenfeld and Harneit [24] used an immobilized nanodiamond to measure the magnetic field of a scanned magnetic microwire. They also implemented a software lock-in to a frequency-modulated microwave signal to increase the signal to noise ratio. Rondin et al. [25] attached a nanodiamond to a scanning probe tip and used a software lock-in for magnetic field mapping. They also demonstrated that the drop in NV center fluorescence intensity in the presence of an off-axis magnetic field can be used for magnetic field mapping without ESR. Maletinsky et al. [26] fabricated a high-purity diamond probe and demonstrated its use for scanning an NV sensor to image magnetic fields.

Arcizet et al. [27] attached a single-NV nanodiamond to a silicon carbide nanowire (a nanomechanical resonator) which was itself attached to a tungsten tip. In a strong magnetic field gradient, the magnetic field measured by the NV in the nanodiamond depends upon the position of the nanowire as it oscillates, and through this they demonstrated magnetic coupling of the NV spin to the nanowire motion.

A common theme in many works is **nanodiamond positioning** using scanning probe tips [20–22, 25–32]. Hall et al. [32] suggest that an NV probe could be valuable for monitoring ion channel function.

Maertz et al. [33] showed the use of diamond for **vector magnetometry**: the ability to measure every component of the local magnetic field. Their approach uses a bulk diamond that has a very dense population of NV centers such that the optical ESR measurement encompasses the contributions

of four known orientations of NV centers in the diamond crystal lattice. The magnetic field projection onto the NV centers varies over these orientations such that the three components of the magnetic field can be determined. The three-dimensional magnetic field was mapped by scanning the excitation beam over the diamond. (See also Ref. [34].) Pham et al. [35] used a similar vector magnetometry method, but N_2^+ ions were implanted to create a two-dimensional layer of NV centers in the bulk diamond, and a CCD camera was used for wide-field fluorescence detection and hence wide-field magnetometry.

In addition to magnetic sensing, diamond NV centers may become useful as electric field [36] and temperature [18] probes.

1.3 Optically trapped diamonds

Laser-based optical trapping is another method of precise nanopositioning, but it occurs without physical contact. Optical trapping provides a means of positioning nanodiamonds, especially in a liquid environment, and it is better suited for accessing microfluidic channels than scanning probe tip techniques. It may also open the door to position control of nanodiamond sensors inside biological cells.

Here I will discuss other works in which diamond particles are optically trapped, including Sun et al. [37], Robledo's dissertation [38], and a preprint by Geiselmann et al. [39].

Rotational control of trapped microdiamonds

In the work of Sun et al. [37], a single-beam optical tweezers apparatus trapped single 15–25 μm diamond particles. Due to the irregular shapes of

these particles, when the net force was balanced in the trap, the net torque applied by the laser was not necessarily balanced, such that the laser drove rotation of the microdiamonds. By measuring the intensity of forward-scattered light or by imaging with CCD, the frequency of rotation was measured, varying from 0.5 to 100 Hz. The rotation rate was proportional to trapping beam power and also depended upon particle shape, proximity to an interface, and the trapping medium. By adjusting the position of the trap with respect to a water-air interface, the torque was balanced such that the particle stopped rotating. Similarly, the direction of rotation could be controlled for most but not all particle shapes by adjusting the laser focal plane.

Micro- and nanodiamonds trapped in gaseous medium

Robledo [38] used an optical trap in the tradition of atomic physics (as opposed to biophysics) in which the diamond particles were trapped in gaseous medium with the option of cooling trapped particles down to 4 K. The trap was used in both a single-beam configuration and a counter-propagating dual-beam configuration with a 785 nm laser. A piezo buzzer shook a funnel to release several particles to the trap. The diamond particles formed an agglomerate at the trapping volume. The trapped nanodiamonds were confined to a volume of 0.32 μm × 0.56 μm × 0.61 μm. Based on observations of fluorescence intensity, Robledo suspected that in some cases nanodiamonds exited the trap in steps until only one particle remained. Robledo trapped diamond particles at a series of sizes (0–50 nm, 0–250 nm, 250–500 nm, 3–5 μm) with a series of trapping powers (1 × 5 mW to 2 × 100 mW) at both 300 K and 77 K (in He atmosphere at 25 mbar), with pressure varying from 5 mbar to 1000 mbar, and in He and N_2 atmosphere. His trapping time was longer

than 24 h. The fluorescence spectrum of the trapped nanodiamonds shows a broad peak at 625 nm with no indication of the presence of NV centers.

Single-NV nanodiamond trapping with a dual-beam optical trap

In the preprint of Geiselmann et al. [39], a counter-propagating dual-beam trap is used to optically trap a single nanodiamond of about 60-70 nm diameter in water. Antibunching measurements indicate that they hold a single NV center in the trapped nanodiamond and ESR measurements of the trapped nanodiamond show the Zeeman shift in response to an external magnetic field. Their apparatus includes a 3-axis external electromagnet system, which allows them to determine the orientation of the trapped NV center. They find that the NV orientation is unchanged within an error range of 10° over a period of 30 minutes. In addition, when the trapped single-NV nanodiamond is rastered over a TiO_2 channel waveguide patterned on a glass substrate, the coherence lifetime decreases from ~17 to ~15 ns near the waveguide. Since they expect the lifetime is inversely proportional to the local density of photon states (LDOS) in the waveguide, this measured lifetime decrease corresponds to a measurement of the LDOS.

1.4 Organization

This dissertation is organized as follows. Chapter 2 contains an introduction to optical tweezers and a detailed description of the optical tweezers apparatus. Chapter 3 gives a description of the confocal fluorescence microscope and measurements of NV centers in nanodiamonds. In Chapter 4, we look at the electron spin resonance of nanodiamonds, both optically trapped and adsorbed on a coverslip. Chapter 5 combines the techniques described in

Chapters 2–4, using optically trapped nanodiamonds for magnetometry.

♦♦♦

Chapter 2

Optical tweezers

An optical trap provides the ability to position particles in solution [40]. Since fluorescent nanodiamonds are nanoscale sensors, it is useful to be able to position them at a variety of locations. Therefore we built an optical tweezers apparatus and used it to trap fluorescent nanodiamonds in solution.

2.1 Theory of optical trapping

Optical trapping often seems a mystery at first. How can a single laser beam hold anything? There are two modes of explanation. The first is the ray-optics approach, in which we argue that conservation of momentum provides the impulse to keep the trapped particle in place. The second is the induced dipole approach, in which we argue that the electric field of the beam induces a dipole in the particle, and this dipole is attracted to the highest electric field gradient. The ray optics approach is best suited for large particles with $a \gg \lambda$, where a is the radius of the trapped particle and λ is the laser wavelength. Conversely, the induced dipole approach [41] is best suited for small particles with $a \ll \lambda$. For mid-sized particles, neither approximation is

valid, and generalized Lorenz-Mie light-scattering theory [42] may be useful.

2.1.1 Mie regime: The ray-optics approach

In the Mie regime, the laser beam is considered to be a set of rays that are parallel when entering the objective. The objective focuses these rays to a point. A bead in these rays will cause the rays to reflect and refract at the interface between the bead and the medium. For the full equation of the trapping force, see Ref. [43, Eq. 6]. The trapping force arises from the conservation of momentum. Sketching the refraction of the rays at the interfaces of the bead and considering the momentum changes can help provide an intuitive understanding of the mechanism of three-dimensional trapping, as shown in Fig. 2.1.

2.1.2 Rayleigh regime: The induced dipole approach

In the Rayleigh regime, the small particle ($a \ll \lambda$) is treated as a point dipole. The laser beam induces the dipole $\mathbf{p} = \alpha\mathbf{E}$ in the particle, where $\mathbf{E}$ is the electric field of the beam and α is the polarizability of the particle, as given by the Clausius–Mossotti equation. This discussion follows Ref. [43].

The force of a tightly focused beam on the particle can be decomposed into the gradient force and the scattering force:

$$\mathbf{F}_{\text{Rayleigh}} = \mathbf{F}_{\text{grad}} + \mathbf{F}_{\text{scatt}}.$$

The gradient force is given by

$$\mathbf{F}_{\text{grad}} = \frac{\alpha}{2}\nabla\langle E^2\rangle.$$

(See also Ref. [44, Eqs. 2.2–2.4].) The scattering force points along the propa-

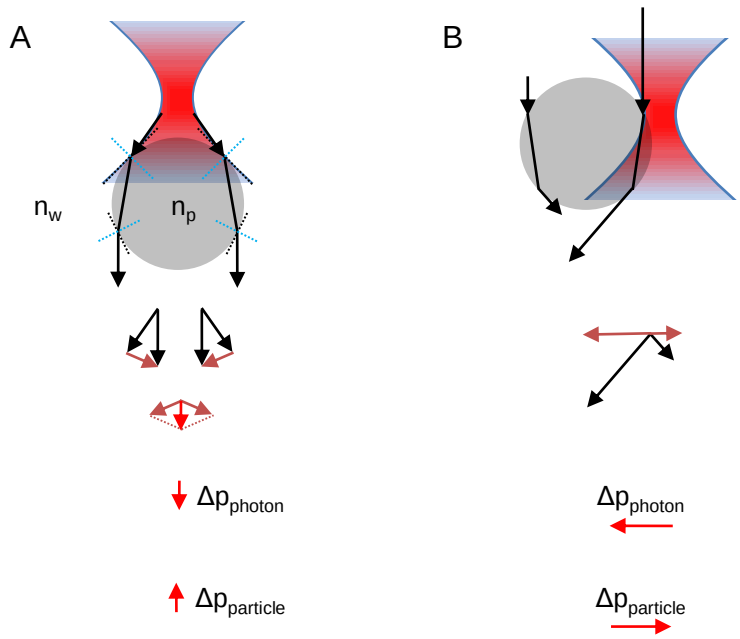

Figure 2.1: The ray-optics interpretation of axial (*A*) and lateral (*B*) optical trapping. Light is refracted through a transparent bead with index of refraction $n_p > n_w$, where n_w is the index of the trapping medium. The momentum change of the light causes an equal and opposite momentum change of the bead, which serves to push the bead toward the focus of the laser. Here the trapping beam is shown directed downwards. (*A*) If the bead is axially displaced from the beam focus, the light rays will refract in such a way to pull the bead toward the focal plane. (*B*) If the bead is laterally displaced from the beam focus, the light rays in the center of the beam are stronger than the rays at the edge of the beam due to the Gaussian beam profile, and the central rays will refract in such a way to pull the bead toward the beam focus. Figure courtesy of Benjamín J. Alemán.

gation direction of the incident light and is given by

$$\mathbf{F}_{\text{scatt}} = n_w \frac{\langle \mathbf{S} \rangle \sigma}{c},$$

where $\langle \mathbf{S} \rangle$ is the time-averaged Poynting vector and σ is the scattering cross section, given by

$$\sigma = \frac{8}{3}\pi (ka)^4 a^2 \left(\frac{m^2 - 1}{m^2 + 2} \right)^2,$$

where $k = 2\pi n_w / \lambda$ is the wavenumber of the beam, a is the particle radius, and $m = n_p / n_w$ is the index of refraction of the particle relative to the index of the medium.

The gradient force holds the particle in the trap while the scattering force pushes the beam out of the trap. Therefore the high numerical aperture objective is crucial for obtaining a sufficiently strong field gradient $\nabla \langle E^2 \rangle$ to overpower the scattering force.

2.1.3 Gaussian potential well in the Rayleigh regime

The single-beam optical trap potential well W is proportional to the laser intensity I according to [45]

$$W(\mathbf{r}) = -\frac{3V_1(n_p^2 - n_w^2)}{2c(n_p^2 + 2n_w^2)} I(\mathbf{r}), \tag{2.1}$$

assuming the size of the particle is much smaller than the laser wavelength (i.e. the Rayleigh regime) and ignoring the back-action of the trapped particles on the field, where

$W(\mathbf{r})$	is the trapping potential well,
$I(\mathbf{r})$	$= I(r, z)$ is the time-averaged laser intensity in watts per unit area,
V_1	is the single-particle volume, given by $\frac{4}{3}\pi a^3 = 210\ \text{nm}^3$ for 100 nm particles,

n_p is the particle's refractive index, given by 2.419 for diamond particles,

n_w is the refractive index of the trapping medium, given by 1.333 for water at room temperature, and

c is the speed of light.

We see that a larger particle will experience a deeper trap and also that the high index of refraction of diamond contributes to a deeper trap compared to other materials such as polystyrene. For trapping 100 nm diamonds in water, Eq. (2.1) evaluates to $W(\mathbf{r}) = (-1.1 \times 10^{-12}\ \mathrm{nm}^2\mathrm{s})\ I(\mathbf{r})$.

Assuming a perfect TEM_{00} mode with no astigmatism or other aberrations, the time-averaged laser intensity $I(r,z)$ is a Gaussian in the lateral directions [46],

$$I(r,z) = \frac{2P}{\pi w(z)^2} \exp\left(-\frac{2r^2}{w(z)^2}\right) \tag{2.2}$$

with a radial beam width given by [47]

$$w(z) = w_0\sqrt{1+\left(\frac{z}{z_R}\right)^2} \quad \text{and} \quad w_0 = \frac{\lambda}{\pi \tan\theta_0}, \quad \text{where} \tag{2.3}$$

r is a cylindrical coordinate giving the distance from the optical axis,

z is a cylindrical coordinate equal to zero at the focus, with the z-axis pointing along the propagating beam,

P is the beam power,

$w(z)$ is the radius of the beam at coordinate z,

w_0 $= w(0)$ is the beam waist radius,

z_R $= \pi w_0^2/\lambda$ is the Rayleigh range, which is half the depth of focus, and

$2\theta_0$ is the angular width of the diverging beam, with $\mathrm{NA} = n\sin\theta_0$, where

NA is the numerical aperture of the objective, which is 1.3 for our 100x objective and

n is the index of refraction of the medium in which the objective is working, equal to 1.515 for the immersion oil.

Note that Eq. (2.2) is self-consistent in the sense that the beam power P is the integrated intensity at any given z: $P = \int_0^{2\pi} \int_0^{\infty} I(r,z)\, r\, dr\, d\phi$. Using the values for NA and n for our oil-immersion objective, the beam intensity is plotted in Fig. 2.2. Although the 532 nm beam is not used for trapping in our apparatus, its intensity profile is also a Gaussian and it is plotted for comparison.

With a known beam intensity profile, we can calculate the trap potential W according to Eq. (2.1), as shown in Fig. 2.3. This is a stable trap in three dimensions. It is common to approximate the trap potential as a harmonic potential well,

$$W(r,z) \approx -W_0 + \frac{1}{2}k_r r^2 + \frac{1}{2}k_z z^2,$$

with trap depth W_0 and trap stiffness values k_r and k_z. From a Taylor series expansion of Eq. (2.2), we approximate that

$$W_0 \sim \frac{2PC}{\pi w_0^2}, \qquad k_r \sim \frac{8PC}{\pi w_0^4}, \quad \text{and} \quad k_z \sim \frac{4PC}{\pi w_0^2 z_R^2}, \quad \text{where}$$

$$C = \frac{3V_1(n_p^2 - n_w^2)}{2c(n_p^2 + 2n_w^2)} \propto \alpha.$$

However, this laser intensity profile is an idealized approximation. No optical trap is perfectly aligned, and the approximations that facilitated these calculations are not very precise, especially in consideration of the high NA of the objective. To emphasize this point, I recalculate and plot the intensity in Fig. 2.4 using a non-paraxial approximation as found in Ref. [48, Eqs. 3–6]. In contrast to Eq. (2.2), the side-lobes resulting from the spherical Bessel

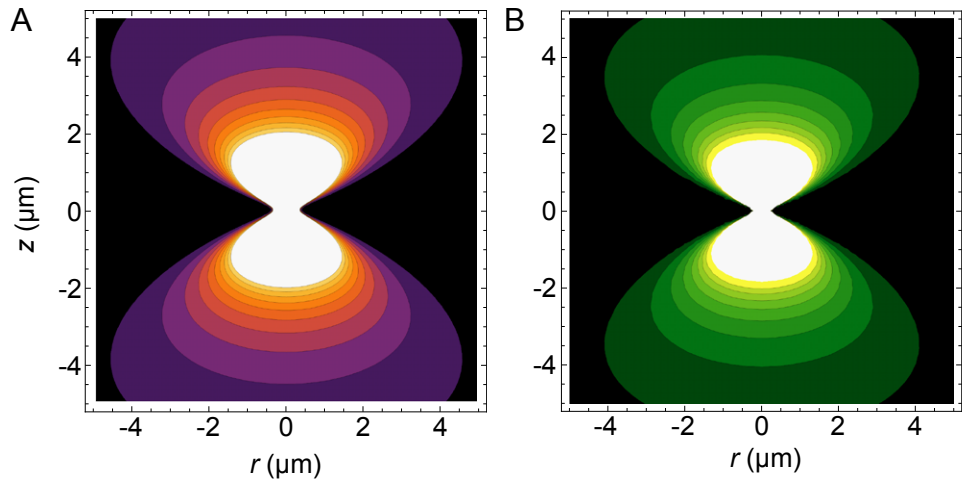

Figure 2.2: The time-averaged intensity of a Gaussian laser beam for (*A*) a 1064 nm and (*B*) a 532 nm laser beam, calculated from Eq. (2.2) with NA = 1.3 and $n = 1.515$. The beam angle is $\theta_0 = 59.1°$. The beam waist diameter is expected to be $2w_0 = 0.41$ μm for the 1064 nm beam and $2w_0 = 0.20$ μm for the 532 nm beam. The depth of focus is expected to be $2z_R = 0.24$ μm for the 1064 nm beam and $2z_R = 0.12$ μm for the 532 nm beam.

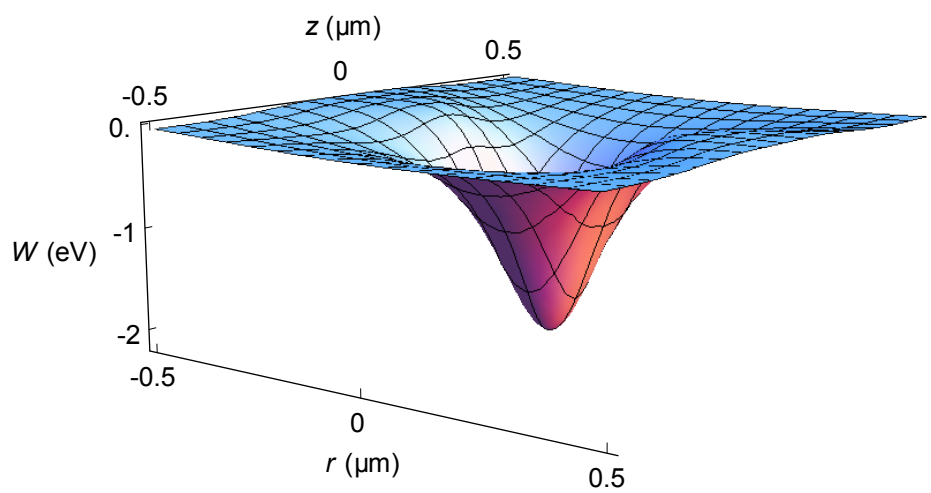

Figure 2.3: The trapping potential well W of a 20 mW, 1064 nm Gaussian laser beam trapping 100 nm diamond particles in water with a 1.3 NA objective in immersion oil ($n = 1.515$), calculated from Eq. (2.1) and using the calculated intensity shown in Fig. 2.2*A*.

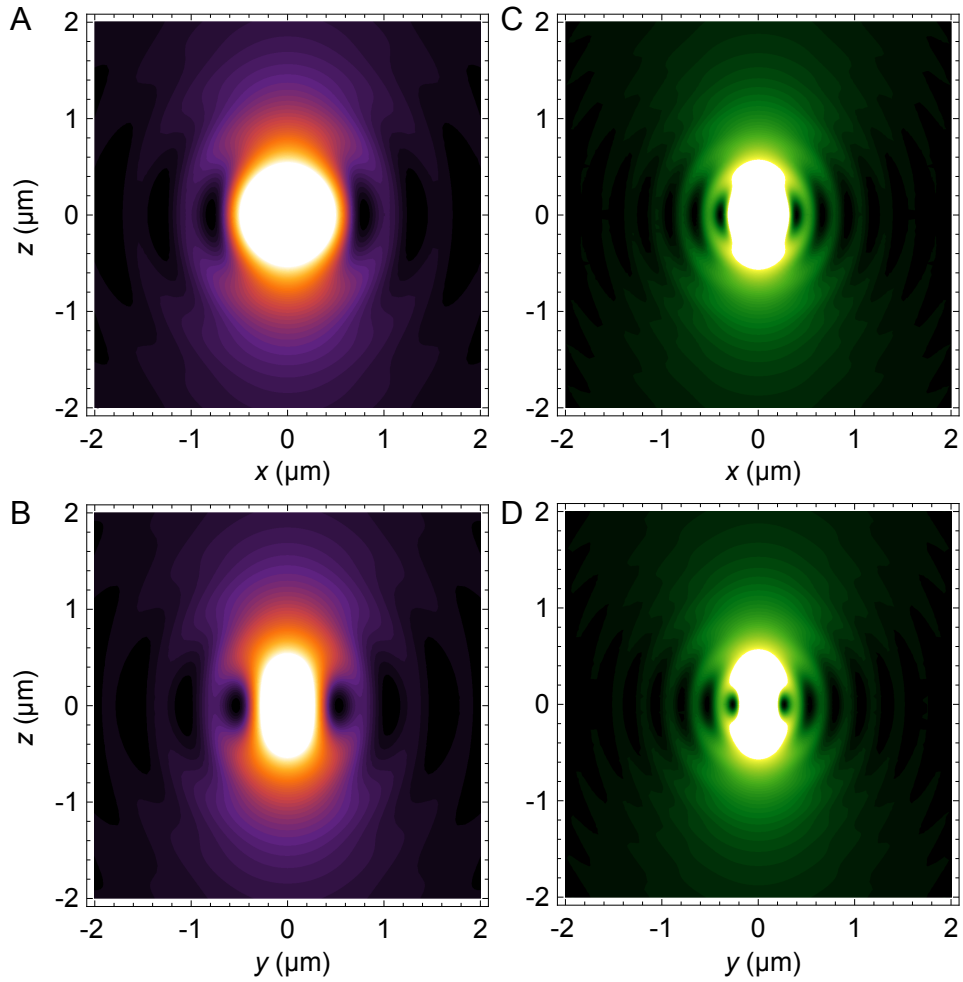

Figure 2.4: The calculated intensity (or, proportionally, the trapping potential well) of a linearly polarized, non-paraxial laser beam for (*A*-*B*) a 1064 nm and (*C*-*D*) a 532 nm laser beam, calculated from Ref. [48] with NA = 1.3 and $n = 1.515$.

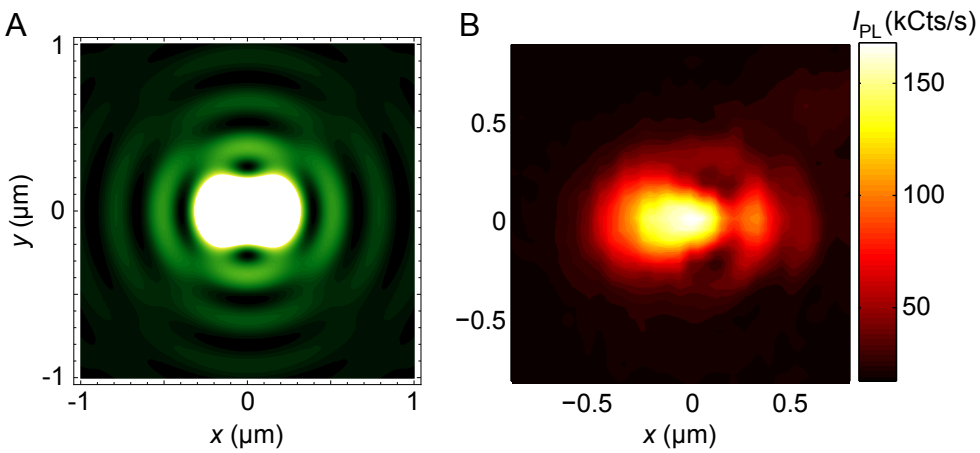

Figure 2.5: Comparison of a theoretical beam profile and the experimental fluorescence profile. (*A*) The calculated intensity of a linearly polarized, non-paraxial, 532 nm laser beam, calculated from Ref. [48] with NA = 1.3 and $n = 1.515$. (*B*) The spatial profile of the fluorescence of a single immobilized NV center excited with a 532 nm beam.

functions appear in this approximation. This is qualitatively similar to sidelobes I observe in two-dimensional scanned fluorescence measurements, as shown in Fig. 2.5. See Chapter 3 for a discussion of confocal fluorescence measurements. The best way to determine trap stiffness is to measure it empirically using the optical tweezers apparatus.

2.2 Instrument

We will discuss the optical tweezers instrument, including each optical component and its alternatives and the alignment and function of these components.

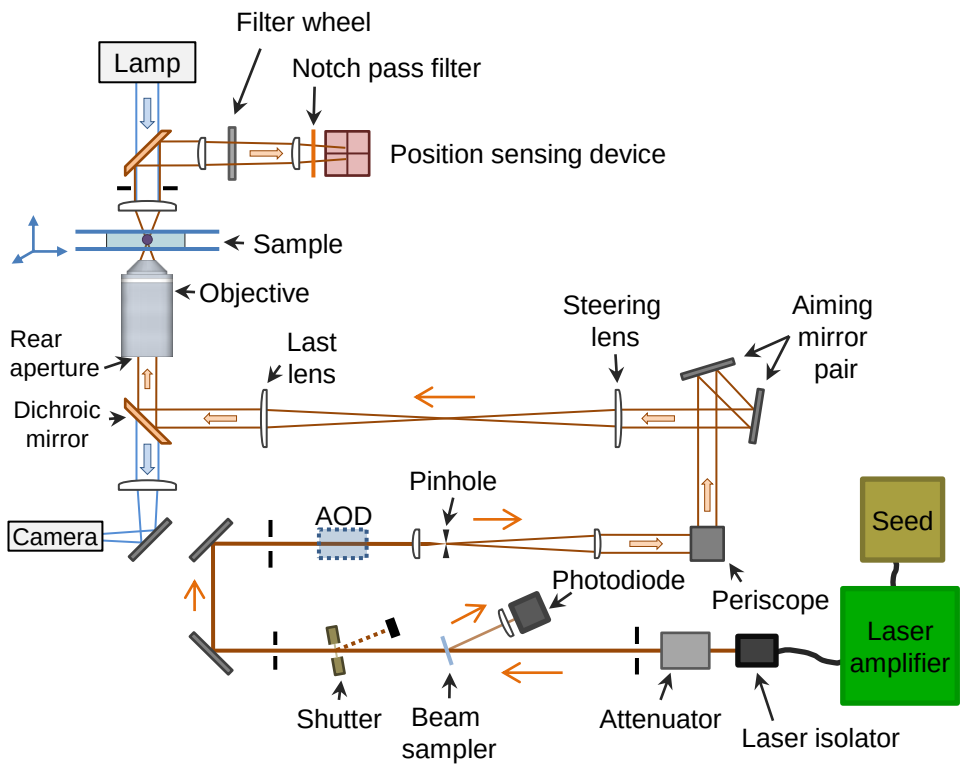

Figure 2.6: The optical tweezers apparatus. A 1064 nm beam is expanded, steered, then tightly focused through a high NA objective. The forward-scattered beam provides tracking of trapped particles. See Tables 2.1 and 2.2 for an ordered list of optical elements.

2.2.1 Optics

The optical tweezers apparatus is, at its essence, a tightly focused Gaussian laser beam. To obtain a tightly focused laser beam, the beam is expanded to slightly overfill the high-NA objective. The forward-scattered beam is collected for measurements of the position of the trapped particle.

Here I explain the purpose of each part in the optical trap apparatus and discuss alternatives. Figure 2.6 shows the optical tweezers apparatus. The elements of the optical tweezers apparatus are listed in order in Table 2.1. The elements of the position detection path are listed in order in Table 2.2. For

completeness, Table 2.3 lists additional equipment for the optical tweezers. For step-by-step instructions on how to build optical tweezers, see Refs. [49–51]. If you are building an optical apparatus, some basic optical alignment skills are covered in Ref. [52].

The **laser system** consists of an NP Photonics seed laser and a Nufern fiber laser amplifier, which outputs a 1064 nm beam with power up to 5 W. The 1064 nm wavelength is a common optical trapping wavelength because it is biocompatible [2, 53]. The amplifier requires two power sources; I use a Xantrex HPD 30-10 voltage source as the first and an ILX Lightwave LDX-3650 current source as the second. The amperage of this second power source controls the beam power. The manufacturer recommends running the second power source at the full 7 amps in order to maintain a stable beam power, but in many cases the beam power stability is not crucial and so we run the second power source at low (or zero) amperage to prevent the Nufern amplifier from overheating. The Nufern amplifier has the bad habit of occasionally turning itself off, and overheating is one of the potential causes. Other causes include having an insufficient seed laser or reflections of the beam returning to the amplifier. Both the seed laser status and the back reflection status are monitored by the Nufern amplifier and can be read as voltages from the Nufern cord. I have never seen back-reflections cause problems, possibly thanks to the **laser isolator**, but the seed laser did need to be returned to NP Photonics for repair once. In contrast to the reflection and seed laser status monitoring, the Nufern has no built-in monitoring for overheating. I added an external water-cooling system to the Nufern amplifier in order to decrease instances of overheating. The Nufern amplifier may also turn off if it is knocked (or if the table is knocked) or for no apparent reason. (It could be worse! It could turn *on* for no apparent reason!)

Table 2.1: Elements of the optical tweezer pathway, as shown in Fig. 2.6.

#	Item	Brand	Item number
1	Seed laser, 1064 nm	NP Photonics	Scorpion, FLM-50-0-1064
2	Trapping laser amplifier, 5 W, 1064 nm	Nufern	PM-ASA-SFA-5W-source, SUB-1151-13
3	Attenuator	Newport	935-3-OPT
4	Iris	Newport	ID-1.0
5	Beam sampler	Newport	10B20NC.3
	Lens, $f = 50.2$ mm	Newport	KPX082AR.33
	IR Photodiode	Thorlabs	DET10C
6	Shutter with foot pedal	Uniblitz	CS45S1T1 and 710R/F
7	Iris	Newport	ID-0.5 and MH-2P
8–9	Mirror pair	Newport	10D20ER.2 (qty:2)
10	Iris	Newport	ID-1.0
	Acousto-optic deflector (removed)	IntraAction	DTD-274HD6 with DVE-120 and DPA-502D
11	First expansion lens, $f = 50.2$ mm	Newport	KPX082AR.33
12	Pinhole, 50 µm with five-axis mount	Newport	910PH-50 with 910A and TSX-1D
13	Second expansion lens, $f = 250$ mm	Newport	KPX109AR.33 and TSX-1D
14–15	Mirror pair in periscope / beam steerer	Newport	13E20DM.10 (qty:2)
16–17	Aiming mirror pair	Thorlabs	BB1-E03 (qty:2) and TSX-1D
18	Steering lens, $f = 250$ mm	Newport	KPX202AR.33 and 460A
19	Last lens, $f = 250$ mm	Newport	KPX202AR.33 and 423
20	Trapping dichroic mirror and filter cube	Chroma	700dcspxr and 91020
21	Objective, CFI Plan Fluor 100x 1.3NA	Nikon	MRH01901
22	Immersion oil	Nikon	MXA20234

Table 2.2: Elements of the IR collection path for position detection, as shown in Fig. 2.6.

#	Item	Brand	Item number
1	Immersion oil	Nikon	MXA20234
2	Condenser, T-C-HNAO high NA oil lens	Nikon	MEL41410
3	Aperture diaphragm	Nikon	part of TE2000U
4	Dichroic mirror in T-CHA	Chroma	700dcspxr
5	First IR collection lens, $f = 200$ mm	Newport	KBX076AR.18
6	Filter wheel (neutral density)	New Focus (now Newport)	5215
7	Second IR collection lens, $f = 75.6$ mm	Newport	KPX088AR.18
8	PSD filter, 1064 nm notch pass	Chroma	z1064/10x
9	Position sensing device (PSD)	Pacific Silicon (now First Sensor)	DL16-7PCBA3, 10-026

Table 2.3: Items relating to the optical tweezers apparatus

Item	Brand	Item number
Piezostage	Physik Instrumente	P-517.3CL and E-710.4CL
Inverted microscope	AG Heinze / Nikon	TE2000U
Water chilling system	ThermoCube	10-200-1D-1-SW-EF-DI
Power meter & sensor	Coherent	33-0498-000 and 1098304
IR viewer	Find-R-Scope	FJW 84499A
IR cards	New Focus	5842
Laser safety glasses	Phillips Safety Products	LS-KG5-33

The **beam attenuator** (935-3-OPT, Newport) uses diffraction to controllably attenuate the beam. An alternative to the diffraction-based attenuator is a rotating-polarizer attenuator, as used in Ref. [54] and the related video, Ref. [55]. A rotating filter wheel is not a recommended alternative because even if the filters did not melt in the beam, the plastic mount would heat and melt when it rotated through the beam. The attenuation varies from about 50% to about 100%. If greater than 2.5 W laser output is desired, the diffracting attenuator should be removed. A motorized actuator can be installed in the diffracting attenuator if automated control is desired. We have used an open-loop actuator for this purpose, but open-loop actuators are generally a bad idea because the motion of the automated actuator is not repeatable. If automated control of the diffracting attenuator is desired, the photodiode could be used to measure the beam power for useful feedback to the actuator. An **iris** after the diffracting attenuator blocks the stray beams that result from the diffraction pattern.

The **beam sampler** sends a fraction of the beam to a **photodiode** so that the beam power can be measured at all times. A previous version of the beam path used a glass slide to sample the beam; however, I replaced it with a commercial beam sampler because a glass slide may distort the beam wavefront. The photodiode is battery-powered, which may be advantageous in terms of immediate convenience and price, but has the disadvantage that the batteries must be replaced. The output voltage from the photodiode is essentially linear to the beam power measured in watts up to ~250 mV.

The **shutter** is useful for turning the trap on and off. When the shutter is closed, the beam is reflected off the shutter blades into a beam dump. (I selected the shutter blades to ensure that they could withstand the laser beam power, and therefore they are quite reflective.) The foot pedal opens or closes

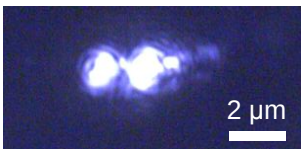

Figure 2.7: Micrograph of time-sharing the beam by rapidly alternating the AOD frequency. The beam is effectively split into two beams, imaged here on a platinum-coated glass slide. Here, the beam is not swept between the two deflections by the AOD; it jumps between them. This makes it possible to create multiple traps at different locations. Scale bar is approximate.

a switch to control the shutter state via the controller.

I have used an **acousto-optic deflector (AOD)** as a fast beam steerer. However, I removed it because it was more trouble than it was worth. I was concerned that the AOD was creating a Schaefer-Bergmann diffraction pattern [56, 57] and a crosshatching pattern [58], while I needed a Gaussian beam profile, and the AOD was not necessary because I was not in need of fast beam steering. That said, many groups benefit from a dual-axis AOD arrangement for applications such as time-sharing, where multiple trapping locations are maintained by rapidly changing the position of the laser (see Fig. 2.7 and Refs. [59, 60]), and force clamping, where the position of the trap is continually updated so that the force on a tethered bead is held constant [61, 62]. An AOD can also be used to rapidly turn the trap on and off, replacing an automated shutter, and to control the beam power, replacing an attenuator. The Schaefer-Bergmann diffraction pattern might be minimized by sending the beam through the AOD crystal at a position closer to the transducer [63].

When an AOD is used, the beam is sent through an acousto-optic crystal (tellurium dioxide). A piezoelectric transducer converts a radio frequency (rf) electrical signal into a sound wave that travels through the crystal, creating a

pattern of high and low optical density. The laser is diffracted by the Bragg angle [64],

$$\Delta\theta_{\text{deflection}} \approx \lambda \frac{\Delta f}{v_{\text{sound}}},$$

where λ is the beam wavelength in air, Δf is a change in the rf frequency, and v_{sound} is the speed of the acoustic wave in the crystal. A position calibration of the dual-axis AOD is shown in Fig. 2.8 and a power calibration is shown in Fig. 2.9. Multiple trapping beams could alternately be created by a liquid-crystal-based spatial light modulator [65]. The AOD is discussed more in the next section, particularly with regards to its placement in the beam path.

The **expansion optics** consist of two lenses of unequal positive focal lengths. The Nufern laser amplifier outputs a beam that is nominally 0.8 mm in diameter and nominally collimated and the beam needs to be expanded to slightly overfill the back aperture of the objective, which in our case is 6 mm in diameter. (Overfilling ensures that steering the beam won't walk the beam too far off the rear aperture of the objective, in case the steering optics are not perfectly conjugate to the objective rear aperture.) Naïvely, this means we need an expansion factor of slightly more than 7.5x. However, the beam is not perfectly collimated exiting the Nufern laser amplifier, so the beam will have expanded unintentionally by the time it arrives at the first expansion lens. In a previous version of the apparatus, I used a collimation lens pair earlier in the optical path (not shown in Fig. 2.6) to prevent the beam from expanding unintentionally, but I removed that lens pair because it was not necessary to avoid unintentional expansion prior to the intentional expansion, and excess lenses might increase aberration. To determine the amount of unintentional expansion, I removed all lenses from the optics path (including the expansion pair, the steering lens and last lens,

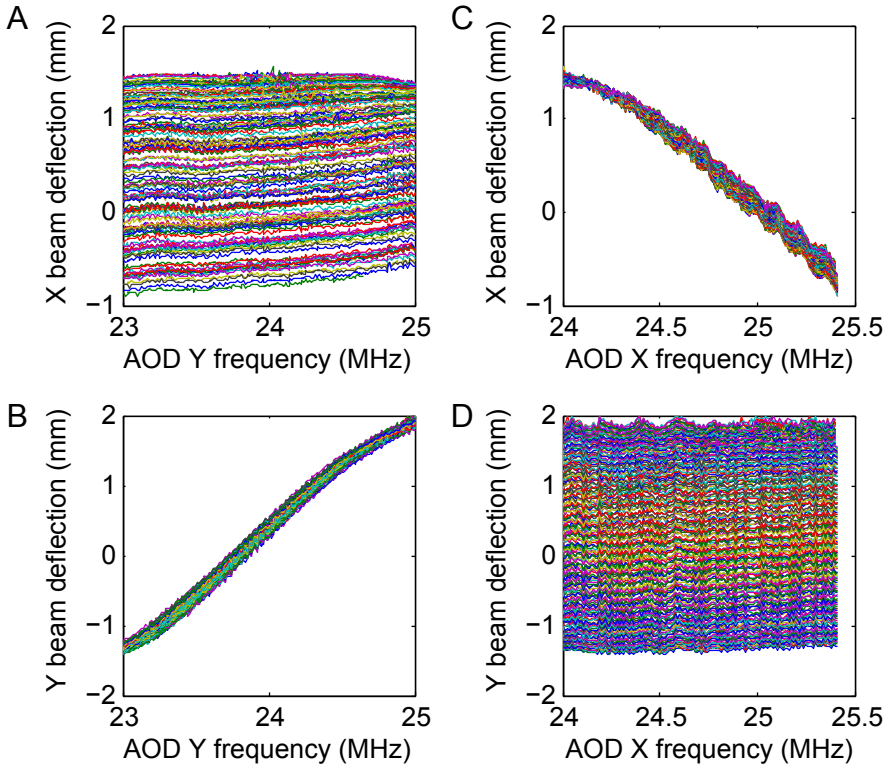

Figure 2.8: Position calibration of a dual-axis AOD. Here the beam deflection is measured at a location immediately after the AOD, without the use of lenses or the microscope objective. Nonlinear ripples in the response are likely due to standing waves created in the acousto-optic crystal [64]. To good approximation, the beam deflection in y only depends on the AOD y frequency and the beam deflection in x only depends on the AOD x frequency. Hence, the beam can be deflected to desired positions in both x and y using two perpendicular acousto-optic crystals.

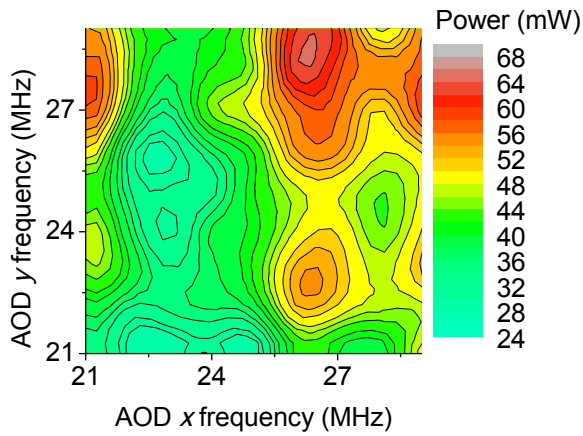

Figure 2.9: Power calibration of a dual-axis AOD. The first order deflected beam exiting the dual-axis AOD will be less powerful than the input beam, and this output power (plotted above) is not flat over the range of AOD rf frequencies. If the trapping beam must be equally intense at each deflection angle, this can be achieved by adjusting the amplitude of the rf frequency input to the transducer at each frequency using this calibration.

and the objective). With no lenses, I measured the $1/e^2$ radius of the beam at the sample location using a knife edge width technique. In this technique, a blade is placed in the beam and the beam power P_{meas} is measured after the beam has clipped on the blade edge. A Gaussian beam will fit to [66]

$$P_{\text{meas}} = \frac{P_0}{2}\left[1 \pm \text{erf}\left(\frac{\sqrt{2}(x - x_0)}{R}\right)\right], \tag{2.4}$$

where

P_0 is the beam power prior to the blade,

erf is the error function,

x is the blade position,

x_0 is the position of the blade when centered on the beam, and

R is the $1/e^2$ radius of the Gaussian beam.

Using a knife edge at the sample location, I found that, in the absence of lenses, the beam expanded from a nominal diameter of 0.8 mm exiting the Nufern amplifier to a measured diameter of $2R = 5.1$ mm at the sample lo-

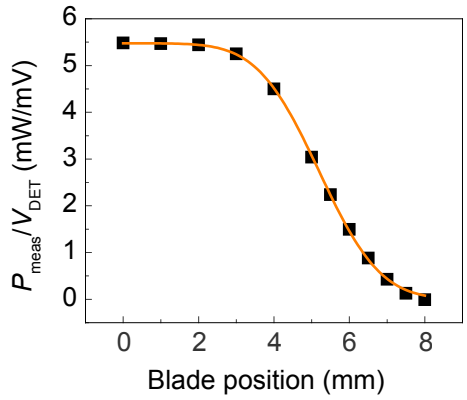

Figure 2.10: Gaussian beam expansion measured with the knife edge technique with all lenses removed. The beam, nominally collimated when exiting the Nufern amplifier, nevertheless diverges unintentionally when all lenses are removed. A blade was mounted on a linear stage and placed at the sample location, and the beam power P_{meas} was measured after the beam had clipped on the knife edge. This was divided by the measured IR photodiode voltage, $V_{\text{DET}} \propto P_0$, to remove the confounding effect of laser power fluctuations. By fitting (orange curve) to Eq. (2.4), the beam radius was determined to be 2.57 mm $\pm$ 0.04 mm.

cation (Fig. 2.10). Without the collimation lens pair to reduce unintentional expansion prior to the expansion optics (i.e. with the optics shown in Fig. 2.6), the desired expansion factor for the expansion optics was determined to be about 5x. Combined with the unintentional expansion, this achieved the desired overall expansion factor. It is also possible that beam quality might be improved by shortening the path length between the expansion optics and the laser output.

As an alternative to a lens pair for the expansion optics, a commercial beam expander with adjustable expansion factor can be useful for this application. We have a Zoom Beam Expander (NT64-414, Edmund Optics) with a variable expansion factor ranging from 2x to 8x. The benefit of an adjustable beam expander is that the expansion factor can be adjusted without replacing lenses. The disadvantage is that the expander is more complicated to use

and introduces more lenses to the beam path, so I opted for the simplicity of a two-lens beam expander that also had the advantage that it provided a laser focus location for a pinhole.

The purpose of the **pinhole** is to spatially filter the beam so that it is a Gaussian beam with a TEM_{00} mode. The alternative is to remove the pinhole and rely on the single-mode fiber that outputs the beam from the Nufern amplifier to provide the proper mode.

The **periscope** serves to raise the IR beam to the level of the trapping dichroic mirror mounted inside the Nikon microscope. Now that the beam has been expanded, care must be taken to ensure that the beam does not clip on any of the optics. Although the beam is still small enough that one-inch diameter mirrors would be sufficiently large, even when mounted at 45° in the periscope, any adjustment could cause the beam to clip on a one-inch mirror, so I chose larger elliptical mirrors.

Aligning the beam into the microscope objective is a crucial consideration for optical tweezers. Four mirrors in a row might seem excessive, since the beam alignment could be accomplished entirely with the periscope, but I prefer gimbal-mounted mirrors for the **aiming mirror pair**. A gimbal mount has a pivot at the center of the mirror so that adjusting the angle of the mirror will not cause other parameters of a beam's position to change if the beam is centered at the pivot point. The two aiming mirrors together provide four degrees of freedom for adjusting the alignment of the beam. In addition, I mount the second aiming mirror on a linear stage because the second aiming mirror needs to be perfectly opposite the trapping dichroic mirror. An alternative to using the linear stage might be to use larger mirrors.

The **steering lens** provides a means of adjusting the position of the trap. If three degrees of freedom are desired, then the steering lens should be

mounted on a 3-axis stage. Once the steering lens focuses the beam, the **last lens before the microscope** collimates the beam.

The **trapping dichroic mirror** is mounted at 45° in a filter cube turret built into the TE2000U microscope. As such, I have used a dichroic that is shaped for mounting in a Nikon filter cube. An alternative would be to build a custom mount for the dichroic, which could be designed with increased stability, if necessary, and which would permit the mounted dichroic to be circular in shape instead.

The **objective** has a numerical aperture (NA) of 1.3, which is sufficiently high to achieve optical trapping. According to Ref. [2, Table 1], the CFI Plan Fluor 100x objective has a transmission of 61% ± 5% at 1064 nm. In order to achieve the high numerical aperture, the objective is designed for use with **immersion oil** with a refractive index of 1.515. I used Nikon-brand immersion oil. This oil had a fluorescence of approximately 400 kCts/s when I focused the 532 nm beam, attenuated to about 16 μW, into the oil. Fortunately, the oil's fluorescence is minimal when the beam is focused through a glass **coverslip** to the sample.

And here we arrive at the trapped particle. The optics of levitating a particle with light are discussed in Section 2.1.

The forward-scattered 1064 nm beam has an interference pattern that provides information about the trapped particle position. The beam traps a particle at the beam focus in solution in the **sample chamber**. The beam continues onwards after its crucial job is completed. It passes through the glass top of the sample chamber, the **immersion oil**, and the **condenser lens**. (I used both an oil-immersion objective and an oil-immersion condenser lens, so the sample chamber is surrounded with oil on bottom and top.) An **aperture diaphragm** is located at the back focal plane of the condenser lens. The

beam passes through this aperture, which may be partially closed for the illumination path but which must be open (crucially!) for the wide beam to pass through for particle tracking.

A **dichroic mirror** serves to reflect the 1064 nm beam away from the illumination path. The dichroic is mounted inside a tube-like Nikon part called a T-CHA. I used a 45° optics mount held inside the T-CHA with a customized attachment. The dichroic was too thin to use a set screw to hold it in the mount, so I used a retaining ring.[1]

The T-CHA was modified with a hole to allow the beam to exit to the side. The beam passes through **lenses** and a **filter wheel** and arrives at the **PSD**. The placement of these lenses and the PSD is discussed in Section 2.2.2. The uses of the PSD (and the filter wheel) are discussed in Section 2.3.

2.2.2 Conjugate focal planes

A crucial consideration in designing optical tweezers is the concept of conjugate focal planes. Two planes are conjugate to each other if points at one plane are imaged at the other. A camera will image all of its conjugate planes, including the surface of the light-sensitive element, which is why it will image dust particles on the surface. (Samples placed directly on the camera surface can also be imaged without a camera lens [67].)

[1] Unfortunately, the retaining ring blocks some of the optical path, which is clearly visible when viewed with the microscope's Bertrand lens. Position tracking and illumination might both be improved if this dichroic were replaced with a dichroic that was thick enough to be mounted with a set screw rather than a retaining ring. However, it is a small concern because the system is functional.

Definition

We use a geometrical ray optics approach following Ref. [68, Chapter 4]. If a ray begins at height y_0 and angle α_0 at the first plane, P_0 then it will arrive at the second plane, P_f, according to

$$\begin{aligned} y_f &= A_{f0} y_0 + B_{f0} \alpha_0 \\ \alpha_f &= C_{f0} y_0 + D_{f0} \alpha_0, \end{aligned} \tag{2.5}$$

where we have made the small-angle approximation that $\tan \alpha_0 \approx \alpha_0$. The constants A_{f0}, B_{f0}, C_{f0}, and D_{f0} are determined by the specific optics between P_0 and P_f. A laser beam can be thought of as a set of rays, which are parallel to each other with the same α where the beam is collimated, and which come together at a single height y at a focus.

Two planes P_0 and P_f are conjugate to each other if and only if $B_{f0} = 0$. In this case, y_f is independent of α_0. As a more intuitive definition, if you arrange to have a laser beam focused at P_0 then all of its rays are at the same y_0 and so they will all arrive at some particular y_f, regardless of their angle, which means that the laser beam will also be focused at P_f. Hence, two planes are conjugate to one another if a laser focused at one plane is also focused at the other.

In some cases, however, it is useful to arrange for two planes to be conjugate to each other where no beam is focused. For example, the steering lens of the optical trap needs to be conjugate to the objective rear aperture, but the trapping laser is not focused at either location.

Conjugate planes in optical microscopy

Köhler illumination is a common technique in optical microscopy for uniform illumination of a sample, despite the uneven lamp source. The

lamp source is unfocused at the sample so that light from every part of the lamp reaches each point of the sample [69]. To achieve this, there are two sets of conjugate planes. The first is the image-forming conjugate plane set: the sample plane is conjugate to the camera or the retina (when imaging by eye) as well as the field diaphragm. Therefore the sample is focused for imaging and the field diaphragm is visually focused to achieve proper Köhler alignment of the illumination path. The second is the illuminating conjugate plane set: the lamp filament is conjugate to the objective rear aperture, the camera lens or the microscope exit pupil, and the condenser aperture diaphragm, as shown in Ref. [70]. Even in the absence of Köhler illumination, these two sets of conjugate planes are important in optical trapping because the trapping beam focus is in the first conjugate plane set while beam steering and position detection are in the second set [2, Fig. 2].

Ray-transfer matrix

When you wish to arrange to have two planes be conjugate to one another, system ray-transfer matrices are valuable for calculating appropriate optics. We rewrite the ray transfer equations (2.5) in matrix notation:

$$\begin{bmatrix} y_f \\ \alpha_f \end{bmatrix} = M_{f0} \begin{bmatrix} y_0 \\ \alpha_0 \end{bmatrix}, \quad \text{where} \quad M_{f0} = \begin{bmatrix} A_{f0} & B_{f0} \\ C_{f0} & D_{f0} \end{bmatrix}.$$

The elements of M_{f0} describe the optics between P_0 and P_f, where again B_{f0} equaling zero is the necessary and sufficient condition for these two planes to be conjugate to each other. We determine the matrix M_{f0} by multiplying the matrices of the optical elements between P_0 and P_f. For example, a translation of length L has a matrix $M_t(L)$ and a thin lens of focal

length f has a matrix $M_l(f)$ as follows:

$$M_t(L) = \begin{bmatrix} 1 & L \\ 0 & 1 \end{bmatrix} \qquad \text{and} \qquad M_l(f) = \begin{bmatrix} 1 & 0 \\ -\frac{1}{f} & 1 \end{bmatrix}.$$

More ray-transfer matrices are available in Ref. [68]. The system matrix M_{f0} is built up from the matrices of each optical element,

$$M_{f0} = M_N M_{N-1} \cdots M_2 M_1,$$

where M_1 is the matrix of the first optical element after P_0 and M_N is the matrix of the last optical element before P_f. In addition to providing a convenient means of ray-tracing, this approach provides a notation for describing a series of optical elements mathematically rather than pictorially.

In an optical path, if P_1 and P_2 are conjugate to each other, and P_2 and P_3 are conjugate to each other, then P_1 and P_3 are conjugate to each other, because

$$M_{31} = M_{32} M_{21} = \begin{bmatrix} A_{32} & 0 \\ C_{32} & D_{32} \end{bmatrix} \begin{bmatrix} A_{21} & 0 \\ C_{21} & D_{21} \end{bmatrix} = \begin{bmatrix} A_{21} A_{32} & 0 \\ A_{32} C_{21} + C_{32} D_{21} & D_{21} D_{32} \end{bmatrix},$$

where we obtain $B_{31} = 0$, as required. This is the transitive property of conjugate planes, and it enables us to speak of sets of planes that are all conjugate to each other.

Beam steering and the particle-tracking collection path

A **steering lens** is a practical example of conjugate focal planes. We wish to be able to control the angle of approach of a laser entering the back of the objective, but we do not want the laser beam to walk off the back opening of the objective. Therefore, the steering element must be conjugate to the rear aperture of the objective. We achieve this by arranging the lenses as shown in

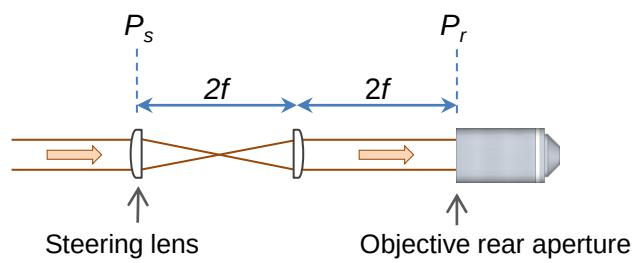

Figure 2.11: If the steering lens is at plane P_s and the rear aperture of the objective is at plane P_r, then these two planes will be conjugate to each other if the two lenses shown (the steering lens and the last lens of the IR pathway) both have a focal length f, are separated by distance $2f$, and if the rear aperture of the objective is a distance $4f$ from the steering lens. Mirrors (including the dichroic mirror) are neglected in this diagram.

Fig. 2.11. Then the system matrix from P_s to P_r is

$$M_{rs} = M_t(2f)M_l(f)M_t(2f)M_l(f) = \begin{bmatrix} -1 & 0 \\ 0 & -1 \end{bmatrix}.$$

Since the element B_{rs} is zero, this lens arrangement puts the steering lens conjugate to the rear aperture of the objective, as desired.

An alternative to the steering lens arrangement, some optical tweezers use a steering mirror; in this case the steering mirror must be conjugate to the objective rear aperture. This is most commonly achieved by placing two lenses between the steering mirror and the objective rear aperture, with spacings as given by the following ray-transfer matrices:

$$M_{rm} = M_t(f)M_l(f)M_t(2f)M_l(f)M_t(f) = \begin{bmatrix} -1 & 0 \\ 0 & -1 \end{bmatrix}.$$

Again, this offers a geometry for which the element B_{rm} is zero and, as before, the distance between the steering element and the rear aperture of the objective is $4f$. However, the last lens of the IR pathway must be placed a distance f from the rear aperture of the objective in this steering mirror arrangement, in contrast to the steering lens arrangement where the last lens is

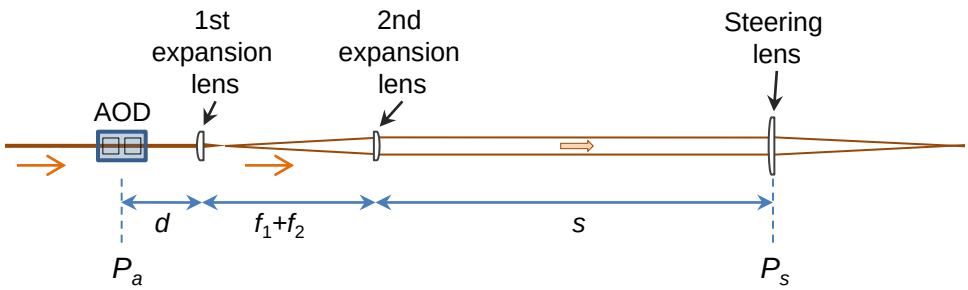

Figure 2.12: The acousto-optic deflector (AOD) must be conjugate to the steering lens. This diagram neglects mirrors that are present in the apparatus.

placed a distance $2f$ from the objective, as shown in Fig. 2.11. I chose to use a steering lens arrangement partly because the geometry of the commercial microscope made it impractical to position a lens close to the rear of the objective, so I would have needed lenses of very long focal length to achieve the steering mirror arrangement. In contrast, for a given lens focal length f, the steering lens arrangement leaves more space free between the last lens and the objective.

If an **acousto-optic deflector (AOD)** is desired to provide fast beam steering, it will be placed prior to the beam expansion. Again, we wish the AOD to be conjugate to the rear aperture of the objective. Equivalently, the AOD will be conjugate to the steering lens, by the transitive property of conjugate planes. The beam expansion consists of two lenses of focal lengths f_1 and f_2, where $f_2 > |f_1|$ and $\frac{f_2}{|f_1|}$ is the expansion factor. The system matrix between the AOD plane P_a and the steering lens plane P_s is

$$M_{sa} = M_t(s)M_l(f_2)M_t(f_2+f_1)M_l(f_1)M_t(d) = \begin{bmatrix} -\frac{f_2}{f_1} & f_1+f_2-s\frac{f_1}{f_2}-d\frac{f_2}{f_1} \\ 0 & -\frac{f_1}{f_2} \end{bmatrix},$$

where s is the distance from the second expansion lens to the steering lens and d is the distance from the AOD conjugate focal plane to the first expan-

sion lens, as shown in Fig. 2.12. Therefore, when the AOD is positioned with $d = -\frac{f_1^2}{f_2^2}s + \frac{f_1^2}{f_2} + f_1$, then it is conjugate to the steering lens, as desired. For example, if $f_1 = 50.2$ mm and $f_2 = 250$ mm for an expansion factor of 5x, then $d = 60.3\text{ mm} - 0.0403s$, whereas if $f_1 = 75.6$ mm and $f_2 = 200$ mm for an expansion factor of 2.6x, then $d = 104.2\text{ mm} - 0.143s$. This raises some practical considerations:

- While a beam expander might in general use a Keplerian approach with both lenses convex, $f_1 > 0$, or a Galilean approach with a concave lens, $f_1 < 0$, we find that the Galilean approach to beam expansion will not permit the placement of the AOD at a conjugate plane; it is necessary to have $f_1 > 0$. Alternatively, if an AOD is not steering the beam prior to beam expansion, then a Keplerian beam expander might still be preferred, because it provides a beam focus where a pinhole can spatially filter the trapping beam.

- A pinhole cannot be placed after a beam steering optic such as an AOD.

- The AOD creates a diffraction pattern. Usually only one of the diffracted beams is desired, so an iris (*i.e.* an adjustable aperture) can be used to block the extraneous beams. The iris must be sufficiently open that the desired beam can deflect, but if the iris is open too much then the extraneous beams will not be fully blocked. The AOD I used had a prism angle on the acousto-optic elements so that the deflected first order beam was collinear with the original laser beam for alignment convenience.

- Care must be taken to keep s sufficiently small that there is plenty of room to place the AOD.

- When I used an IntraAction dual-axis AOD, it was not possible to place both crystals at the appropriate conjugate focal plane, so I chose a placement where the conjugate plane was intermediate between the two crystals. If they were not mounted together, it would be possible to use additional lenses between the two crystals so that the x-axis AOD and the y-axis AOD were conjugate to each other and to the rear aperture of the objective.

- The calculation here assumes that the two lenses are placed a distance $f_2 + f_1$ apart. However, if the beam is not collimated prior to the expansion pair, then that separation distance should be adjusted so that the beam exiting the expansion pair is collimated.

- The tilting range of an AOD is small. The angular deflection will be converted to position control of the trap at the sample plane. In my setup, the AOD only provided a micron of travel for the laser beam at the sample plane, but choosing appropriate lens focal lengths could control this. You should consider how much travel you want to have at the sample plane. For example, a force clamp application might not need as much travel as a time-sharing application.

The AOD is an excellent tool for fast beam steering but it must be used thoughtfully.

Ultimately, we chose to move the piezoelectric stage to control the position of the sample with a fixed trap rather than using the steering optics, since only the relative position is important. Using a fixed trap ensures that the trapping power is constant as the relative position is adjusted laterally, which may not be the case when steering optics are used to move the trap position. Also, the position of the fixed trap can be marked on the camera

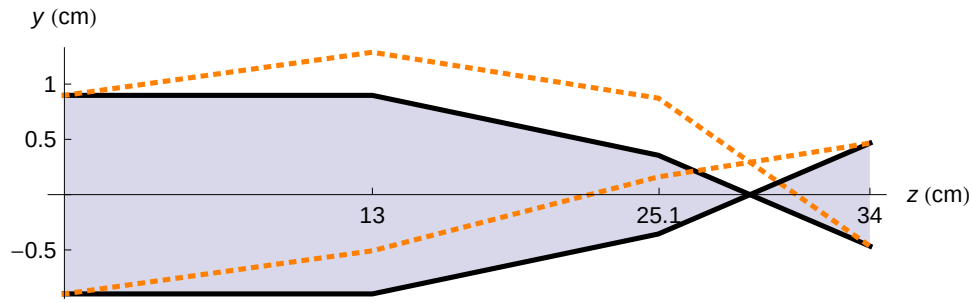

Figure 2.13: The IR collection path for position detection, as calculated with the ray-tracing matrices, Eq. (2.6). The diaphragm, dichroic, lenses, and PSD are not shown. The 200 mm lens is located 13 cm from the condenser aperture diaphragm at $z = 0$, or plane P_c, the 75.6 mm lens is located 25.1 cm from P_c, and the PSD is located 34 cm from P_c, as specified in Eq. (2.6). Here, z is the distance from the condenser aperture diaphragm, with the z-axis lying along the optic axis, and y is the radius of the beam. The shaded area between the black curves shows the IR the beam in the collection path under the following conditions: (1) there is no particle in the trap to cause interference and (2) the condenser is aligned for Köhler illumination such that the condenser aperture diaphragm is conjugate to the rear aperture of the objective. The orange dotted lines outline the location of the beam under the same conditions after it has been steered by the beam-steering optics. The beam arrives at the same location at the PSD regardless of how it is steered. A trapped particle, on the other hand, will create an interference pattern in the beam that will cause a change in the position signal read by the PSD.

display so that the position of the trap is always readily identifiable. Nevertheless, steering the trap has benefits for alignment and it may provide useful for future applications, especially with multiple trapping locations.

The **position sensing device** (**PSD**, at plane P_p) of the IR collection path should also be in the illuminating conjugate plane set [2]. This means the PSD is not placed at the focus of the trapping beam. To arrange this alignment, I placed optics with respect to the plane of the condenser aperture diaphragm (plane P_c) as described by the system matrix

$$M_{pc} = M_t(8.93\text{ cm})M_l(75.6\text{ mm})M_t(12.1\text{ cm})M_l(200\text{ mm})M_t(13\text{ cm}), \quad (2.6)$$

as shown in Fig. 2.13. The 13 cm translation includes the distance from the

condenser aperture diaphragm to the dichroic in the T-CHA plus the distance from the dichroic in the T-CHA to the 200 mm lens. One constraint in determining the appropriate optics was that I had already built a stage that provided space for the PSD to be located up to 14 inches from the condenser aperture diaphragm. I also chose to obtain a beam spot that would not overfill the PSD sensitive area so that the maximum optical signal would be measured. These two constraints made it impractical to achieve P_p at the appropriate conjugate plane with a single lens, so the solution above uses two lenses. As shown in Fig. 2.13, when P_p and P_c are conjugate, the beam will fall on the same location of the PSD regardless of how it is steered. Only interference from a trapped particle will change the position of the beam as measured by the PSD. There is also an imaging plane located at 28.9 cm from P_c.

2.2.3 Benefits and disadvantages of a commercial microscope

Almost every optical tweezers apparatus I have seen is built around a commercial inverted microscope. However, there are both advantages and disadvantages of using a commercial microscope compared to other choices of optomechanics and objective-holders.

We chose to build the optical trap using a commercial microscope. The advantages of the commercial microscope compared to a custom-built microscope are that the microscope is immediately usable, with DIC and phase contrast microscopy, excellent illumination, and built-in binoculars. We use a Nikon TE2000U inverted research microscope, which has excellent quality. In particular, its movable parts have excellent repeatability, which is a trait I have come to truly appreciate in any optomechanics parts. The dichroic

turrets provide the possibility of rotating a dichroic in and out conveniently, or comparing a dichroic to a beamsplitter. The port selector will likewise rotate reliably into place. The built-in focus knob provides the objective with both a large range of motion and submicron adjustment. Furthermore, the commercial microscope can be customized since it's built of modular parts. For example, the stacked pair of dichroic turrets are a rare customization to a TE2000U.

On the other hand, there are disadvantages of using a commercial microscope. The customizability of modular parts is limited to the parts available. One of the limitations of working with Nikon parts is that the dichroic turrets require very specific shapes of dichroics mounted in overpriced filter cubes. It is certainly an option to replace these turrets with custom optic mounts, which could be more stable, but such customization requires time and we would sacrifice the convenience of the rotation of the turrets. A benefit of customized dichroic mounts would be that we could gain access to the space at the back of the objective, which is currently nearly inaccessible. It is currently possible to fit only a thin optic at the back of the objective. When I was judging the effect of linearly polarizing the trapping beam, I purchased a thin polarizer and I machined its mount to be thin enough to fit between the objective and the dichroic turret, but there was not enough space to align the polarizer properly. The polarizer was just a one-time diagnostic tool, but the laser alignment process could also benefit from increased access to the back of the objective.

In places where we did need to machine parts fitting to the commercial microscope, it required careful measurements, since Nikon does not provide good drawings of the microscope. We needed to customize the stage to make a stable mount for the piezoelectric stage. (No commercial stage was avail-

able from Nikon that would interface directly to the piezoelectric stage.) If I were to start from the beginning, I would build the stage lower towards the optical table. In addition to making stability easier to achieve, a lower stage could be a safety benefit, since the existing stage height requires laser beams raised to eye level.

It is a disadvantage of the commercial microscope that the optics are inaccessible. For example, there is a lens inside the base of the microscope, but it is not visible and I cannot adjust its alignment. We deduced the presence of the lens because the sample plane is conjugate to a plane near the microscope port. It is not recommended to remove this lens because the binocular eyepiece likely uses that lens. Furthermore, an extra collimation pair may be helpful because the objective should output collimated light (it has infinity optics) but in practice, for this objective, infinity is about one foot.

Another customized part built into the microscope is the dichroic inside the T-CHA. The T-CHA is a cylindrical part that holds the condenser lens over the sample. It's also exactly in the location where I needed to put a dichroic to collect the forward-scattered trapping beam for particle tracking, so I built a dichroic mount to fit inside the T-CHA and I machined a hole in the side. There's a trade-off here, because the dichroic mount likely diminishes the quality of the illumination path, but it's worthwhile for the particle tracking abilities. If I were to remove the illumination path entirely, I could fit a larger dichroic and collect more of the forward scattered beam, which unfortunately clips on the dichroic in the T-CHA, but that trade-off is not advised because the illumination is useful. These trade-offs are only a matter of convenience; the best option, if time were available, would be to design a part that connects at the top and bottom as a T-CHA does but which is larger in the middle to provide space for a larger dichroic. Such a design could im-

prove both the illumination path and the trapping laser collection path compared to its current functional but compromised quality. The illumination path is also cantilevered and likely susceptible to vibrations, so it would be a great improvement to increase the stability of this dichroic to increase the accuracy of trap characterization, especially when using the power spectrum method (see Section 2.3).

Another issue that arose is that the rotating objective turret is not useful for optical trapping, though it is useful for changing the magnification while imaging. However, the piezoelectric stage leaves no room for rotating through multiple objectives, so the rotation becomes an inconvenience rather than a feature. A single-objective mount was once available from Nikon, but it has been discontinued.

To generally summarize the disadvantages of the commercial microscope, they all relate to the fact that the microscope can accommodate laser beams but it is not primarily designed for them. If I built a custom microscope, I would allow for space to place the last lens of the IR pathway nearer to the objective. This is achieved in other optical traps by replacing the dichroic turret with a custom dichroic mount attached to the commercial microscope. In our optical trap, I opted for a long focal length lens that could be placed further from the objective.

Ultimately, these are all viable options that represent the range of choices when building an optical trap. There are trade-offs to each decision, and my goal has never been to build the best optical trap, but rather to build a trap that functions as well as it needs to function for our purposes while understanding what benefits could be made when there is need.

2.2.4 Challenges and solutions

I ran into a number of challenges in achieving a stable optical trap. The discussion here is intended to assist future researchers working with an optical tweezers apparatus.

The **alignment of the laser entering the objective** is crucial to achieving a stable optical trap. The beam should enter the objective both centered in the objective and parallel to the objective axis. It does not have to be perfect; in fact, the beam is steered by adjusting the angular deflection of the beam. However, a misaligned beam will create an unstable trap, so in practice, the alignment of the beam has to be quite good. I used the two aiming mirrors on two-axis gimbal mounts to align the beam into the objective.

For centering the beam, I used a custom machined cylindrical alignment tool. The cylinder has external threading matched to the threading of a Nikon objective so it screws into the objective location. The cylinder has a 6-mm diameter hole through the center, corresponding to the diameter of the rear aperture of the objective. By maximizing the optical power through the hole,[2] the beam is centered at the objective location.

I used three approaches to aligning a beam parallel to the objective axis.

1. Maximize the beam power through a long, externally threaded cylindrical alignment tool at the objective location, such that the beam will be parallel to the objective axis as well as centered at the objective rear aperture.

2. Observe the beam focus with the camera and adjust the optics so that the beam appears as symmetric as possible.

[2] Make sure the laser power is stable whenever using the maximization of beam power for alignment.

3. Place a mirror above the objective location. If it is aligned perpendicular to the objective axis (I relied on the assumption that the piezoelectric stage sitting on the machined stage was sufficiently perpendicular), then the beam will be reflected back through the optical path. When the back reflection follows the incoming beam path, the incoming beam is parallel to the objective axis. Centering the beam must be achieved independently (using the first approach in this list), which means that the beam must be centered and made parallel in an iterative process.

In practice, only the third approach to achieving a parallel beam, not the first or second, was successful for creating a stable trap. Other methods that can be useful include the following:

4. Color the top of a coverslip black. It will burn a little so that it is visible if the spot is focused and if the spot is walking when the focus is adjusted.

5. Trap particles, then lower the laser power until they just escape the trap, then make small adjustments to the optics until the particles trap again.

The alignment of the laser is critical for optical tweezers.

The beam should ideally have a **Gaussian profile**. The laser amplifier outputs a TEM_{00} mode from the single-mode fiber, so the beam is expected to have a Gaussian profile. However, problems with the optics components can mar the beam profile. I do not recommend "protected" silver mirrors; I found that they tarnish with time.[3] A better choice is dielectric mirrors,

[3]This was not visibly clear until I actually aimed a flashlight at the mirrors and then it became all too obvious. It can also be diagnosed by checking the beam power before and after the mirror and comparing to the reflectivity specifications.

though these may have disadvantages for applications that require polarization preservation. The pinhole in the beam path is also intended to improve the spatial profile of the beam.

I purchased the **infrared dichroic** from Chroma. When I spoke to them about it a few years after the purchase, they were concerned that the dichroic was thin and mounted with plastic, and therefore not sufficiently stable for optical trapping. For demonstration, they let me use a laser-grade mounted dichroic (T860SPXRXT-1500 and 91032) that was supposed to be better but when I compared the two, the trapping stiffness was not improved, so I did not purchase the demo.

Immersion oil is quite useful because it permits a high NA to enable optical trapping. However, **air bubbles in the immersion oil** are a concern. Bubbles act as extra lenses that completely ruin the optics path. A water immersion objective can also have bubbles. To avoid bubbles, the following points are important. We do not focus the powerful trapping laser beam into the oil, because it burns the oil or attracts a bubble into the trap. We focus the trapping laser on the far side of the coverslip, away from the oil. In addition, we put the immersion oil under vacuum once to remove excess air in the oil.

2.3 Characterization

A variety of techniques are valuable for characterizing a trap, including camera observation, escape velocity observation, single-particle tracking with the forward-scattered beam, measurements of the bead trajectory via such single-particle tracking, and trap stiffness measurements that may be made using the bead trajectory measurements.

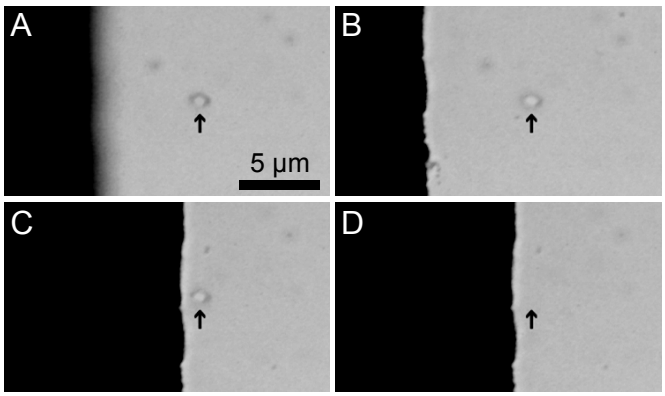

Figure 2.14: Spatial control of optically trapped nanodiamonds near the (black) microwave antenna. (*A*-*B*) The antenna is brought into focus, moving axially by 4.2 µm with respect to the trapped nanodiamonds from (*A*) to (*B*). An arrow indicates the position of the optical trap, with nanodiamonds visible in both frames. (*C*) The antenna is moved laterally by 8.75 µm while the nanodiamonds remain trapped. (*D*) The trapping laser is blocked, releasing the nanodiamonds and allowing Brownian motion to scatter them away from the focus. Reprinted from Ref. [1], where this figure is also available as a movie.

Camera observation

The first method of judging the trap is via camera observation. Potential trapping problems will be visible in the camera image, including repulsion, orbiting, and melting. If the trapping beam displays a repulsive force, hopefully it is only because the focus of the laser is in the coverslip. In this case, moving the stage and the objective closer (by, for example, lowering the stage towards an inverted objective) will bring the trapping location into the colloidal solution and as the gradient force overpowers the scattering force, trapping will become possible. However, if this does not improve the trap, then the optical path probably needs work.

Another problem visible in the camera is large motion of the trapped bead. In particular, if a trapped bead appears to be following an orbiting motion, this is indicative of an unstable trap and the optical path needs

work.

Diamond nanoparticles do not melt, but polystyrene does melt, and if the polystyrene is trapped in a glycerol medium, melting is quite common. Laser heating is less of an issue in water. When the trapped particles melt, it is helpful to change the material or the medium, or to decrease the laser power.

Escape velocity

Once the trap appears reasonably stable in the camera, a more quantitative method of judging the trap is by dragging a trapped particle through the liquid medium [49]. At what speeds can the trapped bead be dragged through the medium? I usually use the piezostage to control the acceleration and speed of the liquid while holding the trapping location fixed with respect to the lab, but a microfluidic channel can also be used to push liquid past a trapped bead. The piezostage is preferred, however, because it can report back the escape speed. Piezostage motion patterns are also possible for determining trap stiffness using the drag force method [2].

For example, a polystyrene microsphere in water remained in the trap when I moved the piezostage and water chamber at up to 0.82 μm/ms, even when moved a distance of 100 μm at that speed, but the bead escaped the trap when it was moved at a speed of 0.88 μm/ms.

Single-particle tracking with the forward-scattered beam

Trap stiffness is generally measured by tracking a single particle using a forward-scattered laser beam. I have used the infrared trapping laser for tracking, but a separate tracking beam is also an option, and the 532 nm laser might be of use for single-particle tracking, since collecting the forward-scattered beam would not interfere with its ability to excite

fluorescence. If a weaker beam is used, a good filter might be necessary to fully remove the trapping beam from the particle-tracking collection path. Since I used the infrared trapping laser for tracking in the back focal plane, the particle position was always measured relative to the center of the infrared laser beam.

The position of the bead with respect to the beam will affect the interference pattern visible in the forward-scattered beam. (That is, it's visible if you hold an IR card in the forward-scattered beam.) This interference pattern is detected as a beam deflection with a quadrant photodiode (QPD) or a position sensing device (PSD). The deflection of the beam is related to the bead position according to [71] (see also Refs. [72, 73])

$$\frac{I_x}{I} = \frac{16k\alpha}{\sqrt{\pi}w_0^2}\left(\frac{x}{w_0}\right)\exp\left[-\left(\frac{x}{w_0}\right)^2\right], \tag{2.7}$$

where

I_x/I	is the normalized x signal of the forward-scattered beam, proportional to the beam deflection in x,
k	is the wavenumber,
α	is the bead polarizability,
w_0	is the beam waist radius in the focal plane, and
(x, y, z)	is the bead position.

Calibration is necessary to find the relation between the beam deflection and the bead position (Fig. 2.15). For calibration, a bead that is adsorbed onto the coverslip is positioned in the trapping beam using the piezostage. With this calibration, the position of a trapped bead with respect to the laser focus is then determined from the calibrated relation between the beam deflection (i.e. the position of the centroid of the forward-scattered beam interference

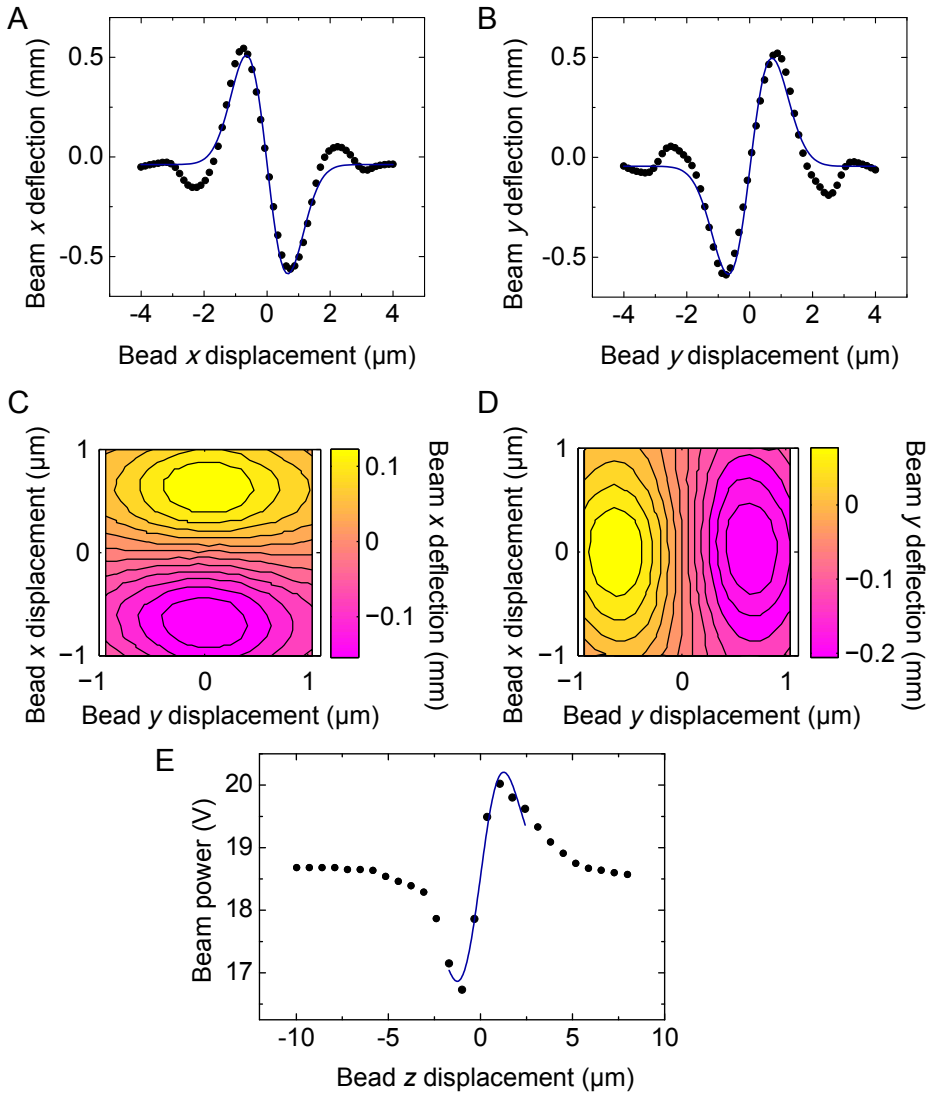

Figure 2.15: Bead position calibration. Lateral displacement of a bead through the trapping beam causes an interference pattern in the beam that is detected by the PSD. For calibration, the bead position is controlled by piezostage while the bead is adsorbed to a coverslip. (*A*-*B*) The deflection curve data (black circles) are fit (blue curve) to Eq. (2.7). The linear calibration coefficients are found to be $\rho_x = -1.37$ mm/μm and $\rho_y = 1.28$ mm/μm for this bead. (*C*-*D*) A two-axis calibration. (*E*) Axial calibration (black circles) with fit (blue curve) to Eq (2.7). The y-axis is the power of the forward-scattered beam as measured by the PSD in volts, and the axial linear calibration coefficient is found to be $\rho_z = 2.36$ V/μm.

pattern) and the bead position. When creating a calibration dataset, it is important to make sure that the bead remains well-stuck to the coverslip, so the trapping beam must be lowered to a power where it will not push the bead off the coverslip. If the bead shifts while a calibration scan is in process, the dataset will show a jump and the calibration must be redone.

The axial position of the bead can also be determined by measuring the intensity of the forward-scattered beam [71, 74]:

$$\begin{aligned} \frac{I_z}{I} &= \frac{8k\alpha}{\pi w_0^2}\left(1+\left(\frac{z}{z_R}\right)^2\right)^{-1/2} \sin\left(\arctan\frac{z}{z_R}\right) \\ &= \frac{8k\alpha}{\pi w_0^2}\frac{z/z_R}{\left(1+(z/z_R)^2\right)}, \end{aligned} \tag{2.8}$$

where I_z/I is the normalized intensity of the forward-scattered beam and z_R is the Rayleigh range. Beware that Neuman and Block have a typographical error in Eq. (5) in Ref. [2]. An axial calibration is shown in Fig. 2.15*E*. (For these data, I found that Eq. (2.8) was not a good fit for purposes of calibration, so I used the functional form of Eq. (2.7) instead.)

Much of particle tracking relies on the idea that a trapped bead does not move very large distances. Therefore the bead stays in the central region where Eqs. (2.7) and (2.8) are approximately linear, deflection = $\rho_x x$, where x is the bead displacement in µm and the calibration coefficient ρ_x is in mm/µm. The calibration will vary with particle size, shape, and material. This method using a QPD or PSD is not suited for tracking multiple particles, but camera images of digital holograms can facilitate multiple-particle tracking [75].

It is often more convenient to use the uncalibrated deflection signal, relying on the linearity of the calibration, rather than using the calibration to calculate the true position of the particle. Even if the uncalibrated signal is

used, it is important to perform a calibration of the QPD or PSD in order to catch problems with the signal and to make sure that the bead is in the linear region of the calibration.

One problem that can arise is that the power of the laser impinging on the PSD must be in a certain range for good measurements. If the power is too low, the PSD measurement has a systematic error and a high standard deviation. I found that the minimum voltage for good PSD measurements is 3.7 V. If the incident beam power is too high, the measurement voltages will reach their maximum (10 V) for measurement with the data acquisition device.[4] The filter wheel in the particle tracking optical path is valuable for adjusting the power to the appropriate range.

Another approach is to use a beamsplitter to separate the beam into two parts. The first beam goes to a PSD/QPD for lateral tracking and the second beam goes to a photodiode for axial tracking. The axial signal benefits from a lower condenser NA [76, 77].

Bead trajectory via back focal plane detection

A well-trapped bead does not have a very interesting trajectory pattern: the bead should just stay put in the center. The trapped particle trajectory can reveal problems with the trap. For example, Fig. 2.16*A*-*C* shows the trajectory pattern of a bead that is poorly trapped while Fig. 2.16*D* shows the trajectory of a bead that is well trapped.

Trap stiffness using the power spectrum of the trajectory

A common approach to trap characterization is the measurement of trap stiffness. Since the trap is like a three-dimensional harmonic potential well,

[4] In Fig. 2.15*E*, two voltages are added together such that the maximum voltage is 20 V.

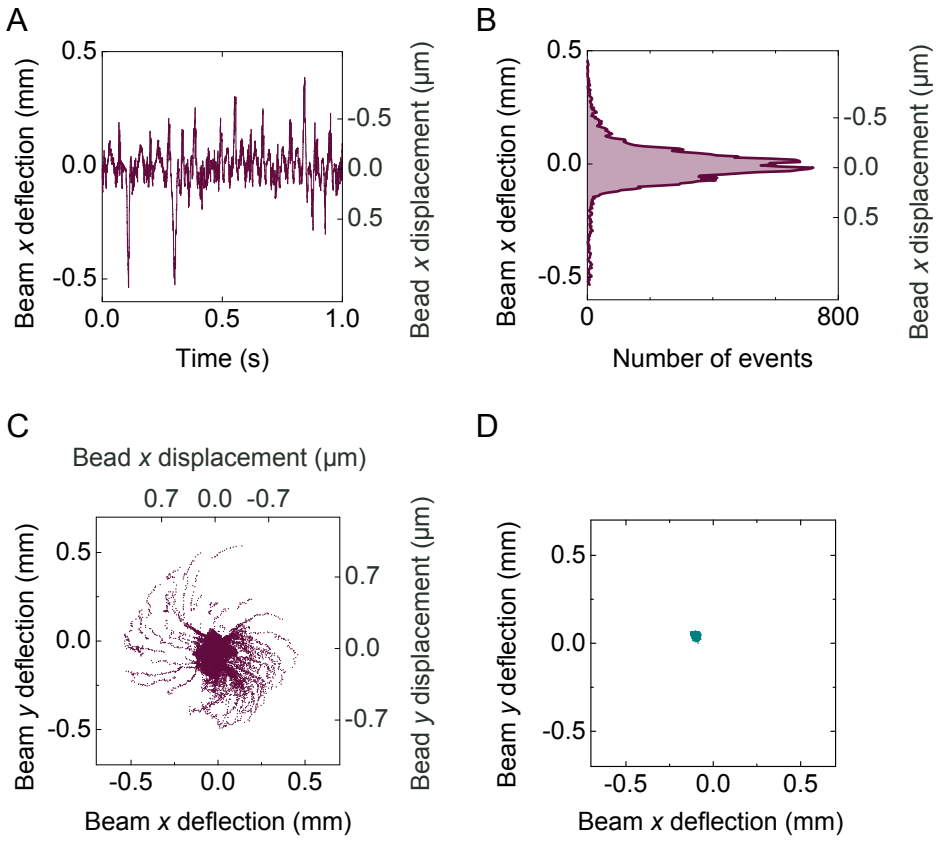

Figure 2.16: Problems with the trap can be identified using the trapped bead trajectory. (*A*) A problematic bead trajectory, showing a bead moving large distances from the trap center. The beam deflection is measured with the PSD and the bead displacement is inferred from a calibration using a similar bead stuck to the coverslip. (*B*) A histogram of the trajectory shown in (*A*). (*C*) The same trajectory, here viewed in two spatial dimensions. We see that, much of the time, the bead is near the center of the trap, but it also explores space further from the center of the trap, usually with a motion that slowly brings the bead away and then rapidly returns to the center, while the bead moved predominantly clockwise around the trap center. The large motion of this bead was also visible with the camera. (*D*) A second trajectory, in which the bead is well centered in the trap.

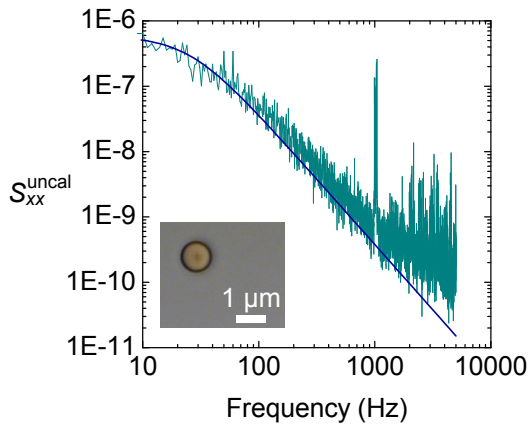

Figure 2.17: The power spectrum (green curve) of the trajectory of an optically trapped bead with fit (blue curve) to Eq. (2.9). The corner frequency is $f_{0,x} = 25.5 \pm 0.3$ Hz, which corresponds to a trap stiffness of $k_x = 1.5$ pN/µm. The inset micrograph shows the polystyrene sphere while it is trapped in the water.

it has a set of spring constants, k_x, k_y, and k_z. There are a variety of methods for determining the trap stiffness [2]; to calculate trap stiffness, I generally used the power spectrum of the trapped particle trajectory, measured using back focal plane detection. This approach is based on the thermal motion of a trapped bead.

If $S_{xx}(f)$ is the one-sided power spectrum of the Brownian motion along the x-axis in a harmonic potential well, then it has the form [2]

$$S_{xx}(f) = \frac{k_B T}{\pi^2 \gamma \left(f_{0,x}^2 + f^2 \right)}, \tag{2.9}$$

where k_B is the Boltzmann constant, T is the absolute temperature, γ is the hydrodynamic drag coefficient of the bead, $f_{0,x}$ is the corner frequency, and f is the frequency.

Unlike some other methods, such as the drag force method, this approach does not require the use of piezostage motion. Since it relies on the bead trajectory measurement, it cannot be used when there are multiple particles in

the trap. In addition, this method assumes the trapped particle is spherical, so it is useful for determining the trap stiffness for a trapped microsphere, but it may not be as useful for nanodiamonds. (However, the presence of nanoparticles can be detected with a similar technique; see Ref. [78].) This method can use the uncalibrated PSD data, but as I wrote above, I nevertheless recommend checking the calibration to ensure the deflection of the laser is linear to the position of the trapped bead. Using the uncalibrated PSD data, we obtain the one-sided power spectrum $S_{xx}^{\text{uncal}}(f) = \rho_x^2 S_{xx}(f)$. Fitting the measured power spectrum to Eq. (2.9), we obtain the corner frequency, $f_{0,x}$, as a fitting parameter, as shown in Fig. 2.17. The spring constant is then [2]

$$k_x = 2\pi\gamma f_{0,x},$$

with the lateral hydrodynamic drag γ given by Faxén's law [2, 43],

$$\text{lateral} \quad \gamma = \frac{6\pi\eta a}{1 - \frac{9}{16}\left(\frac{a}{h}\right) + \frac{1}{8}\left(\frac{a}{h}\right)^3 - \frac{45}{256}\left(\frac{a}{h}\right)^4 - \frac{1}{16}\left(\frac{a}{h}\right)^5},$$

where η is the viscosity of the liquid medium, a is the trapped bead radius, and h is the distance above the surface. For example, if the medium is water with a viscosity of $\eta = 0.001$ kg/(m s), the bead has diameter $2a = 1$ µm, and the bead is trapped at $h = 3$ µm above the coverslip, then $\gamma = 0.01$ pN ms/nm. Faxén's law is preferred to the more approximate Stoke's law because we usually trap very close to the coverslip to minimize beam aberration. In the example, Stoke's law would have an error of 9%. For axial hydrodynamic drag, see Ref. [2, Eq. 9].

Other trap stiffness methods

In addition to the approach outlined here, there are many techniques for calculating the trap stiffness. If the sample information, such as bead size a,

medium viscosity η, and height h are unknown, Ref. [79] describes a method to measure all required quantities to find the trap stiffness. The use of the equipartition theorem, an approach based on optical potential analysis, the drag force method, and direct measurement of optical force are discussed in Ref. [2]. The step response method and other methods of stiffness measurement are described in Refs. [80, 81]. Characterizing the trap using Allan variance is discussed in Ref. [82].

Characterizing a trap using fluorescence

Ultimately, the most important way to characterize a trap is based on how it will be used. This trap will be used for trapping fluorescent nanodiamonds, so this provides for us the possibility of judging the trap quality based on fluorescence. If the noise in the fluorescence intensity of the trapped nanodiamonds is small, it is ideal for clean measurements. This will be discussed more in Section 4.2.

♦♦♦

Chapter 3

Nanodiamond fluorescence

The fluorescence of NV centers provides a wealth of information. The zero phonon line (ZPL) wavelength of the fluorescence shows the splitting between the excited and ground state (Fig. 3.1), and the electronic spin state can be inferred from the intensity of the fluorescence signal. In order to measure the fluorescence, we built a confocal fluorescence microscope.

All data shown in this chapter were taken using milled monocrystalline nanodiamonds from Microdiamant. These nanodiamonds are not irradi-

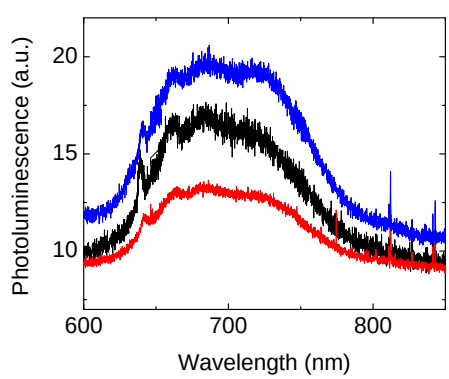

Figure 3.1: The photoluminescence spectra of three different fluorescent nanodiamonds. The zero phonon line (ZPL) at 637 nm indicates the presence of negatively charged NV centers. There is a broad phonon sideband with a peak near 700 nm.

ated, and in general they have fewer than one NV center per ~50 nm particle.

3.1 Instrument

The optical apparatus is shown in Fig. 3.2. The nanoparticle diamond NV color centers are excited with a continuous wave 100 mW, 532 nm laser focused through a 100× oil-immersion objective. A holographic notch filter in the laser beam path filters out all extraneous wavelengths. A half wave plate rotates the polarization of the laser prior to the holographic notch filter to match the polarization expected by the notch filter. The sample is mounted on a three-axis piezoelectric stage so that the nanoparticles can be scanned through the laser spot. The fluorescence signal is collected in a reflection geometry. Table 3.1 lists the optical elements in the excitation path and Table 3.2 lists the optical elements in the fluorescence collection path. Items 11 and 12 are filters that were only used when the 1064 nm trapping laser was used, so they are not shown in Fig. 3.2; their placement will be shown in Fig. 5.1.

In some cases (specifically, when using a higher wattage excitation laser), it has been necessary to add a pinhole in the collection path to spatially filter the emission signal but this is generally unnecessary. With the 100 mW 532 nm laser, adding a pinhole makes no difference to the measurement, so I don't use it, relying only on the optical fibers attached to the APDs and in the spectrometer collection path to spatially filter the signal. Placing a pinhole in the collection path prior to the camera has the disadvantage that the camera can no longer be used for wide-field imaging.

In order to perform multiple measurements simultaneously, I split the

Table 3.1: Elements of the optical excitation path

#	Item	Brand	Item number
1	Excitation laser	CrystaLaser	GCL-532-100-L CW DPSS,
	TEM_{00}, Noise < 0.5%, >100:1 polarization, power stable 1% over 24 h		
2	Filter wheel	Newport	FS-3R and FWM1X6
3	Lens, $f = 250$ mm	Newport	KPX109AR.14 and TSX-1D
4	Mirror	Newport	10D20BD.1
5	Half wave plate, mica	OptoSigma	068-2350
6	Holographic notch filter	Kaiser Optical Systems	HLBF-532.0
7–8	Lens pair	Newport	KPX096AR.14 (qty:2) and TSX-1D stage
9	Iris	Newport	ID-0.5 and MH-2P
10	Mirror	Newport	10D20BD.1
11	Beam sampler	Newport?	10B20NC.1?
12	Iris	Iris	ID-0.5 and MH-2P
13	Mirror	Newport	10D20BD.1
14	Lens, $f = -25$ mm	Newport	KPC025AR.14
15	Linear polarizer	Newport	10GT04AR.14 and RSP-1T
16	Lens, $f = 400$ mm	Newport	KPX115AR.14 and TSX-1D
17	Iris	Newport	ID-1.0
18–19	Mirror pair in periscope / beam steerer	Newport	10D20BD.1 (qty:2) and BSD-2A
20	Last mirror	Newport	10D20BD.1 and TSX-1D
21	Excitation dichroic mirror	Chroma	z532rdc
22	Transmission through IR dichroic (optional)		
23	Objective, CFI Plan Fluor 100x 1.3NA	Nikon	MRH01901

Table 3.2: Elements of the fluorescence collection path

#	Item	Brand	Item number
1	Objective, same	Nikon	MRH01901
2–3	Transmission through IR dichroic (optional) and excitation dichroic		
4	Lens in microscope base	Nikon	part of TE2000U
5	Mirror in microscope base	Nikon	part of TE2000U
6	Lens, $f = 100$ mm	Newport	PAC052AR.14 and TSX-1D
7	Beamsplitter cube, 50:50	Newport	10BC17MB.1
7.1	Filter, notch block 532 nm	CVI Melles Griot	RNF-532.0
7.2	Lens, $f = 50.8$ mm	Newport	PAC040
7.3	Optical fiber, multimode	Thorlabs	BFL37-400, 24 m
7.4	Lenses, ~1.5 in and ~3.5 in	Newport?	
7.5	Spectrometer	Princeton Instruments/Acton	SpectraPro 2758: ARC-SP-2758
7.6	Spectrometer grating, 300 G/mm	Princeton Instruments/Acton	ARC-750-1-030-500
7.7	CCD camera, liquid nitrogen cooled	Princeton Instruments/Acton	Spec-10:400BR/LN
8	Pellicle beamsplitter, 8:92 (R:T)	Thorlabs	BP108
8.1	Lens, $f = 88.9$ mm	Newport	PAC049
8.2	Camera, color CMOS	Uniforce / PixeLink	PL-B681CF-KIT
9	Filter, 640 nm long pass	Omega Optical	3RD640LP
10	Beamsplitter cube, 50:50	Newport	10BC17MB.1
11	Filter, blocks 1064 nm and 532 nm	Omega Optical	XB11.25R
12	Filter, notch block 1064 nm	Edmund	NT46-567
13	Lens, $f = 63.5$ mm	Newport	PAC043AR.14 (qty:2)
14	Optical fiber, multimode	Pacer International (OZ Optics)	SPCM-Q9 (MMJ-33-IRVIS-50/125-3A-2) (qty:2)
15	Avalanche photodiode (APD)	Pacer / Perkin Elmer, now Excelitas Canada	SPCM-AQRH-13-FC (qty:2)

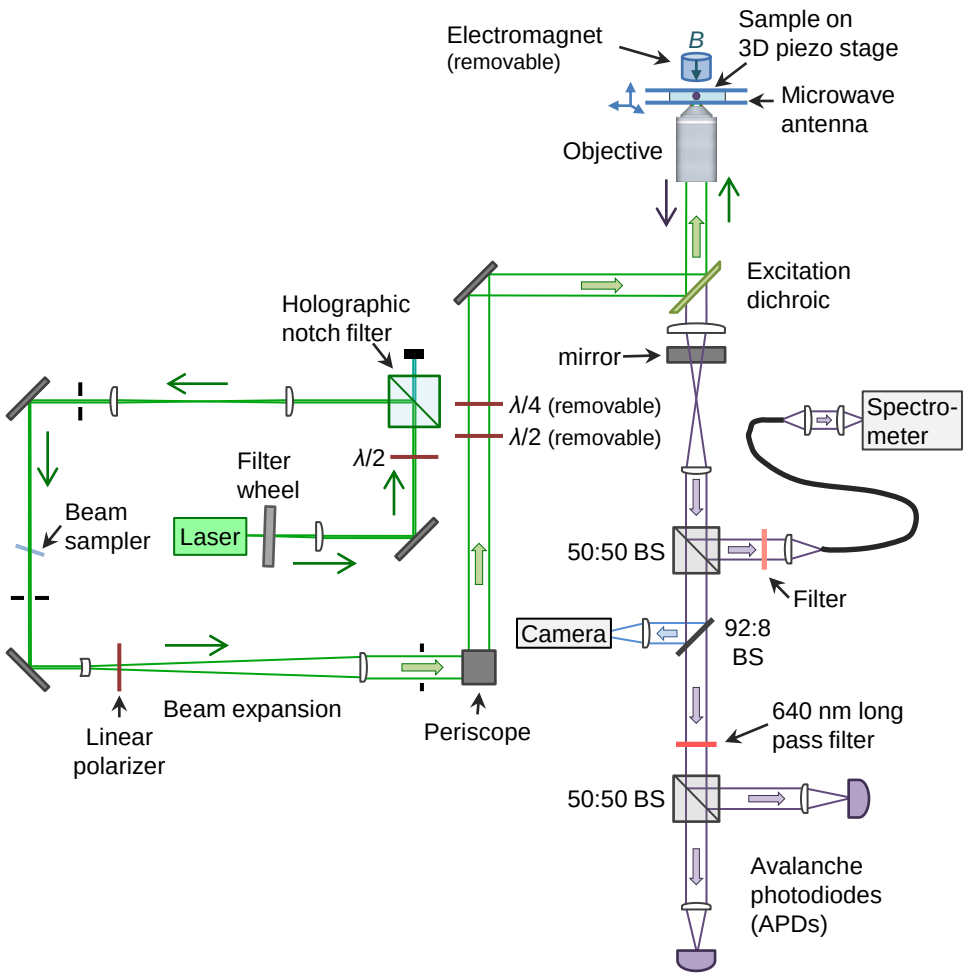

Figure 3.2: The 532 nm excitation beam pathway and the fluorescence collection pathway.

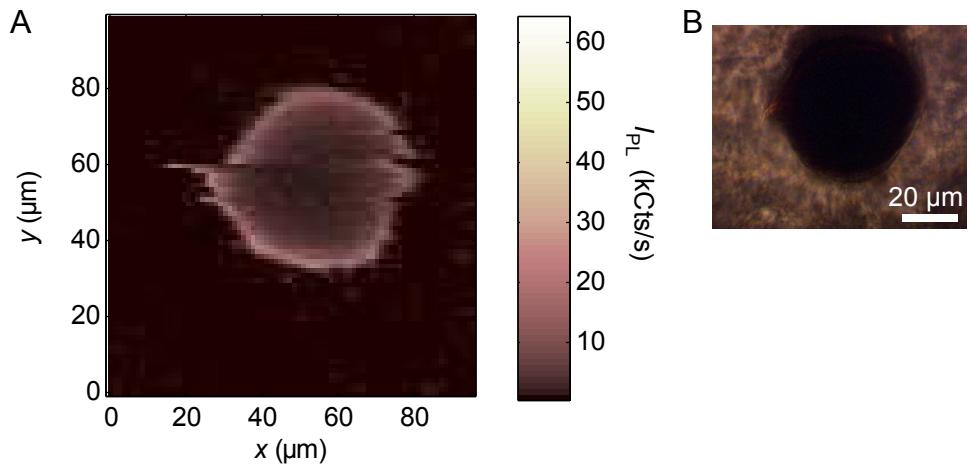

Figure 3.3: A squid chromatophore. (*A*) The micro-photoluminescence of a *Loligo opalescens* squid chromatophore measured while scanning the piezostage. The lines are scanned in x, and the chromatophore was so fresh it was still moving, so the rastered line scans show some staggering, especially at $y = 60$ μm. (*B*) A micrograph of the same chromatophore.

fluorescence light signal as follows:

Percent of signal	Instrument
50%	spectrometer
4%	camera (color CMOS PixeLINK or black and white CCD)
23%	APD 1
23%	APD 2,

as shown in the collection path of Fig. 3.2.

The spectrometer measures the emission spectrum as a function of wavelength. The light signal is delivered to the spectrometer with a multimode optical fiber. Each avalanche photodiode counts photons. I use a filter to control the spectrum of photons I measure with the APD. The pair of APDs makes it possible to measure antibunching.

In addition to using this apparatus to measure diamond NV centers, we have measured the fluorescence of *Loligo opalescens* squid chromatophores [83, 84], as shown in Fig. 3.3.

3.2 Nanoparticle deposition

In order to characterize nanoparticles, it is useful to immobilize them by having them adsorbed onto a surface. There are multiple ways to deposit nanoparticles onto a surface. The simplest is to drop-cast nanoparticles, and in many cases drop-casting is appropriate. However, drop-casting has some disadvantages. It tends to leave a coffee ring at the edges and particles may aggregate while the solvent is drying. Electrospray ionization, on the other hand, allows us to spray nanoparticles in a solvent onto a surface. The solvent evaporates quickly, and the charged particles stream toward the grounded substrate. Spin casting is another method of nanoparticle deposition.

3.2.1 Drop-casting

For drop-casting, I generally choose an appropriate dilution of the nanoparticles, usually diluted in water. In many cases I do not dilute the nanoparticle solution at all, just using the as-purchased dilution. I pipet a small amount, often 2 μL of solution, onto the surface. To dry the solvent, I may heat the sample on a hot plate or use a nitrogen gun (careful to blow gently and straight down onto the sample[1]) or I may let the solvent dry slowly at room temperature. The pipetting and drying step may be repeated. I usually inspect the deposition using a microscope immediately after the deposition, often with dark field illumination.

3.2.2 Electrospray

Electrospraying offers improved regularity of the deposition, and the concentration can be tuned more carefully than with drop-costing. One important

[1] and careful not to blow any other samples away!

goal of using the electrospray process was to eliminated aggregation in deposited nanodiamonds.

I used an electrospray apparatus for deposition of the nanoparticle diamonds. The nanoparticle diamonds are first diluted to a concentration of 0.5 mg/mL in methanol. Then the solution is placed in a syringe over a glass coverslip and the tip of the syringe is brought to 7 kilovolts while the syringe is automatically dispensed at a rate of 0.2 mL/hour in order to deliver a steady supply of nanodiamonds in solution to the tip. The idea is that the voltage charges the nanodiamonds so that they repel each other, and the solution splits into small droplets (the Coulomb explosion) while the methanol is evaporating en route to the glass coverslip so that the nanodiamonds land on the glass coverslip without aggregating [85, Fig. 2]. I usually run this for about an hour. Longer times give more dense nanoparticle spacing and shorter times give less dense spacing. Thus I obtain a glass coverslip covered fairly uniformly with diamond nanoparticles of a convenient spacing, as shown in Fig. 3.4.

Why methanol? We tried pure water as the solvent, but the water does not evaporate while it is sprayed and so droplets of water form on the coverslip, and the nanoparticles aggregate while the water is drying. Similarly, with 10% methanol in water and with 20% methanol in water (by volume), droplets of liquid form on the coverslip. This is the mixed droplet/ion emission regime [86]. I observed that ethanol and acetone, on the other hand, are successful for obtaining pure ion emission, but AFM images revealed that the nanoparticles were still aggregated. In fact, zetasizer measurements show that the nanodiamonds aggregate in solution in ethanol (Fig. 3.5) and acetone. Pure water is the best solvent for obtaining un-aggregated nanodiamonds, but water is not an appropriate solvent for electrospraying because

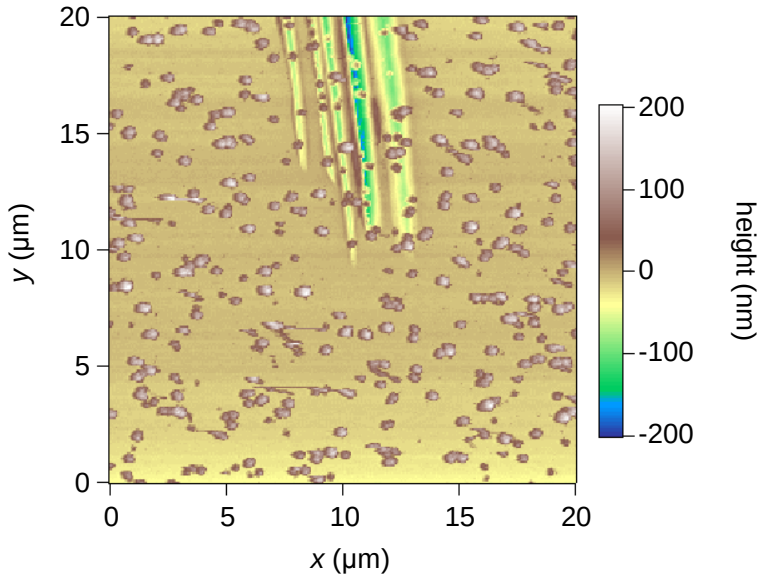

Figure 3.4: An atomic force microscopy image of electrosprayed nanodiamonds. The glass coverslip substrate is intentionally scratched to facilitate consistent placement of the sample.

it is in the droplet regime. Pure methanol is nearly as good as water in terms of aggregation, and it is a solvent that sprays in the ion regime. Therefore, for electrospraying nanoparticles, we use pure methanol as the solvent, or, more accurately, 97.5% methanol in water (by volume), because the nanodiamond sample is in solution in water when purchased and we simply dilute it with pure methanol for electrospraying.

The electrospray is useful for creating a random spread of particles on the surface. However, the electric field lines can be influenced by irregularities in the shape of the grounded surface or in the shape of the high-voltage surface. For example, the alligator clip attached to the syringe tip is at high voltage and it will tend to repel particles such that they are deposited more heavily on the side of the grounded surface that is opposite of the alligator clip. In addition, I have observed that when I electrospray nanodiamonds onto a coverslip that

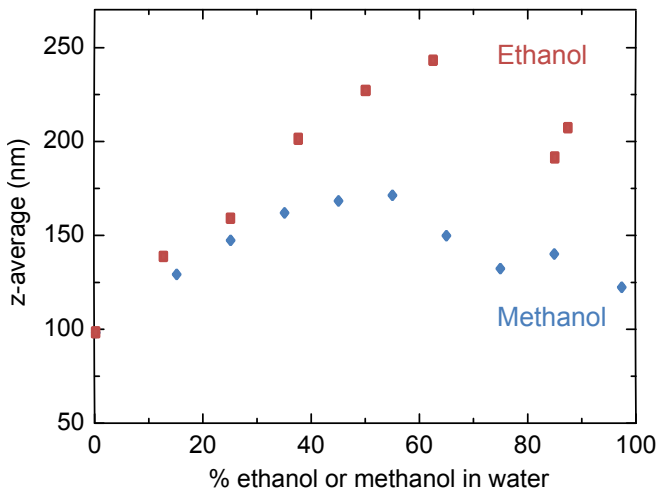

Figure 3.5: Aggregation of MSY100 nanodiamonds in solution in water, ethanol, and methanol, measured with a Malvern Nano ZS. The z-average gives the size of the nanodiamond clusters in solution in mixtures of ethanol and water (red squares) or methanol and water (blue diamonds). Data courtesy of Jayna B. Jones.

has a microwave antenna patterned on the surface, the nanodiamonds land on the coverslip with higher concentration near the metal pattern and lower concentration further from the metal pattern.

In order to measure the photoluminescence of single color centers, it is necessary to prepare a sample in which the nitrogen-vacancy centers are separated further than the measurement resolution. The laser spot size gives a lateral resolution of about 0.3 microns (Fig. 3.6), so this sets the minimum desired distance between NV centers.

3.3 Antibunching measurements

Each NV color center is a single-photon emitter. To test this, I perform time-correlation measurements using a Becker and Hickl card collecting the electronic signal from each APD. The two APDs are placed in a Hanbury Brown

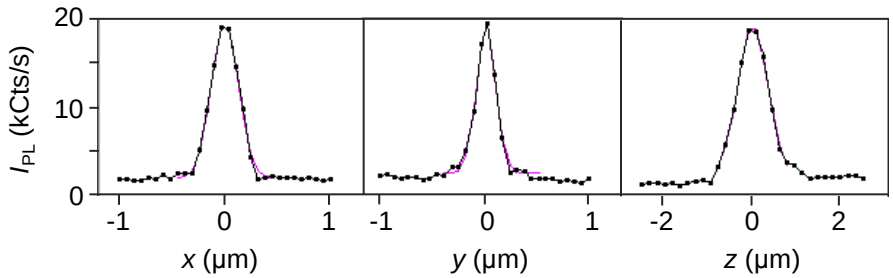

Figure 3.6: Single NV fluorescence. These three line scans (black squares), in x, y, and z, show the general shape of the fluorescence signal of a single NV center. The FWHM of these scans is 0.30 μm, 0.22 μm, and 0.80 μm, respectively, as determined by Gaussian fits (purple curves). The antibunching curve for this single NV is shown in Fig. 3.7. See also Fig. 2.5*B* for a two-dimensional fluorescence scan of another single NV center.

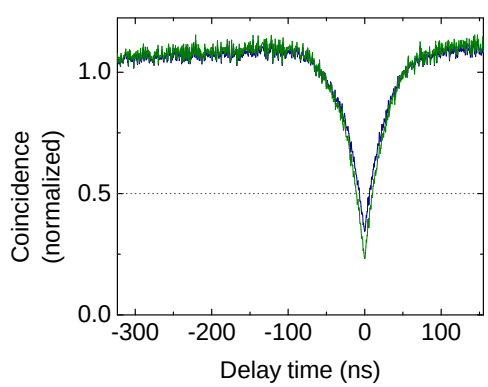

Figure 3.7: The time-correlation measurement of a single NV center displays antibunching. This is a histogram showing the delay time between two photons on the x-axis and the probability of such a two-photon event on the y-axis. The blue data show the normalized probability of coincident events. The green data show the result of subtracting the background according to Eq. (3.1), where S = 19.45 kCts/s and the dark count rate of the APD is B = 1.6 kCts/s. The data dip below 0.5 at zero delay time, indicating that this is a single photon emitter.

and Twiss arrangement, as shown in Fig. 3.2. A photon entering APD 1 will start the clock, and a photon entering APD 2 will stop the clock, and a count is recorded for that clock time [87]. Hence every count in an antibunching measurement corresponds to two photon counts: the first from APD 1 and the second from APD 2. The result is shown in Fig. 3.7 (see also Figs. 3.8*C* and 3.9*C*), which shows the probability that two NV emission photons have a particular delay time. This is the second-order time correlation function $g^{(2)}(\tau)$ of the photon emission. Since only one photon is emitted from the NV at a time, only one APD is expected to count a photon at a given instant. Therefore the time correlation plot shows an antibunching dip at the time delay corresponding to simultaneous counts. If the antibunching dip falls lower than 0.5, we can be reasonably assured that the optical measurement collects fluorescence from only one NV center, not from multiple NV centers.

At higher laser excitation powers, there is also a bunching effect [88] indicating that two photons are more likely to be emitted with a particular time delay, as if they were being emitted one after the other in rapid succession.

The APDs can not measure zero counts. They have a dark count rate that I measure by screwing a cap over the end of the optical fiber, thereby blocking all light. This count rate adds a constant background to the time correlation measurements, and this constant background can be subtracted according to the equation [89]:

$$g^{(2)}(\tau) = (C_N(\tau) - 1 + \rho^2)/\rho^2, \quad \text{where} \tag{3.1}$$

$$\rho = S/(S+B),$$

τ is the delay time between photon counts, $C_N(\tau)$ is the normalized coincident count signal, S is the I_{PL} signal, and B is the background I_{PL}.

3.4 Blinking nanodiamond NV centers

In general, all known fluorophores exhibit fluorescence intermittency [90, 91], though quantum dots with steady fluorescence have been engineered [92]. In bulk diamond, NV fluorescence intermittency is rare but it does occur. In nanodiamonds, the NV centers show an fluorescence intensity that jumps between different count rates but does not necessarily go to zero.

The fluorescence of NV centers in all nanoparticle diamonds I have measured is intermittent. When I shine a steady green laser beam on a fluorescent nanodiamond, the fluorescence jumps from one intensity to another. The intensities and time-scale for this blinking behavior vary from one particle to another. This variation is likely caused by variations in the local environment, such as surface effects and strain.

This blinking might arise from changes in the charge state of the NV center between the negatively charged state, NV^-, and the neutrally charged state, NV^0. The NV^- spectrum has a zero phonon line at 637 nm and a phonon sideband at longer wavelengths whereas the NV^0 spectrum has a zero phonon line at 575 nm (see, for example, Ref. [93, Fig. 2]). In this case I would expect the photoluminescence signal to alternate between these two spectra. Therefore I repeatedly measured the spectrum of a blinking NV center, then in post-processing, I sorted the repeated spectrum measurements according to whether they occurred during a bright or a dark interval. The result is shown in Fig. 3.8, where the bright spectrum and the dark spectrum are plotted together. Other than a change in overall intensity, there is no significant change in the spectrum lineshape, suggesting that a shift in strength between emission at 637 nm and emission at 575 nm is not

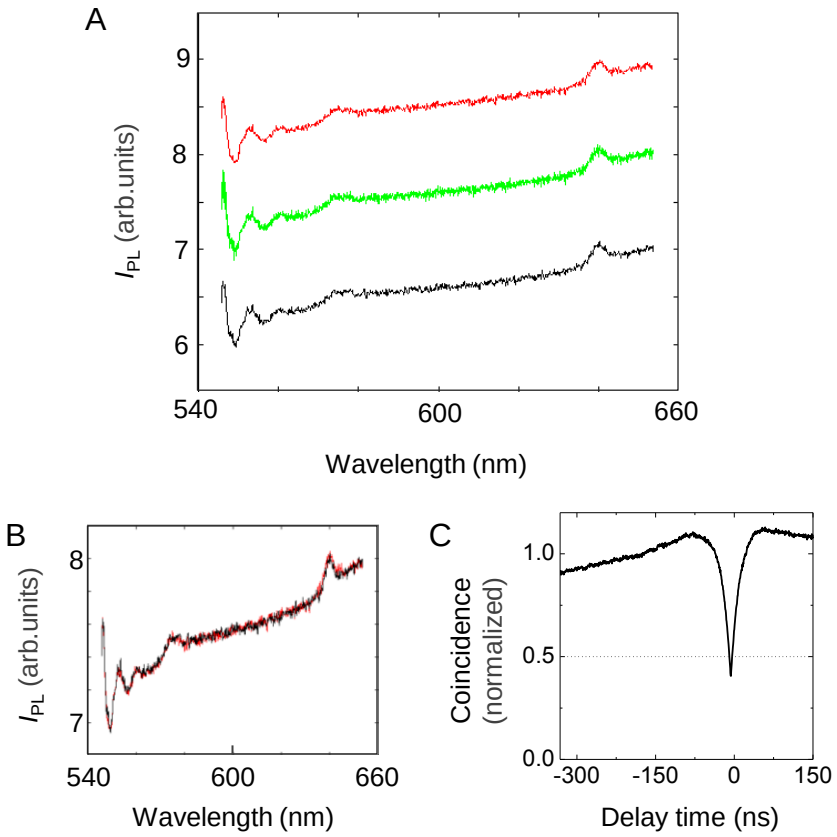

Figure 3.8: (*A*) Comparison of spectra from bright intervals (red) and dark intervals (black). The average spectrum is shown in green. The peak at 575 nm is the zero phonon line (ZPL) of the NV^0 center and the peak at 637 nm is the ZPL of the NV^- center. (*B*) To facilitate comparison between the two curves, I shifted them vertically so that they overlap. I do not observe a significant change in the ZPL at 575 nm or at 637 nm when the blink occurs. (*C*) The antibunching curve for this NV center dips below 0.5, indicating that this is a single NV center emitting single photons. This was measured with a 580 nm long pass filter to remove the green excitation laser.

the cause of the intensity intermittency.

As a second test, I used the two-APD collection path, splitting the signal between APD 1 and APD 2 with different filters in front of each APD. Only photons between 580 nm and 600 nm were detected at APD 1, corresponding to a detection of the NV^0 state. APD 2 only detected photons with wavelength greater than 640 nm, corresponding to a detection of the NV^- state. If the blinking corresponded to the color state flipping with the alternating charge state, we would expect the two signals at the two APDs to alternate: when one signal is strong, the other would be weak and vice versa.[2] However, this is not what I observed. As shown in Fig. 3.9*A*-*B*, when one signal is strong, the other is also strong. An improvement to these measurements might be to use a shorter wavelength excitation laser because the absorption band of NV^0 is weaker at 532 nm than at shorter wavelengths. Nevertheless, 532 nm is within the absorption band of both charge states of the NV center. Therefore this points to the possibility of a different explanation for the blinking behavior.

One of the methods I used for analyzing the intermittent fluorescence came from work with blinking quantum dots [94]: I plot histograms of the blink duration in Fig. 3.10. (See also Ref. [95].) Again, there is a great deal of variation from one NV to another. The histogram data were found to fit to an exponential decay curve in some cases (Fig. 3.10*A*-*B*), a power law decay curve in other cases (Fig. 3.10*C*) and in some cases the data appeared to be between the two decay curve types.

An additional consideration is that sometimes the blinking appears to occur between more than two levels of I_{PL}, as shown in Fig. 3.11.

[2] If we suspected the blinking might be an artifact of the detector, we would expect only one detector to show a blink and not the other. However, the two APDs detect simultaneous blinks.

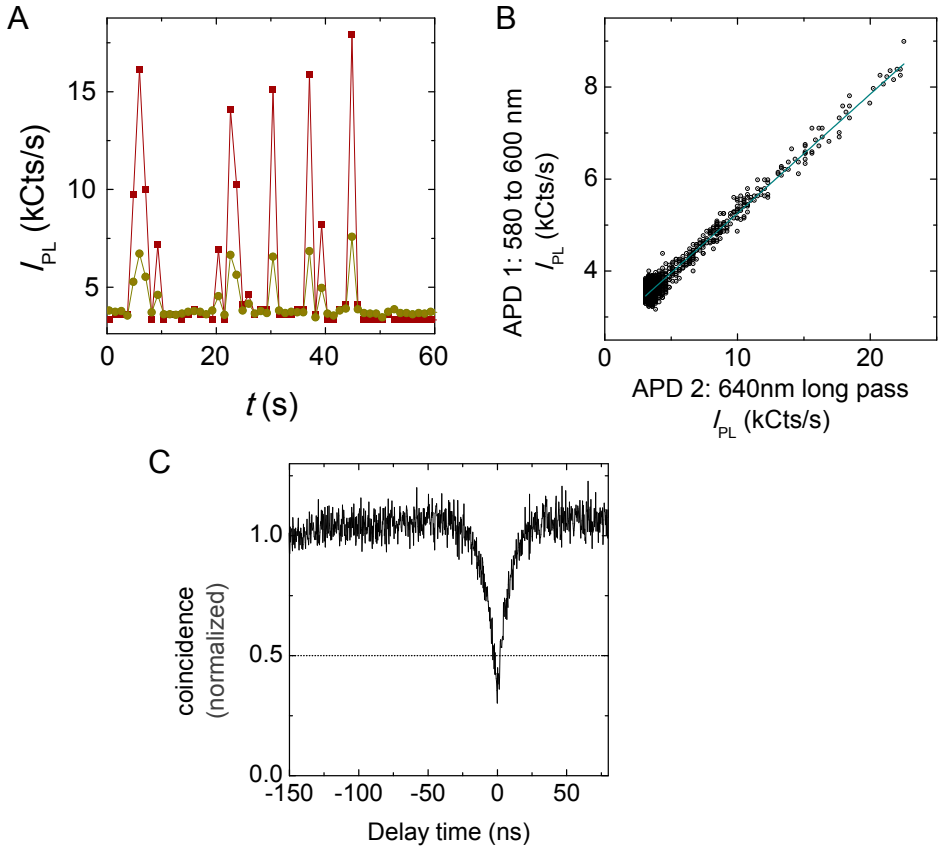

Figure 3.9: A single NV center with blinking detected in two color ranges. (*A*) The red data show I_{PL} as detected by APD 2, detecting photons in wavelengths corresponding to the NV^- state. The dark yellow data show I_{PL} as detected by APD 1, detecting photons in wavelengths corresponding to the NV^0 state. The blinking is observed to occur in tandem at both wavelengths, rather than alternating between the two color states. (*B*) To summarize the blinking data shown in (*A*), for each time t, I plotted the count rate detected by one APD against the other. Again, these data clearly show that the blinking occurs in tandem at both wavelengths; otherwise the slope of the line would be negative. Rather, an increase in I_{PL} at one wavelength range corresponds to an increase in I_{PL} at the other range. (The signal detected from 580 nm to 600 nm is weaker than that measured with > 640 nm, because the 20 nm bandwidth is so much narrower and because the spectrum is generally peaked closer to 700 nm.) (*C*) The antibunching curve for this single NV center dips below 0.5.

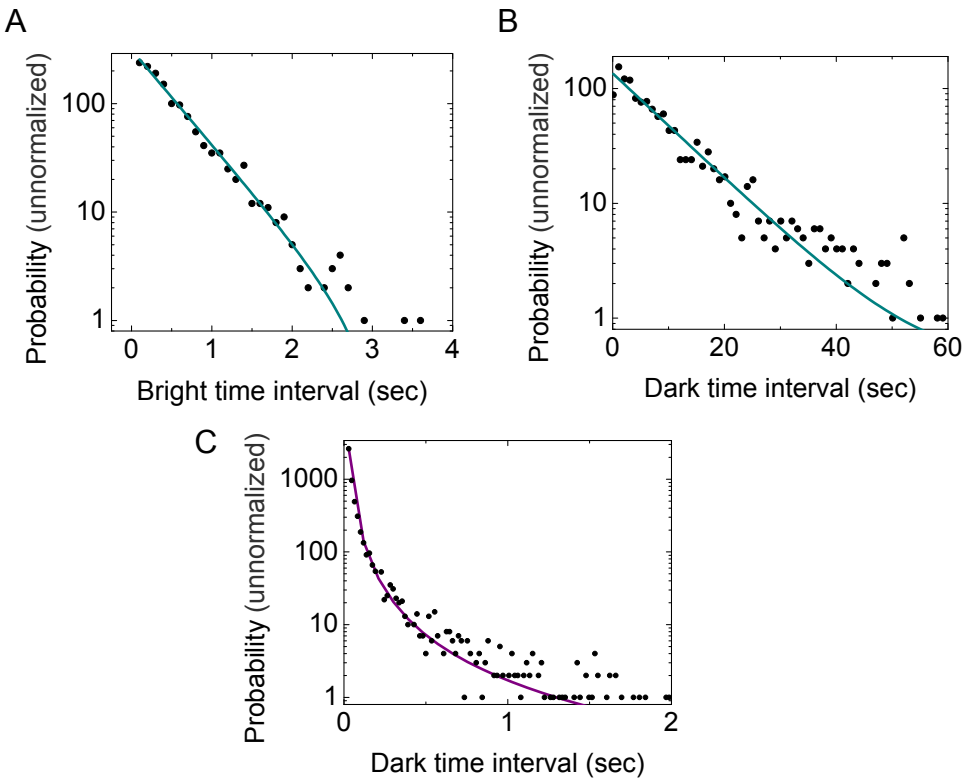

Figure 3.10: Histograms of NV center blinking duration. (*A*-*B*) The bright time intervals and dark time intervals for a single NV center (the same NV center as Fig. 3.9), with curve fits (dark cyan curves) to exponential decay curves. (*A*) The bright time interval decay time constant is 9.5 sec and (*B*) the dark time interval decay time constant is 0.50 seconds. (*C*) The dark time intervals for a different NV center, with curve fit (purple curve) to a power law decay, Probability $\propto \Delta t_{\text{dark}}^{-2.07}$.

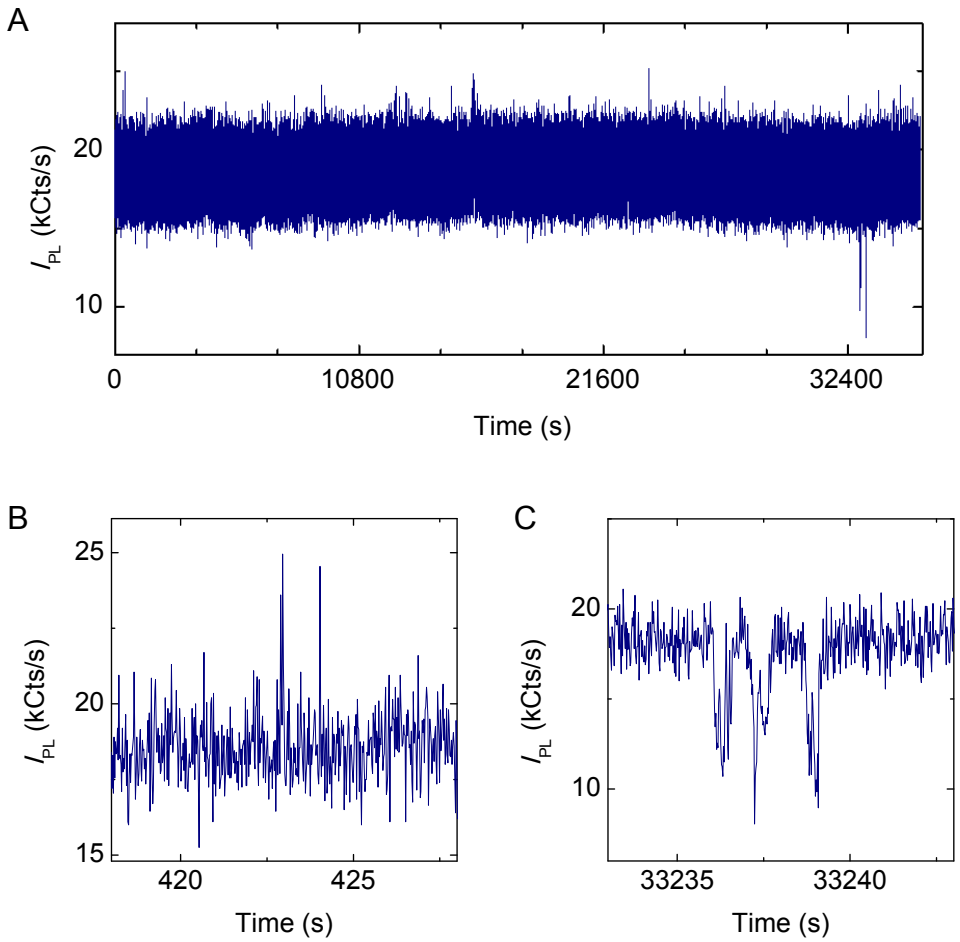

Figure 3.11: The fluorescence intermittency may include three or more intensity levels. (*A*) I_{PL} as a function of time, measured on a single NV center overnight. Data are collected at a rate of 50 Hz. The antibunching dip for this NV center is shown in Fig. 3.7. (*B*) A closer look at brighter blinks. (*C*) A closer look at darker blinks.

The cause of this blinking behavior is likely to be similar to the cause of blinking behavior in quantum dots, nanowires, and other fluorophores. Several different mechanisms have been proposed to explain this behavior. One suggested mechanism is that of Auger processes in ionized nanocrystals, where a charge moves to a surface-trap state, changing the fluorescence intensity [96, 97]. Kuno et al. [98, 99] propose that the tunnel-barrier heights or widths might change so that the electron-transfer rate fluctuates. Frantsuzov and Marcus [100] attribute the blinking to hole trapping associated with Auger ionization. Shimizu et al. [101] and Tang and Marcus [102] describe a diffusion-based mechanism, where the trap-state energy varies randomly so that the charge hopping only occurs when the trap-state reaches a particular energy [103].

3.5 Polarization

The NV center absorbs more light when the excitation beam is linearly polarized at certain angles with respect to the axis of the NV. Rotating the polarization of the excitation laser reveals this effect.

3.5.1 Calculating the angular dependence of the absorption of an NV center

The absorption of a single transition dipole is proportional to $|\mathbf{p}\cdot\mathbf{E}|^2$, where $\mathbf{E}$ is the electric field vector of the exciting laser beam and $\mathbf{p}$ is the dipole, which we treat classically. An NV center has two transition dipoles, each perpendicular to the axis of the NV center [13], as shown in Fig. 3.12*A*, so the combined absorption (i.e. excitation) is

$$\text{Absorption} \propto |\mathbf{p}_1\cdot\mathbf{E}|^2 + |\mathbf{p}_2\cdot\mathbf{E}|^2.$$

Although a highly focused Gaussian beam includes electric fields at multiple angles, we approximate that the electric field that excites the NV center is perpendicular to the axis of the microscope objective. We also assume that the electric field is linearly polarized.

To describe the orientation of the two dipoles, we begin by describing the orientation of the NV axis as a function of an azimuthal angle, ϕ, and a polar angle, θ, which is the angle between the NV axis and the axis of the objective. If $\hat{N}$ is a unit vector pointing along the direction of the symmetry axis of the NV center, as shown in Fig. 3.12*B*, we have

$$\hat{N} = \sin\theta\cos\phi\,\hat{x} + \sin\theta\sin\phi\,\hat{y} + \cos\theta\,\hat{z}.$$

Next we define two unit vectors that are each perpendicular to the NV axis and to each other,

$$\begin{aligned}\hat{u} &= -\sin\phi\hat{x} + \cos\phi\hat{y} \quad \text{and}\\ \hat{s} &= \hat{N}\times\hat{u} = -\cos\theta\cos\phi\hat{x} - \cos\theta\sin\phi\hat{y} + \sin\theta\hat{z}.\end{aligned}$$

These vectors $\hat{u}$ and $\hat{s}$ span a plane that is perpendicular to the NV axis. The two dipoles are perpendicular to each other and lie in this plane, so we define their orientation, $\hat{p}_1$ and $\hat{p}_2$, using an arbitrary rotation angle α in the plane,

$$\hat{p}_1 = \frac{\mathbf{p}_1}{|\mathbf{p}_1|} = \hat{u}\cos\alpha + \hat{s}\sin\alpha \quad \text{and} \quad \hat{p}_2 = \frac{\mathbf{p}_2}{|\mathbf{p}_2|} = \hat{N}\times\hat{p}_1, \tag{3.2}$$

as shown in Fig. 3.12*C*. By symmetry, $|\mathbf{p}_1| = |\mathbf{p}_2|$. Hence we account for the geometry of the two transition dipoles of the NV center. Then the angular dependence of the absorption of a single NV center is

$$\text{Absorption} \propto 1 - \cos^2\phi\sin^2\theta, \tag{3.3}$$

as shown in Fig. 3.12*D*. Thanks to symmetry, the rotation α of the NV center about its axis does not affect the absorption. If the NV center is saturated

at some angles then the absorption will reach a maximum at those angles, which will affect the shape of the curve.

3.5.2 Methods and Results

In order to control the linear polarization of the excitation beam, it has been necessary to understand that the dichroic that reflects the excitation laser into the objective does not preserve linear polarization. It transforms linearly polarized light into elliptically polarized light. By preparing the excitation beam in a calibrated elliptical polarization, I can obtain linearly polarized light [104, Fig. 8]. A half wave plate (HWP) and a quarter wave plate (QWP) adjust the polarization of the beam. I temporarily place a linear polarizer at the sample space, positioned perpendicular to the desired linear polarization angle, and I adjust the HWP and QWP until the excitation beam is extinguished by the linear polarizer, indicating that the polarization is now at the desired angle. I repeat this until I have a set of calibrated polarization angles.

One challenge that arose was that I was using mica polarizers. They have an advantage that they have a large area, which is desirable for use with the laser beam that is expanded enough to overfill the back opening of the high-NA objective. However, the polarizers have a wedge and as they are rotated, they move the excitation beam by up to a micron on the sample space. As a work-around for this, I re-adjusted the collection path for each polarization setting to ensure that the APDs were obtaining signal from the same location as the excitation beam.

Figure 3.13 shows the fluorescence intensity of a single NV center (established by antibunching measurement) as a function of excitation polarization

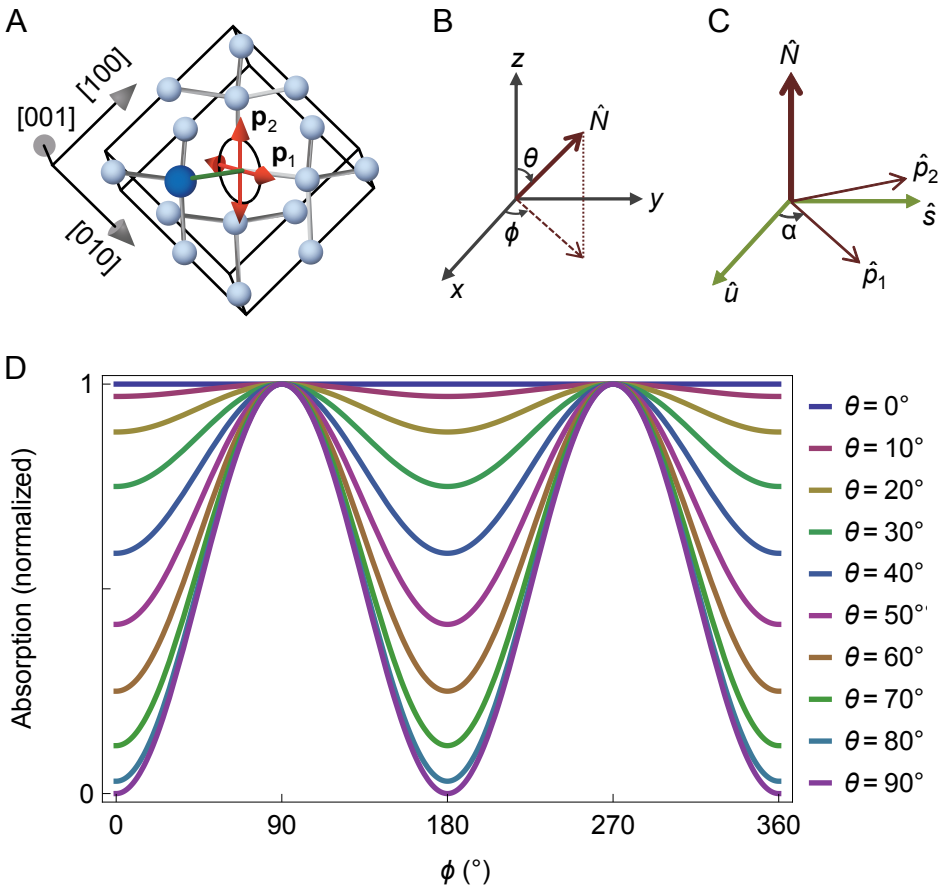

Figure 3.12: The absorption of a single NV center, assuming the excitation is not saturating the NV center. (*A*) Embedded in the diamond crystal lattice, the NV center has two perpendicular transition dipoles, $\mathbf{p}_1$ and $\mathbf{p}_2$. (*B*) The unit vector $\hat{N}$ is parallel to the NV center axis. The polar angle θ and the azimuthal angle ϕ describe the orientation of the NV center. The optical axis is parallel to $\hat{z}$. (*C*) The two transition dipoles of the NV center lie in a plane perpendicular to the NV center axis. We define this plane with the unit vectors $\hat{u}$ and $\hat{s}$. (*D*) Calculated absorption versus ϕ. The absorption of a linearly polarized electric field by an NV center depends on both ϕ and θ, where ϕ is the azimuthal angle between the polarization axis and the NV axis. (*A*) is reprinted by permission from Macmillan Publishers Ltd: *Nature Physics* [13], copyright 2005.

angle.

3.6 Optical trapping and fluorescence

In order to combine optical trapping and confocal fluorescence in a commercial microscope, it was necessary to use a double-decker filter cube turret to hold both dichroic mirrors. This allows the two beams to be brought into the objective simultaneously. The optical apparatus will be described in detail in Section 5.1.

The trapping volume and the measurement volume must overlap each other. The objective is designed for minimal chromatic aberration in the visible wavelengths, but there is chromatic aberration between 532 nm and 1064 nm. To align the two beams, I used the following method: I checked that both the excitation beam and the trapping beam were very well collimated, neither converging nor diverging over a long distance. Then I focused the two beams through the objective, and adjusted the sample up and down until I viewed the focus of each laser with the camera. Due to chromatic aberration, these focal planes were displaced axially. The collimated lasers are not confocal, but the camera is also viewing through the objective, effectively doubling the amount of chromatic aberration. I adjusted the collimation of the excitation laser, but *not* until the focal planes of the two beams would appear together (because the camera view is not accurate). Rather, I adjusted it until the distance between the two focal planes appeared halfway closer. This should bring the two beams to the same focus. The collection path must also be re-aligned.

However, that method of achieving confocal beams is very indirect. One direct technique is to trap fluorescent nanodiamonds and measure the fluo-

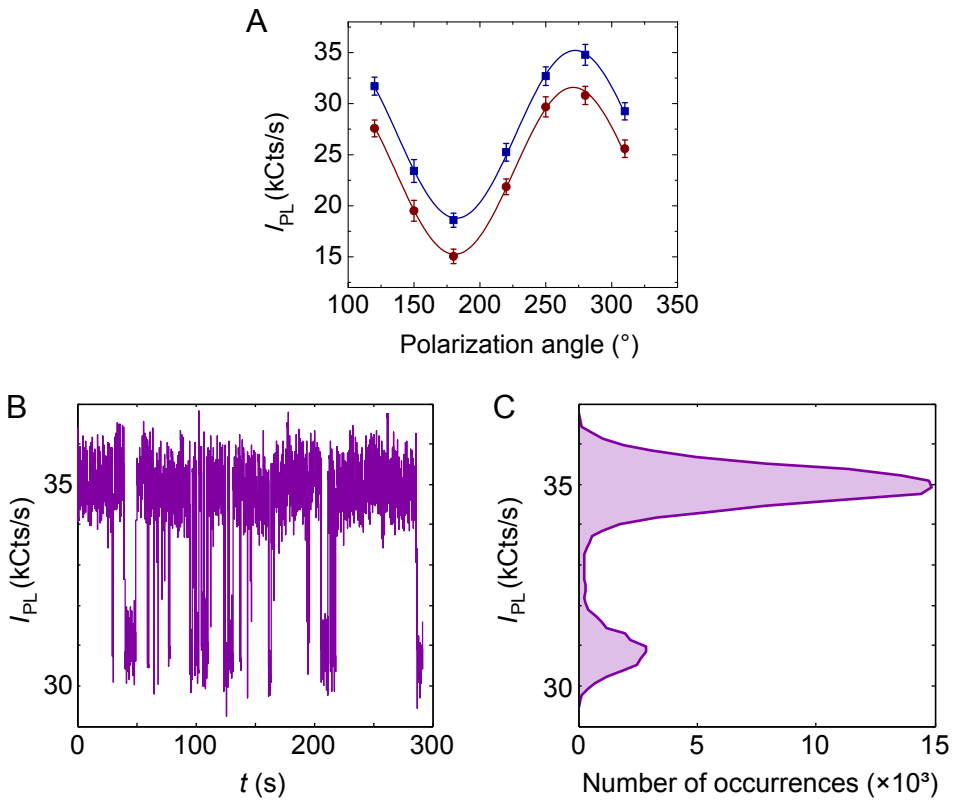

Figure 3.13: (*A*) The fluorescence intensity of a single NV center shows blinking at multiple excitation polarization angles. The blue data were taken when the NV center was more brightly fluorescent; the red data were taken when the NV center was more dimly fluorescent. These data are fit to Eq. (3.3), and I obtain $\theta \approx 45°$ for this NV center, ignoring the effects of dark counts and imperfect polarization. This NV center is displaying blinking between two fluorescence levels. (*B*) An example of the raw data: I_{PL} versus time at excitation polarization angle 280°. The data collection rate is effectively 5 Hz after post-processing smoothing. (*C*) The data in (*B*) are gathered into a histogram to determine the average I_{PL} when the NV was more brightly fluorescent and when the NV was more dimly fluorescent. This histogram provides the information for one blue datapoint and one red datapoint in (*A*), and the width of each histogram peak is shown as an errorbar in (*A*). The count rate in (*C*) is on the y-axis rather than the x-axis to emphasize the connection to (*B*).

rescence. (It is best to start with the indirect technique so that the measurement volume and the trapping volume are partially, if not fully, overlapping.) The excitation beam should not be adjusted unless it is possible to adjust both the excitation beam and the collection path together while measuring the fluorescence. Therefore, the trapping beam should be adjusted with the steering optics to maximize the measured signal by bringing the trapped nanodiamonds into the measurement volume.

A third method is to fabricate a pinhole with a focused ion beam and place it at the focus (i.e. after the objective and immersion oil). The pinhole must have the approximate same width as the beam waist diameter. If both beams pass through the pinhole, then they are confocal. The beam power transmitted through the pinhole may be measured one-by-one to ensure that each beam is passing through the pinhole, but if the measurements are taken at different times, then the pinhole must have very good position stability to ensure that it is not moving between measurements. Alternately, the two beams could be collected after the pinhole and split with a dichroic filter for independent simultaneous measurements to ensure that both beams are passing through the pinhole at the same location.

Measuring the fluorescence of optically trapped nanodiamonds will be discussed further in Section 4.3 and is a crucial step towards measuring magnetic field with optically trapped nanodiamonds (see Chapter 5).

♦♦♦

Chapter 4

Electron spin resonance of NV centers in nanodiamonds

Electron spin resonance (ESR) is a way to drive transitions between energy levels and therefore probe the energy level structure of a material. Section 1.2 discusses mechanisms of electron spin resonance in negatively charged NV centers in diamond. In this chapter, we will discuss the microwave antenna, then discuss noise and the software lock-in for increasing signal to noise and the dynamics of the nanodiamonds in the trap. We conclude the chapter with the ESR spectrum of immobilized nanodiamonds.

By measuring the electron spin resonance (or optically detected magnetic resonance) of the NV center, we measure the energy level splittings of the center. This opens the door to sensing using the energy level structure of the NV center.

4.1 Antenna

In order to apply microwave fields, we designed a microwave antenna that is lithographically patterned on the glass coverslip and impedance-matched

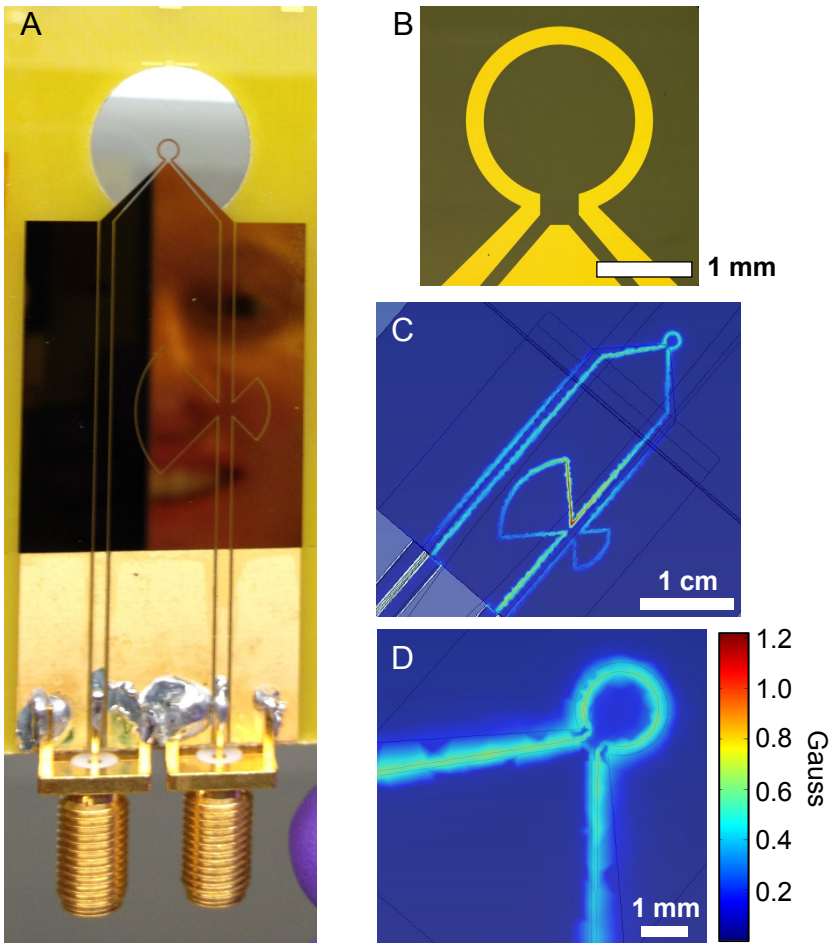

Figure 4.1: The microwave antenna. (*A*) Photograph of the antenna/coverslip assembly mounted on a SMA-connectorized printed circuit board. The hole in the antenna mount under the antenna loop permits optical access. (*B*) Micrograph of the antenna: gold patterned on glass. (*C-D*) Magnetic flux density norm in the plane of the microwave antenna when $f_{\mathrm{MW}} = 2.8$ GHz, modeled in COMSOL Multiphysics. Irregularities in the simulated magnetic flux density norm, appearing as splotching near the antenna trace edges, are an artifact of the chosen finite element meshing. (*C-D*) Image courtesy of David J. Christle; (*B-D*) are reprinted from Ref. [1].

near 2.87 GHz to optimize power transmission and reduce heating. The antenna/coverslip assembly is shown in Fig. 4.1*A-B*. The antenna is impedance-matched to 50 Ω using a bowtie-style radial stub. The design was developed using COMSOL Multiphysics simulations. The magnetic flux density in the vicinity of the antenna resulting from a microwave field is shown in Fig. 4.1*C-D*.

4.2 Noise and software lock-in

Random fluctuations in the photoluminescence of optically trapped fluorescent nanodiamonds present experimental challenges in measuring the ESR contrast. The Brownian motion in solution, collisions between nanoparticles, and the entry and exit of nanodiamonds from the optical trap contribute to a large, low-frequency noise component in the observed I_{PL}. Blinking (see Section 3.4) may augment the observed fluorescence fluctuations. To a lesser extent, spin bath effects [105] also contribute to noise.

The photoluminescence noise from optically trapped fluorescent nanodiamonds shows a dependence on the photoluminescence, I_{PL}. In general, the standard deviation of the experimentally measured I_{PL}, σ_{expt}, grows with increased I_{PL} beyond that expected from Poisson statistics or shot noise behavior, namely $\sigma_{\mathrm{expt}} > \sigma_{\mathrm{shot}} = \sqrt{N}$, where $N = I_{\mathrm{PL}}\Delta t$, and Δt is the time interval in which photon counts are measured. Figure 4.2 illustrates this dependence and plots the ratio $\sigma_{\mathrm{expt}}/\sqrt{N}$ as a function of I_{PL}. For low values of I_{PL}, σ_{expt} approaches shot noise (dotted line in Fig. 4.2), but reaches values nearly 6 times shot noise at higher I_{PL}. Analysis of noise is performed only on plateaus with stable I_{PL}, therefore the plotted noise, especially for higher I_{PL}, is a lower limit. This increase in noise likely arises from dynamics

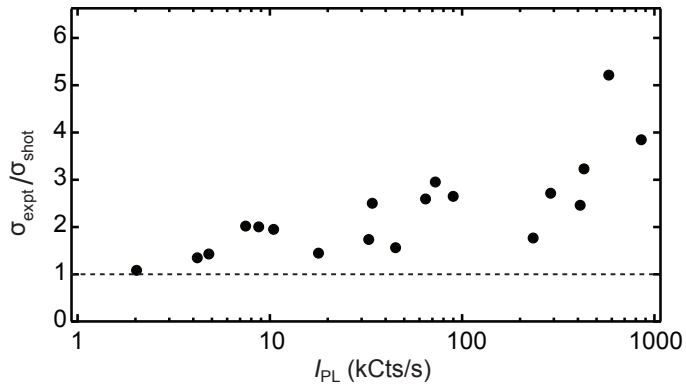

Figure 4.2: The ratio of the measured standard deviation of I_{PL} to shot noise for optically trapped nanodiamonds as a function of I_{PL}. Shot noise was obtained from total counts in a time interval Δt, $\sigma_{shot} = \sqrt{I_{PL}\Delta t}$. The dotted line corresponds to the case when the measured noise equals the shot noise. This illustrates the increase in overall photoluminescence noise observed as the optical trap becomes more populated with fluorescent nanodiamonds. Figure courtesy of Benjamín J. Alemán. Reprinted from Ref. [1].

of multiple particles in the trap. Any motion of particles in the trap, arising from collisions, thermal vibrations, trap instability, and other sources, will have a corresponding contribution to the noise in I_{PL} because each particle will experience a varying degree of electric field strength from the laser beam determined by its position in the measurement volume. In addition, when a fluorescent particle enters the trap, the abrupt increase in I_{PL} contributes to the noise.

To increase the signal-to-noise ratio during ESR measurements, we use commercial nanodiamonds from Adámas Nanotechnologies (Fig. 4.3) that have been He^+ irradiated to create vacancies and subsequently annealed to form approximately 500 NV centers per ~100 nm diameter nanodiamond. Additionally, by performing amplitude modulation of the applied microwaves with a software-based photon-counting lock-in technique [106, 107], we improve the signal-to-noise ratio of the experiment

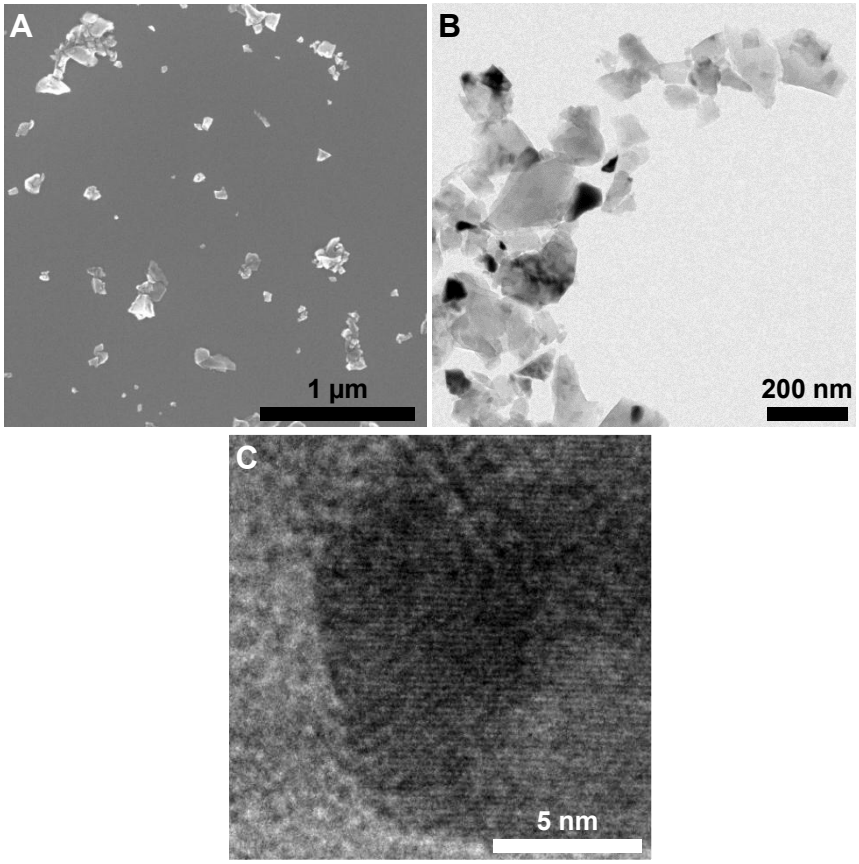

Figure 4.3: (*A*) Scanning electron micrograph and (*B*-*C*) transmission electron micrograph of nanodiamonds (ND-500NV-100nm, Adámas Nanotechnologies). Images courtesy of Benjamín J. Alemán and Stephan Kraemer. Reprinted from Ref. [1].

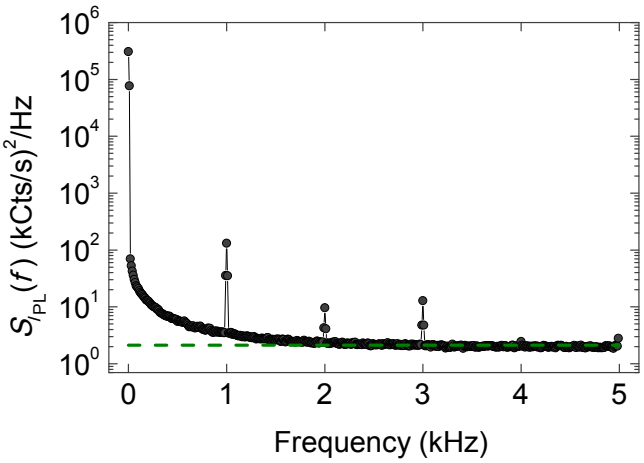

Figure 4.4: Bimodal power spectral density $S_{I_{PL}}(f)$ of the luminescence with on-resonant microwaves at frequency f_{MW} = 2.87 GHz and amplitude-modulation frequency f_{AM} = 1 kHz. The peak at 1 kHz corresponds to the NV response to the amplitude-modulated carrier signal. Peaks at multiples of 1 kHz are harmonics. The green dashed line shows the expected shot noise floor for the bimodal power spectral density, $S_{I_{PL}}(f) = I_{PL}$ = 2.1 MHz. The noise at f_{AM} = 1 kHz is higher than the expected floor, indicating that the measurement is not shot-noise limited. The power spectral density was calculated from I_{PL} data taken for 100 ms, our typical lock-in time; the average of 1000 sets of data is shown. Adapted from Ref. [1].

by more than a factor of ten. In this way, ESR dips in I_{PL} are converted to peaks in the differential luminescence ΔI_{PL}. Figure 4.4 shows the power spectral density of I_{PL} for trapped nanodiamonds, displaying both the low-frequency noise and the NV ESR contrast response from resonant microwaves that are amplitude modulated at 1 kHz.

The software lock-in is shown in Fig. 4.5*A*-*B*. Since f_{MW} is resonant with the energy splitting between the $m_s = 0$ and the $m_s = +1$ or -1 states, I_{PL} drops while the microwave is on, such that I_{PL} oscillates in time at frequency f_{AM}. Locking in to the signal, we extract the differential fluorescence signal ΔI_{PL}. As we sweep the microwave frequency f_{MW}, ΔI_{PL} remains low when f_{MW} is off resonance with the transition between spin states and

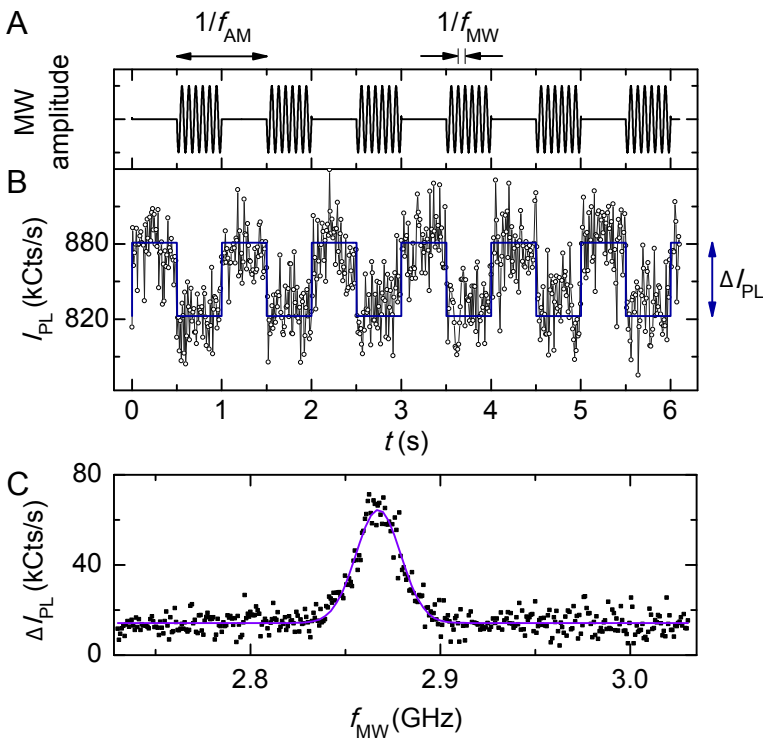

Figure 4.5: Amplitude-modulated ESR of NV centers in optically trapped nanodiamonds in water. These nanodiamonds are irradiated. (*A*) Schematic of the amplitude-modulated microwave signal used in the experiments, with f_{MW} lowered for illustration. (*B*) The read-out contrast of the fluorescence signal created by the modulation amplitude of resonant, $f_{\mathrm{MW}} = 2.868$ GHz, microwaves, modulated at frequency $f_{\mathrm{AM}} = 1$ Hz. We use a software lock-in (blue line) to extract the differential fluorescence intensity $\Delta I_{\mathrm{PL}} = 58.5$ kCts/s or the relative ESR signal $\Delta I_{\mathrm{PL}} / I_{\mathrm{PL,\,high}} = 6.64\%$, where $I_{\mathrm{PL,\,high}} = I_{\mathrm{PL}}$ when the microwave is off. (*C*) Optically detected ESR spectrum obtained by sweeping f_{MW} while $f_{\mathrm{AM}} = 1$ kHz. The Gaussian fit (purple line) has a FWHM of 27.8 MHz and a peak at 2.87 GHz, which is the zero-field splitting between the $m_s = 0$ and the $m_s = \pm 1$ levels. This ESR spectrum was collected in 150 s. Reprinted from Ref. [1].

increases when f_{MW} is on resonance. If X and Y are the two output channels of the lock-in, and $R = \sqrt{X^2 + Y^2}$, then $\Delta I_{\mathrm{PL}} = 2R$. Figure 4.5$C$ shows the ESR spectrum for an ensemble of trapped nanodiamonds in water with no externally applied magnetic field. The nanodiamonds are specified to be 100 nm in diameter and contain 500 NV centers each. The spectrum has a linewidth of 23.6 MHz and a maximum at 2.87 GHz, agreeing with the expected zero-field splitting of the NV center. Off resonance, the curve does not go to zero because the lock-in is not phase locked.

4.3 Trapping nanodiamonds

The optical trap attracts nanodiamonds and traps them. Figure 4.6 shows the measured I_{PL} and contrast ΔI_{PL} before and after turning on the trapping beam. As the trapping beam remains on, fluorescent nanodiamonds stochastically enter the trap and cause I_{PL} to increase in discrete steps, with coincident rises in ΔI_{PL} indicating the presence of NV centers. When the trapping beam is turned off, the nanodiamonds scatter out of the trap from Brownian motion, causing the luminescence to cease.

4.4 ESR of immobilized nanodiamonds

Figure 4.7 shows ESR of nanodiamonds that are drop-cast onto the coverslip. To mitigate the influence of non-NV-based fluorescence, we photobleach the sample with the 532 nm laser, intending to let only the non-photobleaching NV fluorescence signal remain. The ESR signal splits into more than two peaks, indicating that the measurement ensemble includes multiple NV centers at different orientations. These nanodiamonds are not irradiated.

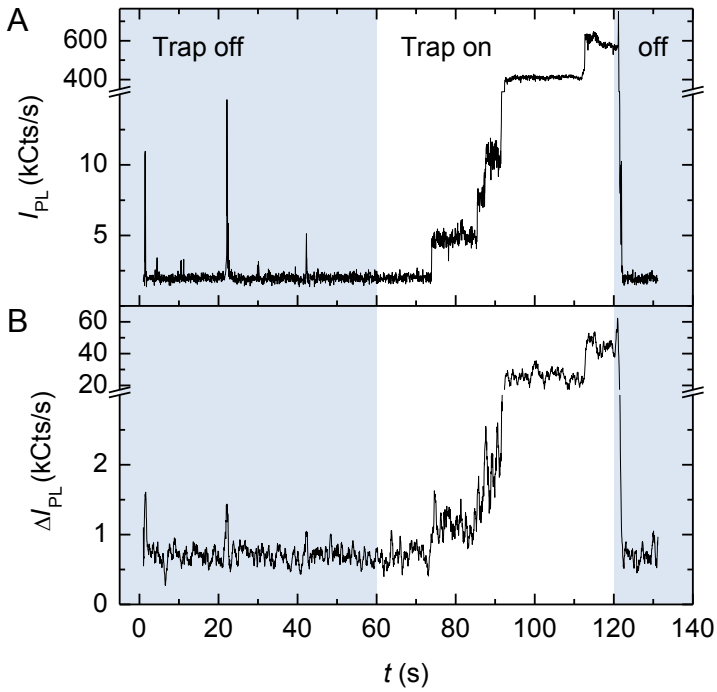

Figure 4.6: (*A*) Time trace of I_{PL} showing discrete steps of increasing photoluminescence as clusters of NV centers enter the optical trap with the green excitation laser on. The trapping laser is initially blocked (blue shaded times). The trapping laser is unblocked at time t = 60 s, and I_{PL} remains low, indicating an empty trap, until the first discrete step at $t \sim 73$ s. At time $t \approx 120$ s, the trapping laser is blocked to release the particles from the trap, with I_{PL} dropping commensurately. (*B*) The coincident ESR response of resonant microwaves, applied at f_{MW} = 2.87 GHz, indicates that the fluorescent particles in the trap are indeed nanodiamonds that contain NV centers. Data in (*B*) are smoothed. Reprinted from Ref. [1].

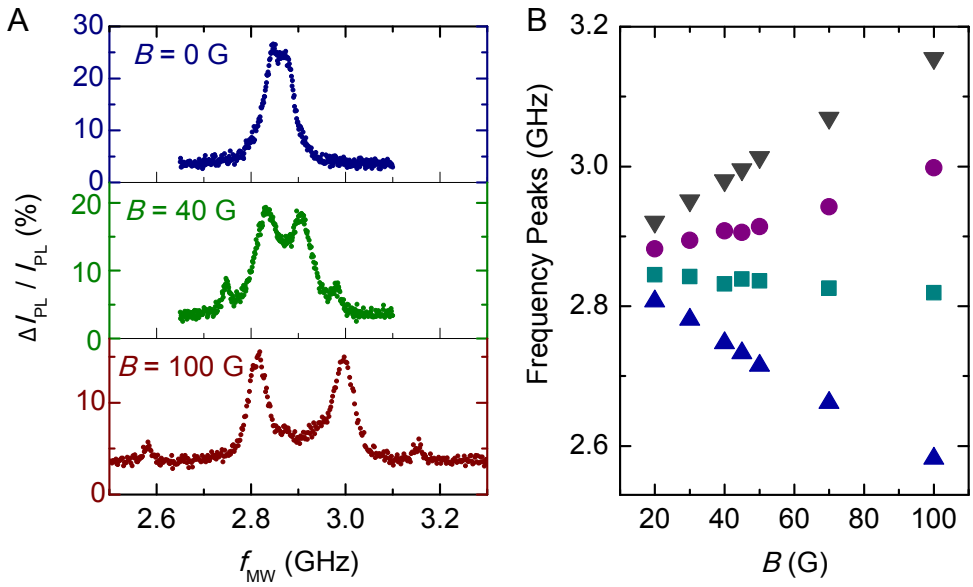

Figure 4.7: (*A*) Optically detected ESR of dry nanodiamonds drop-cast and dried on a coverslip near a microwave antenna. These nanodiamonds are not irradiated. While a single spin will split into two peaks, here we observe at least four peaks, which indicate we are measuring multiple NV centers at different orientation with respect to the applied magnetic field. The frequency peaks of these ESR spectra are plotted in (*B*) as they vary with magnetic field. Reprinted from Ref. [1].

For convenient comparison to conventional continuous wave ESR measurements, the divisor for normalization is the I_{PL} detected during those intervals when the microwave is off, as calculated by the lock-in software.

Next, we combine the ESR spectrum measurements with the optically trapped nanodiamonds in the presence of a magnetic field.

Chapter 5

Magnetometry with optically trapped nanodiamonds

In this chapter, we use the optically trapped nanodiamonds to measure an external magnetic field.

5.1 Apparatus and techniques

Figure 5.1 shows a schematic of the optical apparatus and Fig. 5.2 shows the measurement geometry. The 1064 nm trapping laser optically traps nanodiamonds in solution in water. The 532 nm laser excites photoluminescence and polarizes the NV spin into the $m_s = 0$ spin state. These lasers are attenuated to 30 mW and 90 μW, respectively, measured at the back opening of the objective. The photoluminescence signal is detected by the APD. The 1064 nm and 532 nm beams are combined using dichroic mirrors. The oil-immersion objective with 1.3 NA focuses the beams onto the sample. We mount the sample on the 3-axis piezoelectric stage, which enables moving the antenna/coverslip assembly by up to 100 microns in X and Y and up to 20 microns in Z. We calibrate the electromagnet (EM050-6H-222, APW Com-

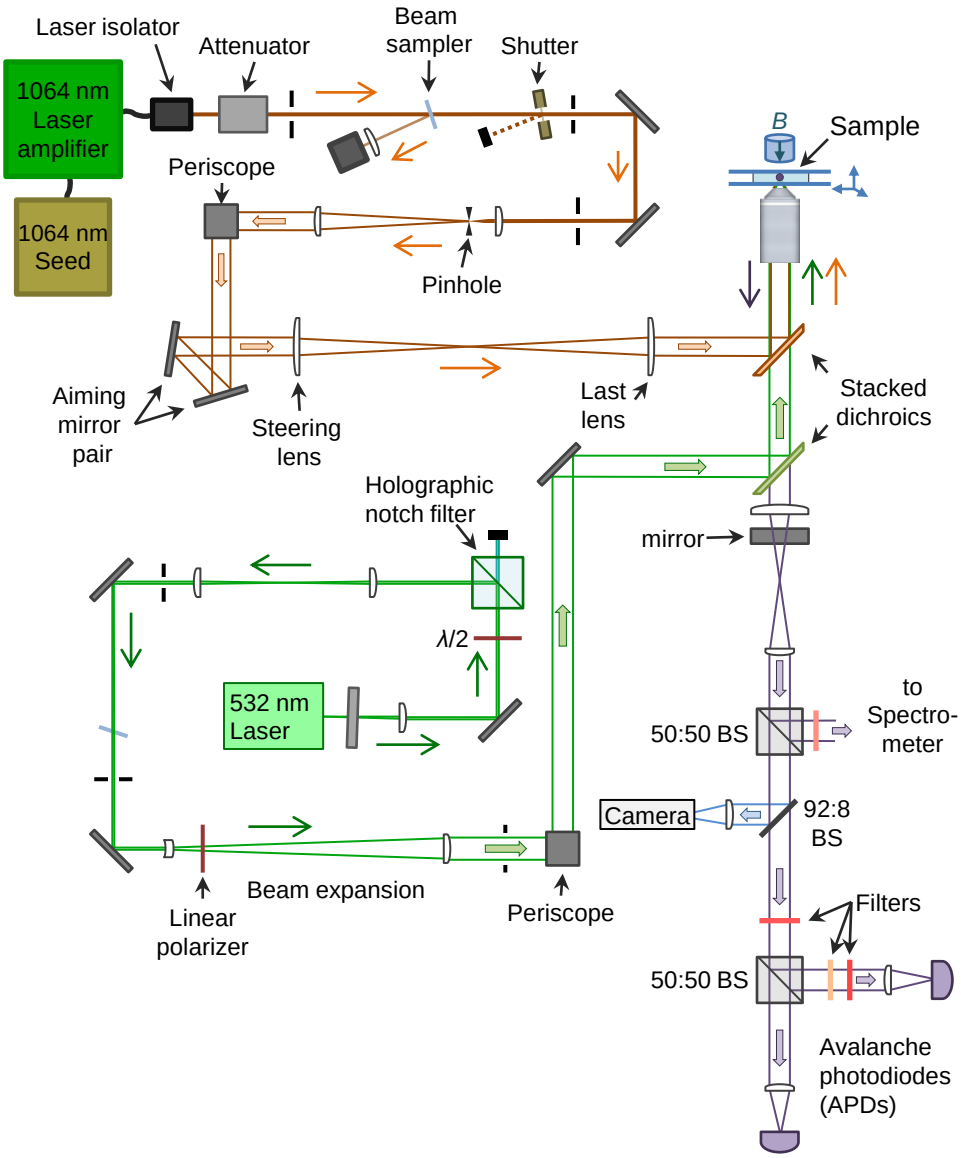

Figure 5.1: The apparatus, with an optical tweezers path (1064 nm laser), an excitation beam path (532 nm laser), and a collection path. All three optical paths are adjusted to the sample focus at the sample so that the photoluminescence signal is collected from the same confocal region where the nanodiamonds are trapped. During measurements, the trapping location remains fixed while a 3-axis piezoelectric stage controls the sample position. See also Figs. 2.6 and 3.2 and Tables 2.1, 3.1, and 3.2.

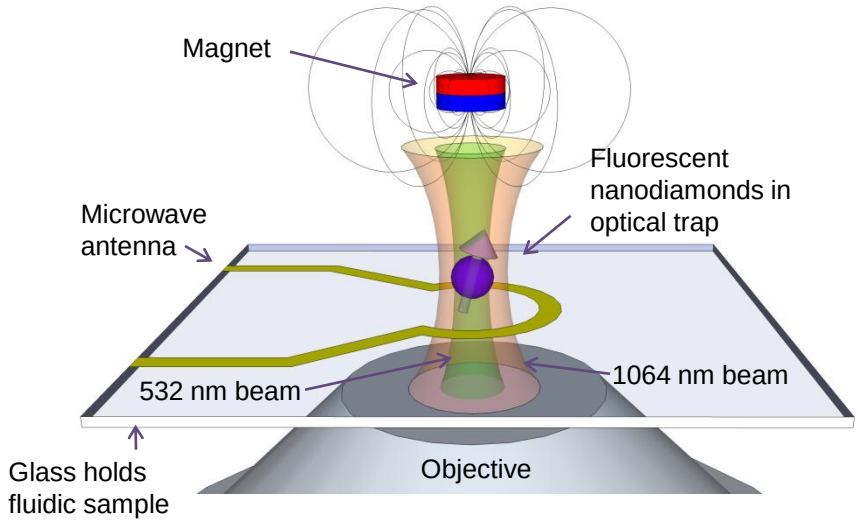

Figure 5.2: Schematic of nanodiamond optical trapping, photoexcitation, and luminescence detection at the focus of the objective. The magnetic field is applied externally, along the axis of the objective. The microwave antenna and glass coverslip are also shown. Reprinted from Ref. [1].

pany; current provided by a Keithley 2400 Sourcemeter) with a Hall probe (HMMA-1808-VR probe and 455 DSP Gaussmeter, Lakeshore). A Hewlett Packard ESG-D4000A generates the microwave signal, which is amplified by an Amplifier Research 5S1G4. The optical signal is filtered with three filters: the 640 nm long pass, the 1064 nm notch block, and the XB11 filter[1] to remove laser scatter prior to APD photon detection. All optical measurements were taken with room lights off to avoid extra photon counts.

[1] The XB11 filter blocks both 1064 nm and 532 nm, which could seem redundant. I found that three filters better removed the laser scatter than one or two, but the signal to noise ratio might be improved by using fewer filters.

5.2 Estimating trap population of nanodiamonds

The trap collects an ensemble of nanoparticles, each specified to contain at least 500 NV centers. From Eq. (2.3) we expect that the trapping laser has a beam waist diameter of $2w_0 = 0.4$ µm and the excitation laser has a beam waist diameter of $2w_0 = 0.2$ µm. The trap width is in good agreement with the width observed in optical images (see Fig. 2.14). The depth of focus is experimentally ~0.8 µm for the measurement volume (see Fig. 3.6), and the trapping laser is expected to have twice the depth of focus, ~1.6 µm. Therefore the trapping volume is approximately 0.1 µm^3 and the measurement volume is approximately 0.02 µm^3. Assuming a unity packing-fraction to make an order-of-magnitude estimate, the maximum number of 100 nm diameter particles, each of approximate volume 0.001 µm^3, that can occupy the trap and measurement volumes is ~100 and 20 particles, respectively. This corresponds to ~8000 NV centers in the measurement volume, assuming maximum packing and the minimum 500 NV centers per particle. However, we would expect only $20 \times 4 = 80$ NV orientations in the measurement volume at a given instant.

The highest stable I_{PL} we observed in our experiments was ~3000 kCts/s. Assuming this value corresponds to a fully packed trap with ~8000 NV centers (assuming only 500 NV centers per particle), we would expect each NV to contribute ~0.4 kCts/s. This value is close to the experimentally measured value of 1 kCts/s, obtained by measuring the minimum step height of I_{PL} as 35 nm diameter nanodiamonds (also from Adámas Nanotechnologies), each specified to contain approximately 1 to 4 NV centers, enter the optical trap.

5.3 Optical collection efficiency

The I_{PL} we measure is approximately 1 kCts/s per NV center, which is about two orders of magnitude lower than the I_{PL} we might expect. This arises from a number of different factors, include the following:

1. The collection path includes multiple beamsplitters that enable multiple simultaneous measurements but that also decrease signal to the APD, as shown in Fig. 5.1. Only 23% of the collected I_{PL} reaches each APD.

2. The NV centers are not aligned along a particular axis for optimal excitation and collection and are likely rotating in the trap. NV centers that are not aligned with the optical axis have decreased excitation and collection efficiencies. Assuming an isotropic distribution of NV orientations, the I_{PL} of the ensemble will scale as
$$\frac{\text{mean amplitude}}{\text{aligned amplitude}} = \frac{\frac{1}{2}\int_0^{\pi} A_1(\theta)\sin\theta\, d\theta}{A_1(0)} = 57\%$$
compared to the I_{PL} of an aligned ensemble of NV centers, using the expression for $A_1(\theta)$ that appears in Eq (5.4).

3. The dichroic that directs the trapping laser into the objective also reflects away the longer wavelengths of the NV center emission spectrum, as shown in Fig. 5.3. (For comparison, see Fig. 3.1.) This decreases the collected light to 58%. We obtained this percentage by measuring the count rate of dry 500-NV nanodiamonds drop cast on a coverslip, both with the 1064 nm dichroic in the optical path (5194 kCts/s) and without it (8992 kCts/s). One improvement to the collection efficiency would be to replace this dichroic with one that transmits rather than reflects wavelengths from 700 nm to 800 nm.

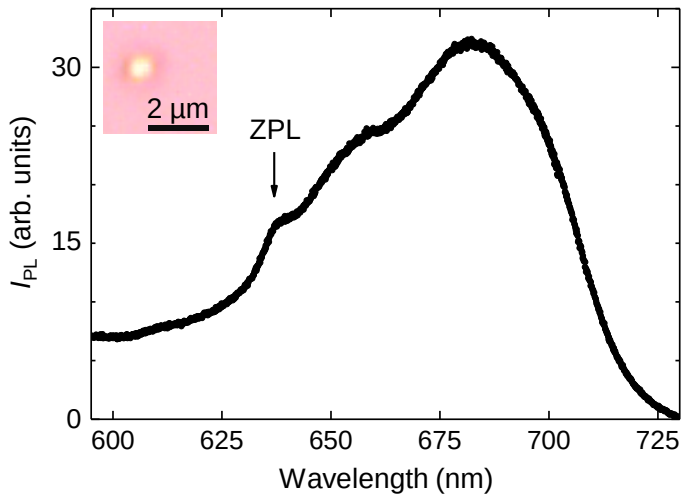

Figure 5.3: Photoluminescence spectrum of an ensemble of optically trapped nanodiamonds. The arrow marks the NV zero phonon line. The spectrum of the phonon sideband is attenuated for wavelengths longer than 700 nm because of a dichroic optical filter that reflects the trapping laser into the objective. These nanodiamonds are not irradiated. The photographic inset shows this nanodiamond ensemble in the optical trap. Reprinted from Ref. [1].

4. We have consistently observed that immobilized nanodiamonds show a decrease in count rate to ~60% when they are in water, even if the particle is adhered to the glass coverslip such that the optical pathway does not pass through a significant amount of water. This could be caused by surface effects of the nanodiamond. We obtained this percentage by measuring the count rate of a nanodiamond immobilized on the coverslip, both dry (50 kCts/s) and wet (31 kCts/s), for example.

5. We have attenuated the excitation laser so that the nanodiamonds are not saturated; they are emitting at ~60% of the saturated I_{PL}.

6. The three optical filters in the collection path, the 640 nm long pass, the 1064 nm notch block, and the XB11 filter (which blocks both 532 nm and 1064 nm) help remove laser scatter but they also likely attenuate

light at the emission wavelengths.

7. Misalignment of the optical paths is certainly a factor in decreasing the count rate. With chromatic aberration of the objective, it is not straightforward to axially align the infrared focus and the visible focus, so that the measurement volume is not necessarily fully overlapped with the trapping volume.

Taking only the first five items into account, we expect to see a reduction in I_{PL} to 3% of the maximum per NV center, with optical misalignment, especially caused by chromatic aberration (see Section 3.6), accounting for a further decrease.

While the count rate per NV center could certainly be increased (for example, by increasing the collection path efficiency and increasing the excitation laser power), in our ensemble measurements we did not find it necessary to increase the overall count rate, which reached as high as 3×10^6 counts/second. However, increasing the signal collection efficiency could improve the signal-to-noise ratio in future experiments and would be of particular value for measurements of single NV centers.

5.4 Modeling the ESR spectrum

To understand the lineshape and magnetic field dependence of the ESR spectra of the trapped ensemble, we develop a model consisting of a statistical average over all possible NV center orientations with respect to a fixed magnetic field, incorporating the directional dependence of the transition frequencies from the NV center Hamiltonian and the anisotropic excitation and collection efficiencies of our confocal microscope. In this model, the orientation

of the NV center's symmetry axis, relative to the magnetic field and optical axis, determines its ESR resonance frequency and contribution to the overall spectrum: a perpendicular orientation yields a minimal contrast contribution and frequency shift, while a parallel NV center gives a maximal contribution and shift (2.80 MHz/G). The NV centers contained in the nanodiamond ensemble are not expected to be aligned or oriented in any particular direction. In addition, the particles may rotate in the optical trap. Therefore, we model the ESR spectrum by assuming the NV centers are randomly oriented. Summing over an isotropic distribution of NV center orientations, we expect the overall ESR spectrum to have two broadened peaks, in accord with our experimental observations. To infer the model parameters and their associated uncertainties for each measured spectrum, we apply a Bayesian Markov Chain Monte Carlo approach [108] and plot the best-fit curves over the plotted data.

5.4.1 Angular dependence of the excitation

We begin by calculating the angular dependence of the excitation (i.e. absorption) of a single NV center. In Section 3.5.1, we found that the absorption of a single NV center is proportional to $1-\cos^2\phi\sin^2\theta$ (Eq. 3.3), as shown in Fig. 5.4*A*, where ϕ is the azimuthal angle between the excitation polarization axis and the NV center axis, and θ is the polar angle between the NV axis and the axis of the objective, as shown in Fig. 5.4*B*. The laser polarization would be important if the magnetic field were applied along a different axis with respect to the microscope objective, but our geometry has a symmetry so the polarization of the laser is not important. Laser polarization control could provide a route to vector magnetometry using an ensemble of randomly ori-

ented NV centers. For now, we have a system that is symmetric in ϕ, because the NV ensemble includes NV centers at every orientation. Therefore, we integrate over all ϕ to obtain

$$\text{Absorption} \propto 1 + \cos^2\theta, \tag{5.1}$$

as shown in Fig. 5.4*C*. We will integrate over all angles θ at a later point in the calculation.

Is Eq. (5.1) what we might expect? We can consider a few test cases to convince ourselves that it is. First, we can begin by assuming that there is no dependence on α of the NV center's rotation about its own axis. We showed it rigorously in Section 3.5.1, but it is not surprising that the rotation of the NV center about its own axis would have little effect on the NV center's ability to absorb the excitation beam. So we can arbitrarily fix $\alpha = 0$. Having fixed α, now $\hat{p}_1 = \hat{u}$ and $\hat{p}_2 = \hat{s} = \hat{N} \times \hat{u}$. Since $\hat{p}_1 = \hat{u}$ is perpendicular to the optical axis, the absorption of this dipole will have no dependence on θ. Let's say the first dipole has one arbitrary unit of absorption, regardless of the polar angle θ. In the case that the second dipole is perpendicular to the optical axis (i.e. if the NV is parallel to the optical axis), then the second dipole will also have one arbitrary unit of absorption. Adding that with the absorption of the first dipole, we have two arbitrary units of absorption when $\theta = 0$. However, in the case that the NV is perpendicular to the optical axis, then the second dipole will be parallel to the optical axis, and so it will have zero absorption. Then the total absorption will be one arbitrary unit when $\theta = \frac{\pi}{2}$. These two test cases agree with Eq. (5.1).

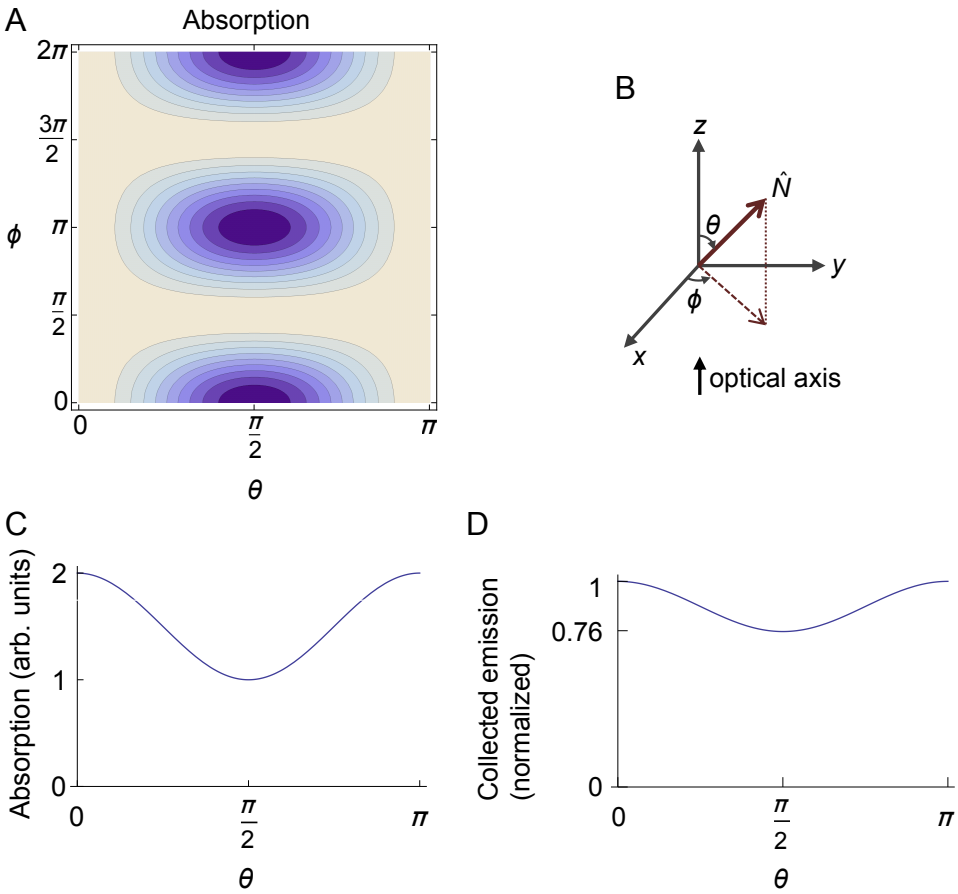

Figure 5.4: The angular dependence of the absorption and emission of a single NV center. (*A*) The absorption of a single NV center depends, in general, on both ϕ and θ, according to Eq. (3.3). (*B*) The unit vector $\hat{N}$ is parallel to the NV center axis. The polar angle θ and the azimuthal angle ϕ describe the orientation of the NV center. The optical axis is parallel to $\hat{z}$. (*C*) Integrating the absorption over all angles ϕ, we obtain the absorption of the NV center as a function of the polar angle θ, according to Eq. (5.1). (*D*) The emission collected by the 1.3 NA objective, assuming uniform absorption over all angles in the collection cone, has a slight dependence on the angle the NV center makes with the optical axis, according to Eq. (5.2).

5.4.2 The emission collected from a single NV center

In order to calculate the collected emission of the transition dipole, we begin by calculating the angular part of the emission function of a dipole $\mathbf{p}$, which we treat classically. The component of the dipole that is orthogonal to the direction vector $\hat{r}$ is

$$\mathbf{p}_\perp = \mathbf{p} - \hat{r}\,(\hat{r}\cdot\mathbf{p}),$$

where

$$\hat{r} = \sin\vartheta\cos\varphi\,\hat{x} + \sin\vartheta\sin\varphi\,\hat{y} + \cos\vartheta\,\hat{z}.$$

The power radiated by the dipole is proportional to $|\mathbf{p}_\perp|^2$ [109]. We integrate over the collection cone of the microscope objective to find the angular part of the power collected,

$$P_1 \propto \int_0^{\vartheta_{\max}} \int_0^{2\pi} |\mathbf{p}_\perp|^2 \sin\vartheta\, d\varphi d\vartheta$$

where P_1 is the collected emission of one dipole and $\vartheta_{\max}$ is the maximum angle at which the objective can collect light; since NA = $n\sin\vartheta_{\max}$ with n = 1.515 and NA = 1.3, we have $\vartheta_{\max} = 59.1°$. At this point in the calculation we do not take into account the excitation anisotropy. We assume that the objective has uniform efficiency for collecting light from all angles in its collection cone. The result is

$$P_1(\mathbf{p}) \propto 2.43\,(p_x^2 + p_y^2) + 1.25\,p_z^2,$$

where p_x, p_y, and p_z are the components of $\mathbf{p}$. This is not a very strong dependence on dipole orientation. An objective with a lower NA would have a stronger angular dependence of the collection.

We recall Eq. (3.2) to describe the geometry of the two dipoles associated

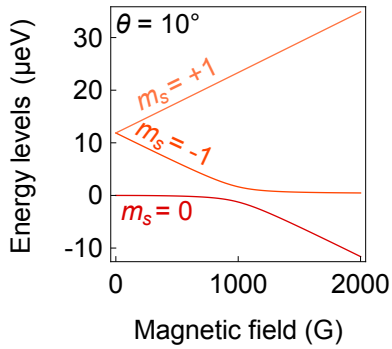

Figure 5.5: The ground state energy eigenvalues of an NV center as a function of magnetic field when the angle between the NV axis and the magnetic field vector is $\theta = 10°$, calculated from Eq. (5.3). There is a level anti-crossing near 1026 G.

with the NV center. Then the collected emission of a single NV is

$$P_{\mathrm{NV}} = P_1(\mathbf{p}_1) + P_1(\mathbf{p}_2), \quad \text{which evaluates to}$$
$$P_{\mathrm{NV}} \propto 2.43 + 2.43\cos^2\theta + 1.25\sin^2\theta, \tag{5.2}$$

as shown in Fig. 5.4*D*. We see that the angular part of the collected emission P_{NV} depends only on θ, the angle between the NV center axis and the axis of the microscope objective. Thanks to symmetry, it does not depend on α or ϕ.

5.4.3 Zeeman splitting

The energy levels of the spin states of the ground state of the NV center are calculated directly from the ground state Hamiltonian,

$$\hat{H}_{\mathrm{NV}} = D\hat{S}_z^2 + g\mu_{\mathrm{B}}\mathbf{B}\cdot\hat{\mathbf{S}}, \tag{5.3}$$

where $D = h \cdot 2.87$ GHz $= 11.8$ μeV, $g = 2.00$, $\mu_{\mathrm{B}} = 5.79 \times 10^{-9}$ eV/G is the Bohr magneton, and the components of $\hat{\mathbf{S}}$ are the spin 1 matrices. Terms of the Hamiltonian not relevant to this calculation have been suppressed. Some

calculated energy levels are shown in Fig. 5.5. The difference between spin levels gives the frequency of the peaks measured in the ESR spectrum of a single NV center. That is, for a given field **B**, the spectrum will have peaks corresponding to

$$hf_{0\to+1} = E_{m_s=+1} - E_{m_s=0} \quad \text{and}$$
$$hf_{0\to-1} = E_{m_s=-1} - E_{m_s=0},$$

where $E_{m_s=0}$, $E_{m_s=-1}$, and $E_{m_s=+1}$ are the three eigenvalues of $\hat{H}_{\mathrm{NV}}$. Figure 5.6 shows how these spin sublevel frequencies depend on the angle of the NV center to the magnetic field. For zero field, $E_{m_s=-1} = E_{m_s=+1}$, so the peaks are degenerate, $hf_{0\to-1} = hf_{0\to+1} = D$. The frequencies split with magnetic field. For NV centers aligned with the magnetic field, and for fields below 1026 G, the frequencies are linear in the magnetic field:

$$hf_{0\to\pm1}(\theta=0) = D \pm g\mu_{\mathrm{B}}B,$$

where $g\mu_{\mathrm{B}}/h = 2.80$ MHz/G and θ is the angle between the NV axis and the magnetic field vector. However, the frequency $f_{0\to-1}$ varies more with θ than $f_{0\to+1}$ does, causing an asymmetry at nonzero fields.

5.4.4 ESR spectrum of a single NV center

We assume that each NV center in the distribution has an ESR spectrum with two Gaussian functions, one peak centered at $f_{0\to-1}$ and the other at $f_{0\to+1}$. These frequencies depend on the magnetic field strength and the angle θ between the magnet and the axis of the NV center. Note that for our geometry, where the magnet and the objective share an axis (see Fig. 5.2 or 5.1), this is the same angle as the angle between the NV center and the axis of the microscope objective; for the purposes of the calculation, we assume no misalign-

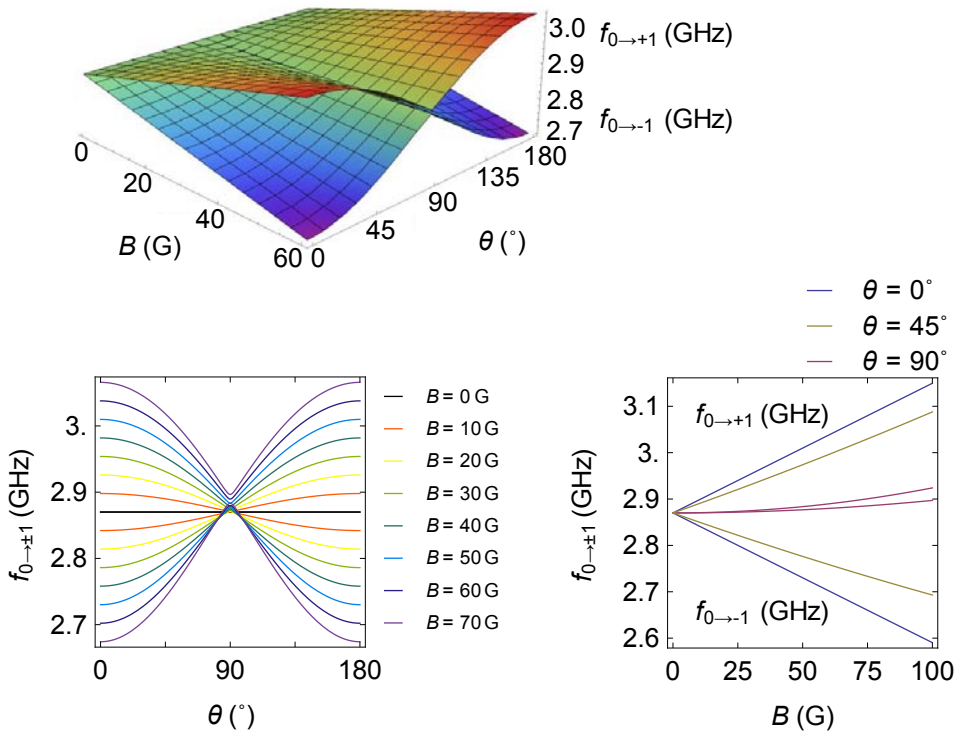

Figure 5.6: The calculated spin sublevel transition frequencies $f_{0\to-1}$ and $f_{0\to+1}$ depend on both the magnitude B of the magnetic field and the angle θ between the NV symmetry axis and the magnetic field vector. Here we assume the zero-field splitting is $D = 2.87$ GHz. Top subfigure is reprinted from Ref. [1].

ment between the magnet and the microscope objective. The amplitude of this double-Gaussian single-NV ESR spectrum depends on the angle θ between the axis of the NV center and the axis of the microscope objective:

$$A_1(\theta) \propto (1+\cos^2\theta)\,(2.43+2.43\cos^2\theta+1.25\sin^2\theta), \tag{5.4}$$

where Eqs. (5.1) and (5.2) give the angular dependence of the absorption and collected emission of the NV center (see Fig. 5.7). Note that the NV center can emit a photon via either dipole, regardless of the dipole that absorbed a photon. We approximate that the microwave power affects the NV centers uniformly, regardless of NV orientation or microwave frequency. Therefore

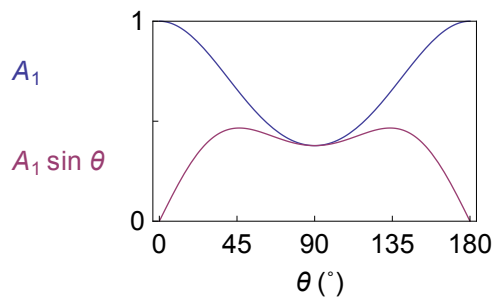

Figure 5.7: The calculated angular dependence A_1 of the measured I_{PL} of an NV center and the contribution to I_{PL} of each angle θ in an isotropic ensemble of NV centers, $A_1 \sin\theta$. The normalized function $A_1(\theta)$ is plotted, showing the dependence of the measured I_{PL} of an NV center as a function of the angle between the NV center and the optical axis (see Eq. (5.4)). For an ensemble of randomly oriented NV centers, the angular dependence of the contribution from NV centers of each angle is multiplied by the probability, $\sin\theta$, of any given NV center from the ensemble being in that orientation. (See Eqs. (5.5) and (5.6).)

the ESR spectrum $C_1(B,\theta; f_{\mathrm{MW}})$ of a single NV has angular dependence

$$C_1(B,\theta; f_{\mathrm{MW}}) = A_1(\theta)\,[G(f_{0\to+1}; f_{\mathrm{MW}}) + G(f_{0\to-1}; f_{\mathrm{MW}})], \tag{5.5}$$

where $G(x_0; x)$ is a Gaussian function of x centered at x_0, and $f_{0\to+1}$ and $f_{0\to-1}$ are functions of B and θ. Examples of C_1 curves are plotted in Fig. 5.8. The widths of the two Gaussian functions must be determined empirically and are assumed to be equal to each other.

5.4.5 ESR spectrum of an isotropic ensemble of NV centers

The measured ESR spectrum is a sum of the ESR spectra of all the NV centers in the measurement volume. Therefore, to obtain the ESR spectrum of an isotropic ensemble of NV centers, $C_{\mathrm{model}}(B, f_{\mathrm{MW}})$, we integrate over all angles θ,

$$C_{\mathrm{model}}(B, f_{\mathrm{MW}}) = \int_0^{\pi} C_1(B,\theta; f_{\mathrm{MW}}) \sin\theta \, d\theta, \tag{5.6}$$

and the result is plotted in Fig. 5.9. Note that for an isotropic distribution of

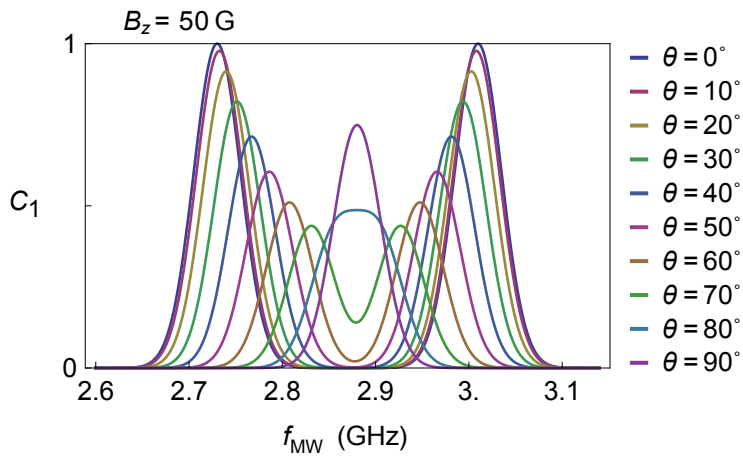

Figure 5.8: The modeled ESR spectrum, $C_1(B,\theta; f_{\mathrm{MW}})$, for a single NV center, normalized and plotted for a series of NV orientations. These orientations range from $\theta = 0°$, with maximal splitting, to $\theta = 90°$, with minimal splitting. The magnetic field is assumed to be parallel to the axis of the objective and to have a magnitude of 50 G. The width of each Gaussian is set to 50 MHz. In the case of a continuous wave ESR measurement without lock-in, the Gaussian functions would be dips instead of peaks. We assume the excitation laser is not saturating the NV center. The effects of laser polarization angle ϕ are ignored because this calculation uses Eq. (5.1) rather than Eq. (3.3); this has a physical interpretation for *single* NV measurements only if we assume the laser is circularly polarized. (We can ignore the effects of laser polarization angle regardless of laser polarization in the experiment, however, because we will use C_1 to describe isotropic *ensembles* of NV centers.) The curves for $\theta = 0°$ are the strongest, but in an isotropic ensemble, the probability of having an NV center perfectly aligned with the objective/magnet axis is vanishingly small.

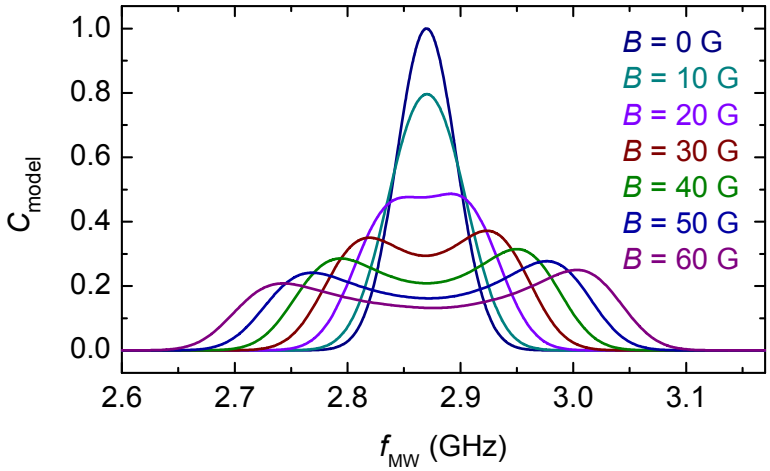

Figure 5.9: Modeled ESR spectra for an ensemble of randomly oriented NV centers, calculated from Eq. (5.6), normalized, and plotted with a zero-field width of 61.7 MHz and D = 2.87 GHz. The magnetic field is assumed to be parallel to the axis of the objective. Reprinted from Ref. [1]. These curves are also plotted as a colormap in Fig. 5.11*B*.

NV centers, more NV centers will be perpendicular to the axis of the magnet/objective than parallel to this axis, with a probability distribution given by $\sin\theta$, as shown in Fig. 5.7. The model predicts two peaks separating and broadening as the magnetic field is increased. The right peak is predicted to be taller and narrower than the left peak because of the asymmetry between $f_{0\to-1}$ and $f_{0\to+1}$.

Although the ESR spectra modeled here are effectively an average over ensembles of randomly oriented NV centers, the spectra at low magnetic fields retain qualitative similarities to measurements of aligned NV centers: the spectra exhibit two distinct peaks that shift approximately linearly as a magnetic field is applied. However, unlike aligned NVs, the spectral peaks broaden with increased magnetic field.

5.4.6 Fitting the ESR curves

The model of Eq. (5.6) can be fit to the data by adjusting the following fitting parameters:

1. Magnetic field B_{est}, which can then be compared to the calibrated magnetic field,

2. The crystal field splitting D, which should be near 2.87 GHz, but which may vary with a change in strain or temperature,

3. The background signal y_0 measured far off resonance, which is not zero because the lock-in lacks phase-locking, so the data has a dc offset when the noise exceeds the signal (e.g. when f_{MW} is off resonance),

4. Amplitude, which is not determined by the model because Eq. (5.4) only gives a proportionality, and

5. The width w of the Gaussian function G in Eq. (5.5), which equals the zero-field width, and which must be determined empirically.

The sixth parameter that is determined from the fitting algorithm is noise, σ_{est}. We use a Markov Chain Monte Carlo approach to fitting, in which the parameters iterate towards the best fit, then continue to iterate to explore the parameter space. Ignoring the first few iterations, this exploration of the parameter space gives the probability curve for the parameter to have certain values. The peak of the probability curve gives the best fit, the mean of the probability curve gives the best estimate of the value for the parameter, and the spread of the probability curve gives the error for the fit. More details of the fitting algorithm are available in the SI Text of Ref. [1].

5.5 Results and Discussion

We optically trapped an ensemble of nanodiamonds near a microwave antenna in an external magnetic field and measured the ESR spectra (Fig. 5.10). Measured ESR spectra up to 60 G are shown in Fig. 5.11*A*. In Fig. 5.11*B*, we fix the model parameters found at 0 G, adjust only the parameter for the applied magnetic field, and obtain excellent qualitative agreement with the data.

By fitting the data to modeled curves as described in Section 5.4.6, we determine the magnetic field B_{est} measured by the trapped nanodiamond ensemble and plot it against the applied magnetic field in Fig. 5.12. The theoretical magnetic sensitivity is related to the noise and the lineshape of the associated ESR spectrum. At a given microwave frequency, f_{MW}, small changes in the measured contrast signal $C \equiv \Delta I_{\text{PL}}/I_{\text{PL}}$ occur with a change in magnetic field according to $\delta C = \delta B \frac{\partial C}{\partial B}$ and thus the most efficient magnetometry measurement would take place at the f_{MW} where this derivative is largest in magnitude. In the low-field limit, this maximum in $\left|\frac{\partial C}{\partial B}\right|$ occurs for f_{MW} centered between the two peaks, approximately $f_{\text{MW}} = 2.87$ GHz; however, once the two peaks split by about twice the FWHM, the most sensitive f_{MW} for measurement occurs on the downward slope of the highest frequency peak. If the minimum detectable change in magnetic field is δB_{min}, then the estimated optimal magnetic sensitivity is [21, 110]

$$\eta_B = \delta B_{\text{min}} \sqrt{\Delta t} = \frac{\sigma_C \sqrt{\Delta t}}{\max \left|\frac{\partial C}{\partial B}\right|}, \tag{5.7}$$

where σ_C is the estimated standard deviation of C for measurement time Δt from the analysis.

From the model, we can gain an intuition for the optimal conditions for dc magnetometry in our system. Since the splitting of the peaks is approx-

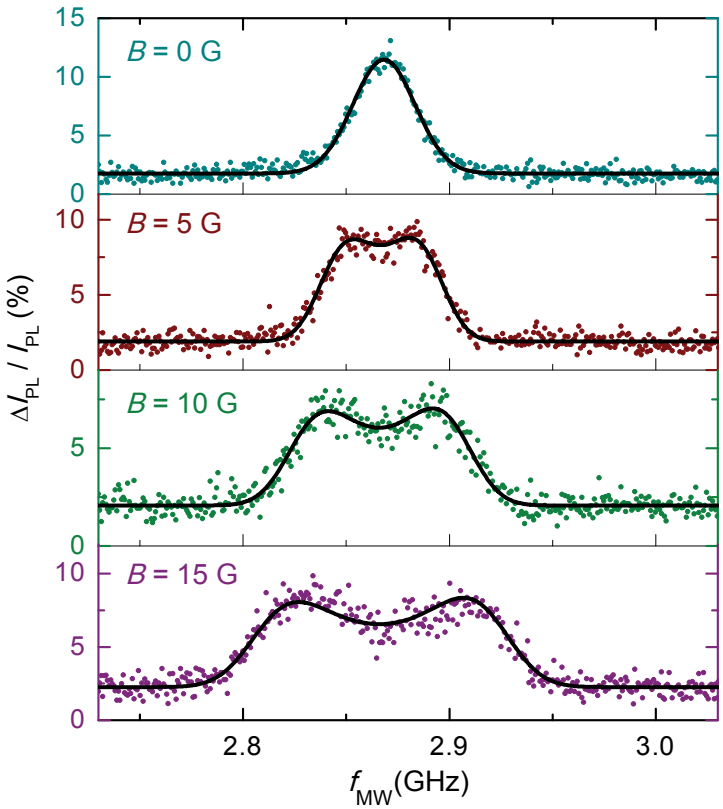

Figure 5.10: Optically detected ESR spectra of trapped nanodiamond ensembles at calibrated low field strengths. The best-fit curve from the model with five fitting parameters is shown (black lines). The measurements occurred at calibrated applied magnetic fields of 0, 5, 10, and 15 G. By fitting to the model, we obtain estimated magnetic fields of 1.5, 9.4, 14.5 and 20.8 G, respectively. Each ESR spectrum has a total acquisition time of about 200 s. $I_{PL} \approx 510$ kCts/s and $f_{AM} = 1$ kHz. Reprinted from Ref. [1].

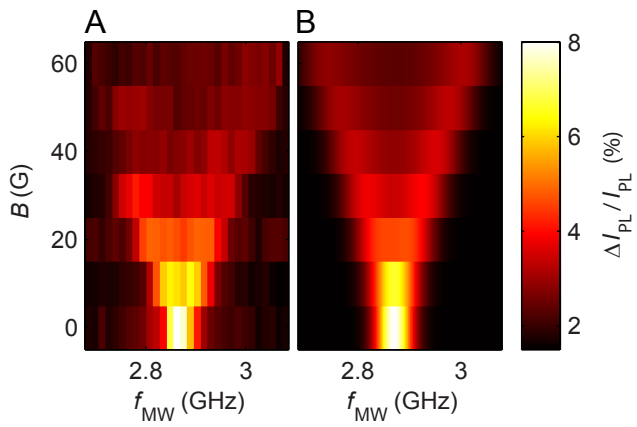

Figure 5.11: (*A*) Measured ESR spectra of trapped nanodiamonds up to 60 G. (*B*) Predicted ESR spectra from the model are computed by fixing all parameters except B to their best-fit values at zero field and adjusting B to the calibrated field values. Reprinted from Ref. [1].

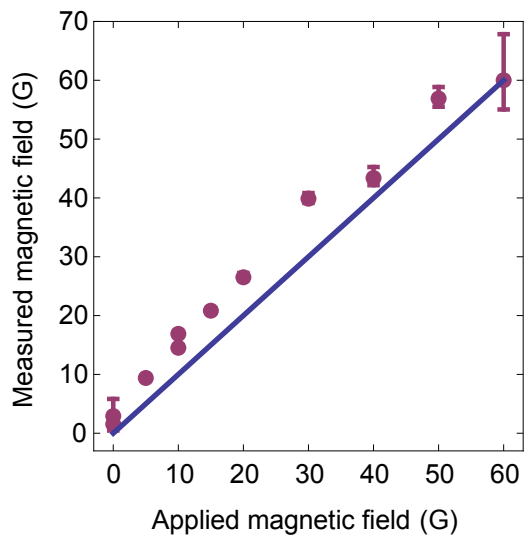

Figure 5.12: Magnetic field B_{est} measured by the trapped NV ensemble versus applied magnetic field. Plotted error bars are 95% highest probability density intervals. The measured values are inferred from the model fitting while the applied values are set by an *ex situ* calibration. The solid line of unit slope and zero offset is used to compare the data against the ideal measurement. Reprinted from Ref. [1].

imately linear with increasing field and the contrast diminishes, we would expect that the magnetic sensitivity generally worsens at higher fields. Similarly, when the two resonances become unresolved near zero magnetic field, the line shape becomes weakly dependent on B and the sensitivity is poor. For this reason, an optimum condition exists at low fields ~5 G when the resonances are split but the contrast is still large.

We calculate the maximum-magnitude derivative of the model with respect to the parameter B and corresponding error parameter over samples from the Markov Chain Monte Carlo output to obtain a probability density for the optimal sensitivity given the lineshape inferred from experiment. The mean estimated and 68.2% highest probability density intervals [111] from this distribution are plotted as black circles in Fig. 5.13. In addition, the standard deviation of the marginal density for B, scaled by the square root of the total acquisition time, serves as an empirical measure of the actual sensitivity obtained in the experiment, and is plotted (open purple circles) for comparison to the optimal estimates.

The most sensitive estimate of ~45 $\mu\mathrm{T}/\sqrt{\mathrm{Hz}}$, measured with $I_{\mathrm{PL}} \approx 510$ kCts/s, occurs at low fields (~5 G) when the peaks are at least partially split. Further improvements to the collection efficiency and operating at a higher modulation frequency could improve the sensitivity of this technique by a factor of ~20, making it competitive with existing NV scanning-probe dc magnetometry protocols [24–26]. Stable trapping of single nanodiamonds would ameliorate noise from collisions within the trap and improve the spatial resolution of the technique. The use of shaped diamond particles trapped with a controlled orientation [112] and aligned along the appropriate crystallographic axis would remove the degrees of freedom that complicate the ESR lineshape from the situation

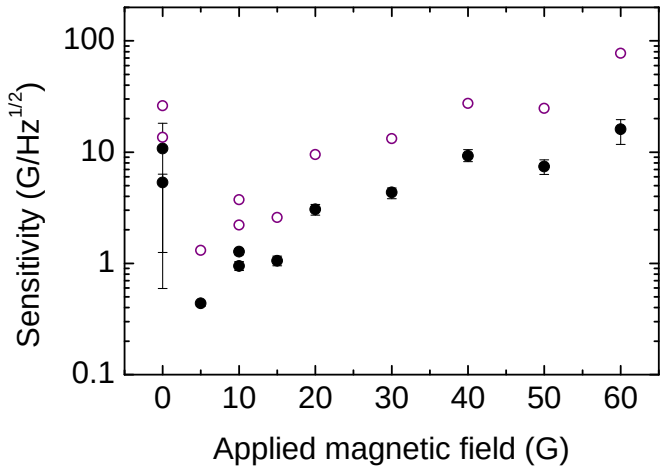

Figure 5.13: Estimated sensitivity of the diamond-based magnetometer using the optimal measuring scheme (black circles). The estimates are computed using values inferred from experiment, and the error bars reflect the 68.2% highest probability intervals from the propagated uncertainties. The demonstrated sensitivity (open purple circles) of the optically trapped nanodiamond-ensemble magnetometer is plotted for comparison. Reprinted from Ref. [1].

in bulk, opening the possibility of improved contrast and even vector magnetometry [33]. Alternately, an optical trap with a helical mode could be used to controllably rotate a trapped diamond particle such that the orientation would vary with a fixed rate [113], which would similarly remove the degrees of freedom that cause the broadened ESR lineshape.

♦♦♦

Chapter 6

Conclusion

The combination of optical trapping and NV-center-based sensing enables the three-dimensional mapping of magnetic fields in solution and addresses the need to probe complex environments, such as the interiors of microfluidic channels. Together, these two powerful techniques could pave the way for exploiting the unique electromagnetic and thermal sensing properties of NV centers at the nanoscale. Using optically trapped nanodiamonds for intracellular sensing [12] and the mapping of neurons [35, 114] are particularly exciting applications of this technique. The three-dimensional position control and on-demand release of optically trapped nanodiamonds enables applications requiring nanoscale precision placement of NV centers within existing systems, such as the controlled tagging of a single biological cell. Additionally, this technique may serve as a tool for monitoring physical and chemical processes at liquid/solid interfaces, which could help improve the understanding of electrochemical cells, surface catalysis, or lipid membranes in biomedicine.

♦♦♦

Appendix A

Etched nanodiamonds

Commercial nanodiamonds are generally produced by growing synthetic high temperature high pressure microdiamonds, then milling them into smaller particles. All nanodiamonds measured in the main text of this dissertation were produced this way. Another method is through a detonation process. Detonation nanodiamonds are generally smaller than milled nanodiamonds. They are also usually contaminated with a great deal of graphite.

Bulk diamond NV centers have significantly better properties for quantum information processing than commercially available nanodiamonds. For example, bulk diamond NV centers have a T_2 time of up to 1.82 ms in isotopically pure CVD samples [115] whereas nanodiamond NV centers have a T_2 time ranging from 250 ns to 1.4 μs [116]. It is true that the coherence times may be extended using dynamical decoupling [117], nevertheless the comparison between the bulk and nanocrystal T_2 times indicates that the NV in the bulk diamond has a much cleaner environment than the NV in the nanodiamond.

I used an inductively coupled plasma (ICP) to dry-etch a diamond

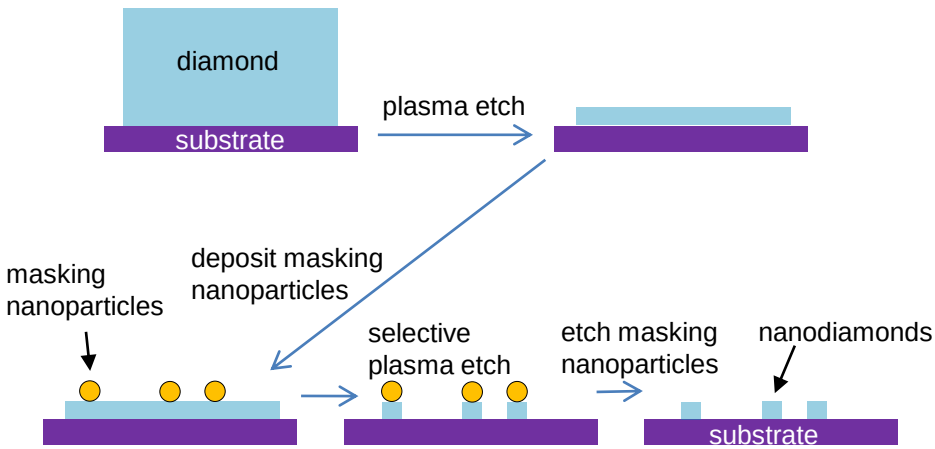

Figure A.1: Procedure for etching nanodiamonds.

membrane to the desired thickness, checking the thickness at intervals by scanning electron microscopy (SEM). For this first plasma etch, I used Ar/Cl_2 gas, though I also experimented with CF_4/O_2 gas [118]. When the diamond membrane was at the desired thickness, I drop-cast (see Section 3.2.1) gold nanoparticles onto the membrane as an etch mask. An anisotropic oxygen etch selectively etched the diamond and not the gold or the silicon oxide substrate. The etching procedure is shown in Fig. A.1.

We obtained randomly scattered diamond nanoparticles on the silicon oxide substrate (Fig. A.2*A*) with gold caps on top of the diamond particles (Fig A.2*B*-*C* and Fig. A.3*A*-*B*). The gold caps were subsequently removed (Fig. A.3*C*) using a gold etch.

The fabrication of nanoparticle diamonds is an ongoing project. By shaping nanodiamonds into rods, we hope to be able to form a shape that will not rotate in the optical trap.

♦♦♦

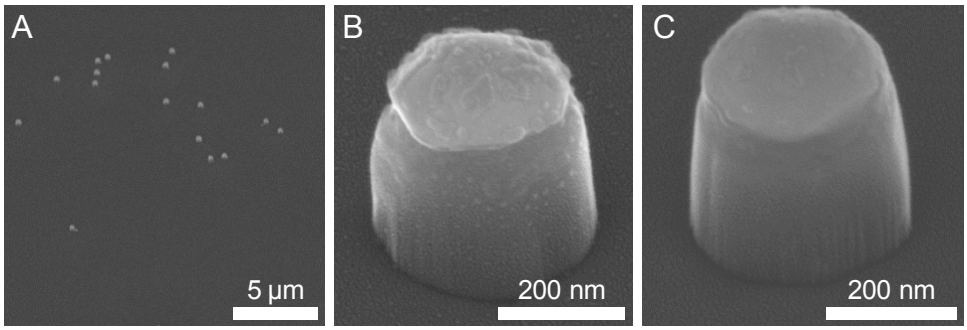

Figure A.2: SEM images of etched nanodiamonds with gold caps / etch masks. Stage tilted at 45°.

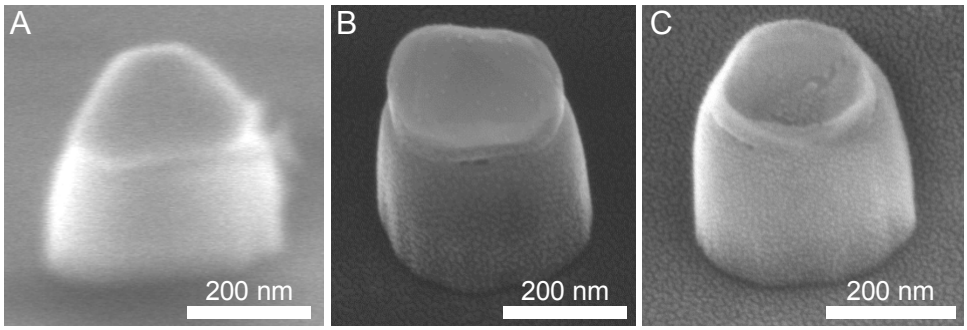

Figure A.3: SEM images of an etched nanodiamond (*A*) with gold caps / etch masks, (*B*) with gold caps after being metalized for SEM imaging, and (*C*) after gold caps have been removed with a wet etch. Stage tilted at 45° in all three subfigures. The image in (*A*) is smeared because the diamond surface is not conductive and it is charging.

References

[1] V. R. Horowitz, B. J. Alemán, D. J. Christle, A. N. Cleland, D. D. Awschalom. Electron spin resonance of nitrogen-vacancy centers in optically trapped nanodiamonds. *Proceedings of the National Academy of Sciences of the United States of America* **109**, 13493 (2012). xii, 47, 83, 85, 86, 87, 88, 90, 91, 94, 97, 105, 108, 109, 111, 112, 114

[2] K. C. Neuman, S. M. Block. Optical trapping. *Review of Scientific Instruments* **75**, 2787 (2004). 2, 20, 30, 33, 39, 48, 51, 54, 55, 56

[3] S. Block, L. Goldstein, B. Schnapp. Bead movement by single kinesin molecules studied with optical tweezers. *Nature* **348**, 348 (1990). 2

[4] M. Ericsson, D. Hanstorp, P. Hagberg, J. Enger, T. Nyström. Sorting out bacterial viability with optical tweezers. *Journal of Bacteriology* **182**, 5551 (2000). 2

[5] E. Abbondanzieri, W. Greenleaf, J. Shaevitz, R. Landick, S. Block. Direct observation of base-pair stepping by RNA polymerase. *Nature* **438**, 460 (2005). 2

[6] K. Svoboda, C. Schmidt, B. Schnapp, S. Block. Direct observation of kinesin stepping by optical trapping interferometry. *Nature* **365**, 721 (1993). 2

[7] S.-J. Yu, M.-W. Kang, H.-C. Chang, K.-M. Chen, Y.-C. Yu. Bright fluorescent nanodiamonds: No photobleaching and low cytotoxicity. *Journal of the American Chemical Society* **127**, 17604 (2005). 2

[8] C.-C. Fu, H.-Y. Lee, K. Chen, T.-S. Lim, H.-Y. Wu, P.-K. Lin, P.-K. Wei, P.-H. Tsao, H.-C. Chang, W. Fann. Characterization and application of single fluorescent nanodiamonds as cellular biomarkers. *Proceedings of the National Academy of Sciences of the United States of America* **104**, 727 (2007). 2

[9] K.-K. Liu, C.-L. Cheng, C.-C. Chang, J.-I. Chao. Biocompatible and detectable carboxylated nanodiamond on human cell. *Nanotechnology* **18**, 325102 (2007). 2

[10] A. M. Schrand, H. Huang, C. Carlson, J. J. Schlager, E. Ōsawa, S. M. Hussain, L. Dai. Are diamond nanoparticles cytotoxic? *The Journal of Physical Chemistry B* **111**, 2 (2007). 2

[11] Y.-R. Chang, H.-Y. Lee, K. Chen, C.-C. Chang, D.-S. Tsai, C.-C. Fu, T.-S. Lim, Y.-K. Tzeng, C.-Y. Fang, C.-C. Han, H.-C. Chang, W. Fann. Mass production and dynamic imaging of fluorescent nanodiamonds. *Nature Nanotechnology* **3**, 284 (2008). 2

[12] L. P. McGuinness, Y. Yan, A. Stacey, D. A. Simpson, L. T. Hall, D. Maclaurin, S. Prawer, P. Mulvaney, J. Wrachtrup, F. Caruso, R. E. Scholten, L. C. L. Hollenberg. Quantum measurement and orientation tracking

of fluorescent nanodiamonds inside living cells. *Nature Nanotechnology* **6**, 358 (2011). 2, 115

[13] R. J. Epstein, F. M. Mendoza, Y. K. Kato, D. D. Awschalom. Anisotropic interactions of a single spin and dark-spin spectroscopy in diamond. *Nature Physics* **1**, 94 (2005). 3, 75, 78

[14] A. Gruber, A. Dräbenstedt, C. Tietz, L. Fleury, J. Wrachtrup, C. von Borczyskowski. Scanning confocal optical microscopy and magnetic resonance on single defect centers. *Science* **276**, 2012 (1997). 3

[15] N. B. Manson, J. P. Harrison, M. J. Sellars. Nitrogen-vacancy center in diamond: Model of the electronic structure and associated dynamics. *Physical Review B* **74**, 104303 (2006). 3

[16] V. M. Acosta, A. Jarmola, E. Bauch, D. Budker. Optical properties of the nitrogen-vacancy singlet levels in diamond. *Physical Review B* **82**, 201202 (2010). 4

[17] J. R. Maze, A. Gali, E. Togan, Y. Chu, A. Trifonov, E. Kaxiras, M. D. Lukin. Properties of nitrogen-vacancy centers in diamond: the group theoretic approach. *New Journal of Physics* **13**, 025025 (2011). 4

[18] D. M. Toyli, D. J. Christle, A. Alkauskas, B. B. Buckley, C. G. Van de Walle, D. D. Awschalom. Measurement and control of single nitrogen-vacancy center spins above 600 K. *Physical Review X* **2**, 031001 (2012). 4, 6

[19] F. Jelezko, T. Gaebel, I. Popa, A. Gruber, J. Wrachtrup. Observation of coherent oscillations in a single electron spin. *Physical Review Letters* **92**, 76401 (2004). 4

[20] C. L. Degen. Scanning magnetic field microscope with a diamond single-spin sensor. *Applied Physics Letters* **92**, 243111 (2008). 4, 5

[21] J. M. Taylor, P. Cappellaro, L. Childress, L. Jiang, D. Budker, P. R. Hemmer, A. Yacoby, R. Walsworth, M. D. Lukin. High-sensitivity diamond magnetometer with nanoscale resolution. *Nature Physics* **4**, 810 (2008). 4, 5, 110

[22] G. Balasubramanian, I. Y. Chan, R. Kolesov, M. Al-Hmoud, J. Tisler, C. Shin, C. Kim, A. Wojcik, P. R. Hemmer, A. Krueger, T. Hanke, A. Leitenstorfer, R. Bratschitsch, F. Jelezko, J. Wrachtrup. Nanoscale imaging magnetometry with diamond spins under ambient conditions. *Nature* **455**, 648 (2008). 4, 5

[23] J. R. Maze, P. L. Stanwix, J. S. Hodges, S. Hong, J. M. Taylor, P. Cappellaro, L. Jiang, M. V. G. Dutt, E. Togan, A. S. Zibrov, A. Yacoby, R. L. Walsworth, M. D. Lukin. Nanoscale magnetic sensing with an individual electronic spin in diamond. *Nature* **455**, 644 (2008). 4

[24] R. S. Schoenfeld, W. Harneit. Real time magnetic field sensing and imaging using a single spin in diamond. *Physical Review Letters* **106**, 030802 (2011). 5, 113

[25] L. Rondin, J.-P. Tetienne, P. Spinicelli, C. D. Savio, K. Karrai, G. Dantelle, A. Thiaville, S. Rohart, J.-F. Roch, V. Jacques. Nanoscale magnetic field mapping with a single spin scanning probe magnetometer. *Applied Physics Letters* **100**, 153118 (2012). 5, 113

[26] P. Maletinsky, S. Hong, M. S. Grinolds, B. Hausmann, M. D. Lukin, R. L. Walsworth, M. Loncar, A. Yacoby. A robust scanning diamond sensor

for nanoscale imaging with single nitrogen-vacancy centres. *Nature Nanotechnology* **7**, 320 (2012). 5, 113

[27] O. Arcizet, V. Jacques, A. Siria, P. Poncharal, P. Vincent, S. Seidelin. A single nitrogen-vacancy defect coupled to a nanomechanical oscillator. *Nature Physics* **7**, 879 (2011). 5

[28] S. Kühn, C. Hettich, C. Schmitt, J. P. Poizat, V. Sandoghdar. Diamond colour centres as a nanoscopic light source for scanning near-field optical microscopy. *Journal of Microscopy* **202**, 2 (2001). 5

[29] T. van der Sar, E. C. Heeres, G. M. Dmochowski, G. de Lange, L. Robledo, T. H. Oosterkamp, R. Hanson. Nanopositioning of a diamond nanocrystal containing a single nitrogen-vacancy defect center. *Applied Physics Letters* **94**, 173104 (2009). 5

[30] M. Barth, N. Nüsse, B. Löchel, O. Benson. Controlled coupling of a single-diamond nanocrystal to a photonic crystal cavity. *Optics Letters* **34**, 1108 (2009). 5

[31] A. Cuche, A. Drezet, Y. Sonnefraud, O. Faklaris, F. Treussart, J.-F. Roch, S. Huant. Near-field optical microscopy with a nanodiamond-based single-photon tip. *Optics Express* **17**, 19969 (2009). 5

[32] L. T. Hall, C. D. Hill, J. H. Cole, B. Städler, F. Caruso, P. Mulvaney, J. Wrachtrup, L. C. L. Hollenberg. Monitoring ion-channel function in real time through quantum decoherence. *Proceedings of the National Academy of Sciences of the United States of America* **107**, 18777 (2010). 5

[33] B. J. Maertz, A. P. Wijnheijmer, G. D. Fuchs, M. E. Nowakowski, D. D. Awschalom. Vector magnetic field microscopy using nitrogen vacancy centers in diamond. *Applied Physics Letters* **96**, 092504 (2010). 5, 114

[34] S. Steinert, F. Dolde, P. Neumann, A. Aird, B. Naydenov, G. Balasubramanian, F. Jelezko, J. Wrachtrup. High sensitivity magnetic imaging using an array of spins in diamond. *Review of Scientific Instruments* **81**, 043705 (2010). 6

[35] L. M. Pham, D. L. Sage, P. L. Stanwix, T. K. Yeung, D. Glenn, A. Trifonov, P. Cappellaro, P. R. Hemmer, M. D. Lukin, H. Park, A. Yacoby, R. L. Walsworth. Magnetic field imaging with nitrogen-vacancy ensembles. *New Journal of Physics* **13**, 045021 (2011). 6, 115

[36] F. Dolde, H. Fedder, M. W. Doherty, T. Nobauer, F. Rempp, G. Balasubramanian, T. Wolf, F. Reinhard, L. C. L. Hollenberg, F. Jelezko, J. Wrachtrup. Electric-field sensing using single diamond spins. *Nature Physics* **7**, 459 (2011). 6

[37] C. K. Sun, Y. C. Huang, P. C. Cheng, H. C. Liu, B. L. Lin. Cell manipulation by use of diamond microparticles as handles of optical tweezers. *Journal of the Optical Society of America B: Optical Physics* **18**, 1483 (2001). 6

[38] L. M. Robledo Esparza, *Optical Manipulation of Mesoscopic Systems*, Ph.D. dissertation, Swiss Federal Institute of Technology Zurich (2008). 6, 7

[39] M. Geiselmann, M. Juan, J. Renger, J. M. Say, L. J. Brown, F. J. García de Abajo, F. Koppens, R. Quidant. 3D optical manipulation of a single electron spin. arXiv:1207.0650v2 [physics.optics]. 6, 8

[40] D. G. Grier. A revolution in optical manipulation. *Nature* **424**, 810 (2003). 10

[41] Y. Harada, T. Asakura. Radiation forces on a dielectric sphere in the Rayleigh scattering regime. *Optics Communications* **124**, 529 (1996). 10

[42] G. Gouesbet, G. Gréhan, *Generalized Lorenz-Mie Theories* (Springer, 2011). Available: www.springerlink.com/content/978-3-642-17193-2. 11

[43] K. Svoboda, S. M. Block. Biological applications of optical forces. *Annual Review of Biophysics and Biomolecular Structure* **23**, 247 (1994). 11, 55

[44] J. P. Gordon. Radiation forces and momenta in dielectric media. *Physical Review A* **8**, 14 (1973). 11

[45] B. N. Slama-Eliau, G. Raithel. Three-dimensional arrays of submicron particles generated by a four-beam optical lattice. *Physical Review E* **83**, 051406 (2011). 13

[46] R. Paschotta, *Encyclopedia of Laser Physics and Technology* (Wiley-VCH, 2008), pp. 270–273. Available: www.rp-photonics.com/gaussian_beams.html. 14

[47] J. Alda, *Encyclopedia of Optical Engineering* (Marcel Dekker, Inc., 2003), pp. 999–1013. Available: www.ucm.es/info/euoptica/org/pagper/jalda/docs/libr/laserandgaussian_eoe_03.pdf. 14

[48] C. J. R. Sheppard, S. Saghafi. Electromagnetic Gaussian beams beyond the paraxial approximation. *Journal of the Optical Society of America A: Optics, Image Science, and Vision* **16**, 1381 (1999). 15, 17, 18

[49] W. M. Lee, P. J. Reece, R. F. Marchington, N. K. Metzger, K. Dholakia. Construction and calibration of an optical trap on a fluorescence optical microscope. *Nature Protocols* **2**, 3226 (2007). 20, 48

[50] S. M. Block, *Cells: A Laboratory Manual*, D. L. Spector, R. D. Goldman, L. A. Leinwand, eds. (Cold Spring Harbor Laboratory Press, 1998). Available: www.cshlpress.com/chap_cells.tpl or www.stanford.edu/group/blocklab/cshl-chap.html. 20

[51] S. P. Smith, S. R. Bhalotra, A. L. Brody, B. L. Brown, E. K. Boyda, M. Prentiss. Inexpensive optical tweezers for undergraduate laboratories. *American Journal of Physics* **67**, 26 (1999). 20

[52] S. Cundiff, E. McKenna, Advanced optics lab - ECEN 5606: Basic skills lab (2004). Retrieved August 13, 2012 from http://massey.dur.ac.uk/resources/grad_skills/BasicAlignmentSkills.pdf. 20

[53] J. Pine, G. Chow. Moving live dissociated neurons with an optical tweezer. *Biomedical Engineering, IEEE Transactions on* **56**, 1184 (2009). 20

[54] J. M. Nascimento, E. L. Botvinick, L. Z. Shi, B. Durrant, M. W. Berns. Analysis of sperm motility using optical tweezers. *Journal of Biomedical Optics* **11**, 044001 (2006). 23

[55] Which primate has the fastest sperm? [Video], from article: "In promiscuous primates, sperm feel need for speed" by Roxanne Khamsi. NewScientist and the University of California San Diego (2007). Available: www.newscientist.com/article/dn12345 or www.youtube.com/watch?v=u2cldkDmbH4. 23

[56] S. J. Koch, Schaefer-Bergmann diffraction, acousto-optic, figshare (1999). Retrieved August 13, 2012 from http://dx.doi.org/10.6084/m9.figshare.89635 and http://commons.wikimedia.org/wiki/File:AOD_Loops_Schaefer-Bergmann.png. 24

[57] N. Uchida. Schaefer-Bergmann diffraction pattern due to the abnormal Bragg reflection in birefringent media. *Quantum Electronics, IEEE Journal of* **7**, 160 (1971). 24

[58] S. J. Koch, Koch Lab:Research/AOD tidbits, OpenWetWare (2007). Retrieved October 1, 2008 from http://openwetware.org/wiki/Koch_Lab:Research/AOD_tidbits. 24

[59] T. Pielage, B. van den Broek, J. van Mameren, Real-life μ-tetris [Video] (2002). Retrieved August 13, 2012 from http://joost.joostenyvonne.nl/tetris/ and www.youtube.com/watch?v=jCdnBmQZ6_s. 24

[60] Acousto-optic deflector (AOD). Retrieved August 13, 2012 from www.pi2.uni-stuttgart.de/contact/redaxo_methods/aod/Acousto.pdf;

see also www.pi2.uni-stuttgart.de/events/soccer/football.avi, retrieved June 20, 2008. 24

[61] K. Visscher, M. J. Schnitzer, S. M. Block. Single kinesin molecules studied with a molecular force clamp. *Nature* **400**, 184 (1999). 24

[62] M. J. Lang, C. L. Asbury, J. W. Shaevitz, S. M. Block. An automated two-dimensional optical force clamp for single molecule studies. *Biophysical Journal* **83**, 491 (2002). 24

[63] D. D'Orazio, Journal, Stony Brook Laser Teaching Center (2007). Retrieved July 3, 2008 from http://laser.physics.sunysb.edu/~dan/Journal/. 24

[64] J. W. Shaevitz, A practical guide to optical trapping (2006). Available: http://genomics.princeton.edu/shaevitzlab/OT_Practicle_Guide.pdf. 25, 26

[65] J. E. Curtis, B. A. Koss, D. G. Grier. Dynamic holographic optical tweezers. *Optics Communications* **207**, 169 (2002). 25

[66] Gaussian beams and the knife-edge measurement, Durham Atomic and Molecular Physics. Retrieved July 19, 2011 from http://massey.dur.ac.uk/resources/grad_skills/KnifeEdge.pdf. 27

[67] X. Cui, L. M. Lee, X. Heng, W. Zhong, P. W. Sternberg, D. Psaltis, C. Yang. Lensless high-resolution on-chip optofluidic microscopes for *Caenorhabditis elegans* and cell imaging. *Proceedings of the National Academy of Sciences of the United States of America* **105**, 10670 (2008). 31

[68] F. J. Pedrotti, L. S. Pedrotti, *Introduction to Optics* (Prentice Hall, edn. 2, 1992). 32, 34

[69] M. Abramowitz, M. W. Davidson, Microscope illumination. In the Olympus Microscopy Resource Center. Retrieved August 1, 2012 from www.olympusmicro.com/primer/anatomy/illumination.html. 33

[70] T. J. Fellers, M. W. Davidson, Conjugate planes in optical microscopy. In Nikon's MicroscopyU. Retrieved August 1, 2012 from www.microscopyu.com/articles/formulas/formulasconjugate.html. 33

[71] A. Pralle, M. Prummer, E.-L. Florin, E. H. K. Stelzer, J. K. H. Hörber. Three-dimensional high-resolution particle tracking for optical tweezers by forward scattered light. *Microscopy Research and Technique* **44**, 378 (1999). 49, 51

[72] F. Gittes, C. F. Schmidt. Interference model for back-focal-plane displacement detection in optical tweezers. *Optics Letters* **23**, 7 (1998). 49

[73] M. W. Allersma, F. Gittes, M. J. deCastro, R. J. Stewart, C. F. Schmidt. Two-dimensional tracking of ncd motility by back focal plane interferometry. *Biophysical Journal* **74**, 1074 (1998). 49

[74] J. K. Dreyer, K. Berg-Sørensen, L. Oddershede. Improved axial position detection in optical tweezers measurements. *Applied Optics* **43**, 1991 (2004). 51

[75] J. Fung, R. W. Perry, T. G. Dimiduk, V. N. Manoharan. Imaging multiple colloidal particles by fitting electromagnetic scattering solutions to digital holograms. *Journal of Quantitative Spectroscopy and Radiative Transfer* (2012). In press. 51

[76] A. Samadi, S. N. S. Reihani. Role of condenser iris in optical tweezer detection system. *Optics Letters* **36**, 4056 (2011). 52

[77] L. Friedrich, A. Rohrbach. Tuning the detection sensitivity: a model for axial backfocal plane interferometric tracking. *Optics Letters* **37**, 2109 (2012). 52

[78] F. V. Ignatovich, A. Hartschuh, L. Novotny. Detection of nanoparticles using optical gradient forces. *Journal of Modern Optics* **50**, 1509 (2003). 55

[79] S. F. Tolić-Nørrelykke, E. Schäffer, J. Howard, F. S. Pavone, F. Jülicher, H. Flyvbjerg. Calibration of optical tweezers with positional detection in the back focal plane. *Review of Scientific Instruments* **77**, 103101 (2006). 56

[80] A. E. Knight, G. Mashanov, J. E. Molloy. Single molecule measurements and biological motors. *European Biophysics Journal* **35**, 89 (2005). 56

[81] K. Visscher, S. P. Gross, S. M. Block. Construction of multiple-beam optical traps with nanometer-resolution position sensing. *Selected Topics in Quantum Electronics, IEEE Journal of* **2**, 1066 (1996). 56

[82] F. Czerwinski, A. C. Richardson, L. B. Oddershede. Quantifying noise in optical tweezers by Allan variance. *Optics Express* **17**, 13255 (2009). 56

[83] R. Hanlon. Cephalopod dynamic camouflage. *Current Biology* **17**, R400 (2007). 62

[84] R. Hanlon, C.-C. Chiao, L. Mäthger, A. Barbosa, K. Buresch, C. Chubb. Cephalopod dynamic camouflage: bridging the continuum between

background matching and disruptive coloration. *Philosophical Transactions of the Royal Society B: Biological Sciences* **364**, 429 (2009). 62

[85] A. El-Aneed, A. Cohen, J. Banoub. Mass spectrometry, review of the basics: Electrospray, MALDI, and commonly used mass analyzers. *Applied Spectroscopy Reviews* **44**, 210 (2009). 64

[86] W. D. Luedtke, U. Landman, Y.-H. Chiu, D. J. Levandier, R. A. Dressler, S. Sok, M. S. Gordon. Nanojets, electrospray, and ion field evaporation: Molecular dynamics simulations and laboratory experiments. *The Journal of Physical Chemistry A* **112**, 9628 (2008). 64

[87] W. Becker, The bh TCSPC handbook, Becker & Hickl GmbH (2006). Retrieved January 11, 2008 from www.becker-hickl.de/handbook.htm. 68

[88] C. Kurtsiefer, S. Mayer, P. Zarda, H. Weinfurter. Stable solid-state source of single photons. *Physical Review Letters* **85**, 290 (2000). 68

[89] A. Beveratos, S. Kühn, R. Brouri, T. Gacoin, J.-P. Poizat, P. Grangier. Room temperature stable single-photon source. *The European Physical Journal D – Atomic, Molecular, Optical and Plasma Physics* **18**, 191 (2002). 68

[90] P. Frantsuzov, M. Kuno, B. Jankó, R. A. Marcus. Universal emission intermittency in quantum dots, nanorods and nanowires. *Nature Physics* **4**, 519 (2008). 69

[91] Universal emission: Blinking stars on nanoscale, Physics blog: spintronics, nanoscience, vortex. University of Notre Dame. Retrieved August 13, 2012 from http://blogs.nd.edu/condensed-matter-physics/research/nanoscale/. 69

[92] X. Wang, X. Ren, K. Kahen, M. A. Hahn, M. Rajeswaran, S. Maccagnano-Zacher, J. Silcox, G. E. Cragg, A. L. Efros, T. D. Krauss. Non-blinking semiconductor nanocrystals. *Nature* **459**, 686 (2009). 69

[93] A. P. Magyar, J. C. Lee, A. M. Limarga, I. Aharonovich, F. Rol, D. R. Clarke, M. Huang, E. L. Hu. Fabrication of thin, luminescent, single-crystal diamond membranes. *Applied Physics Letters* **99**, 081913 (2011). 69

[94] M. Nirmal, B. O. Dabbousi, M. G. Bawendi, J. J. Macklin, J. K. Trautman, T. D. Harris, L. E. Brus. Fluorescence intermittency in single cadmium selenide nanocrystals. *Nature* **383**, 802 (1996). 71

[95] C. Bradac, T. Gaebel, N. Naidoo, M. J. Sellars, J. Twamley, L. J. Brown, A. S. Barnard, T. Plakhotnik, A. V. Zvyagin, J. R. Rabeau. Observation and control of blinking nitrogen-vacancy centres in discrete nanodiamonds. *Nature Nanotechnology* **5**, 345 (2010). 71

[96] A. L. Efros, M. Rosen. Random telegraph signal in the photoluminescence intensity of a single quantum dot. *Physical Review Letters* **78**, 1110 (1997). 75

[97] A. Efros, *Semiconductor Nanocrystals: From Basic Principles to Applications*, A. L. Efros, D. J. Lockwood, L. Tsybeskov, eds. (Kluwer Academic/Plenum Publishers, New York, 2003), pp. 52–72. Available: arXiv:cond-mat/0204437. 75

[98] M. Kuno, D. P. Fromm, A. Gallagher, D. J. Nesbitt, O. I. Micic, A. J. Nozik. Fluorescence intermittency in single InP quantum dots. *Nano Letters* **1**, 557 (2001). 75

[99] M. Kuno, D. P. Fromm, S. T. Johnson, A. Gallagher, D. J. Nesbitt. Modeling distributed kinetics in isolated semiconductor quantum dots. *Physical Review B* **67**, 125304 (2003). 75

[100] P. A. Frantsuzov, R. A. Marcus. Explanation of quantum dot blinking without the long-lived trap hypothesis. *Physical Review B* **72**, 155321 (2005). 75

[101] K. T. Shimizu, R. G. Neuhauser, C. A. Leatherdale, S. A. Empedocles, W. K. Woo, M. G. Bawendi. Blinking statistics in single semiconductor nanocrystal quantum dots. *Physical Review B* **63**, 205316 (2001). 75

[102] J. Tang, R. A. Marcus. Mechanisms of fluorescence blinking in semiconductor nanocrystal quantum dots. *The Journal of Chemical Physics* **123**, 054704 (2005). 75

[103] M. Pelton, G. Smith, N. F. Scherer, R. A. Marcus. Evidence for a diffusion-controlled mechanism for fluorescence blinking of colloidal quantum dots. *Proceedings of the National Academy of Sciences of the United States of America* **104**, 14249 (2007). 75

[104] K. Park, K. Berland, Investigating molecular rotational dynamics with fluorescence fluctuation spectroscopy (2007). Available: www.cse.emory.edu/sciencenet/undergrad/SURE/Posters/2007_Park_Keon-young.cfm. 77

[105] R. Hanson, V. V. Dobrovitski, A. E. Feiguin, O. Gywat, D. D. Awschalom. Coherent dynamics of a single spin interacting with an adjustable spin bath. *Science* **320**, 352 (2008). 84

[106] D. Braun, A. Libchaber. Computer-based photon-counting lock-in for phase detection at the shot-noise limit. *Optics Letters* **27**, 1418 (2002). 85

[107] F. T. Arecchi, E. Gatti, A. Sona. Time distribution of photons from coherent and Gaussian sources. *Physics Letters* **20**, 27 (1966). 85

[108] E. Laloy, J. A. Vrugt. High-dimensional posterior exploration of hydrologic models using multiple-try DREAM$_{(ZS)}$ and high-performance computing. *Water Resources Research* **48**, W01526 (2012). 99

[109] A. Sevgen, Electric dipole radiation (2009). Available: http://hbar.phys.boun.edu.tr/~sevgena/p202/docs/Electric%20dipole%20radiation.pdf. 102

[110] A. Dréau, M. Lesik, L. Rondin, P. Spinicelli, O. Arcizet, J.-F. Roch, V. Jacques. Avoiding power broadening in optically detected magnetic resonance of single NV defects for enhanced dc magnetic field sensitivity. *Physical Review B* **84**, 195204 (2011). 110

[111] M.-H. Chen, Q.-M. Shao. Monte Carlo estimation of Bayesian credible and HPD intervals. *Journal of Computational and Graphical Statistics* **8**, 69 (1999). 113

[112] W. A. Shelton, K. D. Bonin, T. G. Walker. Nonlinear motion of optically torqued nanorods. *Physical Review E* **71**, 036204 (2005). 113

[113] L. Paterson, M. P. MacDonald, J. Arlt, W. Sibbett, P. E. Bryant, K. Dholakia. Controlled rotation of optically trapped microscopic particles. *Science* **292**, 912 (2001). 114

[114] L. T. Hall, G. C. G. Beart, E. A. Thomas, D. A. Simpson, L. P. McGuinness, J. H. Cole, J. H. Manton, R. E. Scholten, F. Jelezko, J. Wrachtrup, S. Petrou, L. C. L. Hollenberg. High spatial and temporal resolution wide-field imaging of neuron activity using quantum NV-diamond. *Nature Scientific Reports* **2**, 401 (2012). 115

[115] G. Balasubramanian, P. Neumann, D. Twitchen, M. Markham, R. Kolesov, N. Mizuochi, J. Isoya, J. Achard, J. Beck, J. Tissler, V. Jacques, P. R. Hemmer, F. Jelezko, J. Wrachtrup. Ultralong spin coherence time in isotopically engineered diamond. *Nature Materials* **8**, 383 (2009). 116

[116] J. Tisler, G. Balasubramanian, B. Naydenov, R. Kolesov, B. Grotz, R. Reuter, J.-P. Boudou, P. A. Curmi, M. Sennour, A. Thorel, M. Börsch, K. Aulenbacher, R. Erdmann, P. R. Hemmer, F. Jelezko, J. Wrachtrup. Fluorescence and spin properties of defects in single digit nanodiamonds. *ACS Nano* **3**, 1959 (2009). 116

[117] G. de Lange, Z. H. Wang, D. Ristè, V. V. Dobrovitski, R. Hanson. Universal dynamical decoupling of a single solid-state spin from a spin bath. *Science* **330**, 60 (2010). 116

[118] Y. Ando, Y. Nishibayashi, K. Kobashi, T. Hirao, K. Oura. Smooth and high-rate reactive ion etching of diamond. *Diamond and Related Materials* **11**, 824 (2002). 117

♦♦♦